Computational Modeling of Molecular Junctions: Transport, Structure and Inelastic effects

Bækgaard, Iben Sig Buur

Publication date:
2009

Document Version
Early version, also known as pre-print

Preface

This thesis is submitted in candidacy for the Ph.D. degree from the Technical University of Denmark (DTU). It is based on the work carried out at the Center for Atomic-scale Materials Design (CAMD), Department of Physics at DTU from March 2005 to September 2009 (maternity leave from June 2007 to March 2009) under the supervision of Kristian S. Thygesen and Professor Karsten W. Jacobsen. Financial support was provided by DTU.

First of all, I would like to thank Kristian and Karsten for great supervision and many inspiring discussions. I am also very grateful to Jens K. Nørskov for being my supervisor in the work on CO oxidation.

Part of the work on the platinum/hydrogen contact was carried out in cooperation with Jan van Ruitenbeek, Darko Djukic and Manabu Kiguchi. I thank them for sharing their experimental results and insights with me. A number of people have been helpful and inspired me, those are: Robert Stadler, Mikkel Strange, Thomas Frederiksen, Magnus Paulsson, Hanne Falsig, Britt Hvolbæk and Thomas Bligaard.

Finally, I thank Mikkel Bækgaard for his patience and support during the whole period and my son Gustav for reminding me of the really important things in life.

Lyngby, September 19, 2009
Iben Sig Buur Bækgaard

Abstract

This thesis describes theoretical investigations of the conductance properties of some selected nano-scale junctions. The studies are based on a numerical scheme where the atomic and electronic structure of the junction is described within ground state density functional theory (DFT). This in combination with the non-equilibrium Green's function (NEGF) formalism makes it possible to describe the electrical properties of atomic-sized junctions realistically.

In the attempt to establish a general consensus concerning the correct result of a NEGF-DFT calculation a set of benchmark calculations has been performed. The Kohn-Sham elastic transmission function of five representative single-molecule junctions are calculated using two different and independent, albeit similar, density functional theory (DFT) methods: (i) An ultra soft pseudopotential plane wave code DACAPO [1, 2] in combination with maximally localized Wannier functions [3]. (ii) The norm-conserving pseudopotential code SIESTA [4] which applies finite range pseudo atomic orbitals [5]. It is found that for all reference systems the SIESTA transmission function converges towards the plane wave result as the SIESTA basis is enlarged. Overall, an atomic basis with double-zeta and polarization is sufficient (and in some cases even necessary) to ensure quantitative agreement with the plane-wave calculation.

The electrical properties of single-molecule junctions are sensitive to the detailed atomic structure of the contact. This, in turn, is for organic molecules largely determined by the anchoring group. With the aim of identifying and comparing the intrinsic properties of two commonly used anchoring groups (thiol and amine) the atomic structure and conductance traces of different Au-S-Au and Au-NH_2-Au nanojunctions have been calculated. It was found that the structural selectivity of the amine group leads to small junction to junction fluctuations in the conductance traces of the Au-NH_2-Au junctions. On the other hand, the larger variability in sulphur-gold bonding geometries leads to significantly different Au-S-Au conductance traces depending on the atomic structure of the gold contacts. This indicates, in agreement with experiments [6], that the intrinsic transport properties of the amine group are more well defined than those of the thiol.

The conductance histograms obtained when a Pt contact is broken in a hydrogen atmosphere show two strong peaks, one near 1 G_0 and the other around 0.2 G_0 on top of a low-conductance tail [7, 8, 9]. In previous work substantial evidence have been given that the atomic structure responsible for the pronounced 1 G_0 peak consists of a hydrogen molecule captured between platinum electrodes [10]. To further characterize this linear bridge configuration first-principles calculations of the non-linear dI/dV curves are presented. The conductance is found to decrease by a few percentage at threshold voltages corresponding to the excitation energy of longitudinal vibrations of the H_2 molecule. The transverse vibrations, on the other hand, induce an *increase* in conductance. The latter is not in agreement with the experimental findings and seems, at first, to conflict with the so-called one-channel model. On the basis of scattering theory it is shown that the increase

is a result of the fact that the transverse vibrations can mediate transport through the otherwise non-transmitting Pt *d*-channels. This explanation is consistent with the finding that for a Au/H_2 bridge the transverse modes do not affect the conductance.

A detailed study of platinum/hydrogen chains bridging Pt electrodes has been performed. By comparison with the experimental evidence it is shown that the 0.2 G_0 conductance peak is likely due to a hydrogen decorated Pt chain in contact with the H_2 molecular bridge. The chain formation process were investigated and it was found that actual "wire pulling" is unlikely as the hydrogen molecule is only weakly bound to the platinum electrodes.

Resumé

I denne Ph.D afhandling beskrives teoretiske undersøgelser af nogle udvalgte nanoskala kontakters elektriske ledningsegenskaber. Systemernes konduktans er beregnet ved brug af en numerisk fremgangsmåde, hvor den atomare og elektroniske struktur af kontakten beskrives ved hjælp af tæthedsfunktionalteori (DFT). Dette i kombination med ikkeligevægts Green's funktions (NEGF) formalismen gør det muligt at beskrive de elektriske ledningsegenskaber for atomare kontakter realistisk.

I forsøget på at opnå en general enighed om, hvad det korrekte resultat af en NEGF-DFT beregning er, præsenteres en række benchmark beregninger. Kohn-Sham transmissionfunktionen for fem repræsentative nanoskala kontakter er beregnet ved brug af to forskellige og uafhængige tæthedsfunktional (DFT) metoder: (i) En planbølge kode DACAPO [1, 2] med ultrabløde pseudopotentialer kombineret med maksimalt lokaliserede Wannier funktioner [3]. (ii) En normbevarende pseudopotential kode SIESTA [4], som anvender pseudo atomare orbitaler med endelig rækkevidde [5]. Det konstateres, at for alle referencesystemerne konvergerer SIESTA transmission funktionen mod planbølge resultatet når SIESTA basissættet udvides. Generelt er en atomar basis med dobbelt zeta og polarisering tilstrækkeligt (og i visse tilfælde endda nødvendigt) for at sikre en kvantitative overensstemmelse med planbølgeregningen.

De elektriske ledningsegenskaber af et enkelt molekyle, som er placeret imellem to metalelektroder, er afhængig af den detaljerede atomare kontaktstruktur. For organiske molekyler bestemmes kontaktstrukturen i høj grad af forbindelsesgruppen. For at identificere og sammenligne to almindelige forbindelsesgruppers (thiol og amine) karakteristiske egenskaber er den atomare struktur og konduktanskurverne for forskellige Au-S-Au and Au-NH_2-Au nanoskala kontakter blevet beregnet. Det viser sig, at amine gruppens strukturelle selektivitet medfører, at der kun observeres små variationer i konduktansen når den atomare struktur af guld-kontakten ændres. Derimod, medfører den større variation i svovl-guld bindingsgeometrien, at der, afhængigt af kontaktstrukturen, kan observeres markant forskellige Au-S-Au konduktanskurver. Denne forskel indikerer, i overensstemmelse med nyere eksperimenter [6], at amine gruppen har mere veldefinerede ledningsegenskaber end thiol.

I konduktanshistogrammet, som fremkommer når en platintråd brydes i en hydrogen gas, observeres to tydelige toppe, den ene tæt ved 1 G_0 og den anden omkring 0.2 G_0 [7, 8, 9]. Tidligere undersøgelser tyder stærkt på, at 1 G_0 toppen kan forklares ved den gentagne forekomst af en kontaktstruktur, hvor et hydrogenmolekyle er udspændt imellem to platinelektroder [10]. For yderligere at karakterisere denne molekylære hydrogen ,,bro" præsenteres *ab initio* beregninger af ikke-lineære dI/dV kurver. Det findes at, systemets konduktans formindskes med et par procent, når eksitationsenergien for de longitudinale vibrationer af H_2 molekylet svarer til den påtrykte spænding. Eksitationen af de transverse vibrationer medfører derimod en *stigning* i konduktansen. Sidstnævnte stemmer ikke overens med de eksperimentelle resultater, og synes, i første omgang, at være i konflikt

med den såkaldte ,,en-kanals“ model. Med udgangspunkt i spredningsteorien vises det, at konduktansstigningerne kan forklares ved, at de transverse vibrationstilstande kan mediere transport gennem de ellers ikke-transmitterende platin *d*-kanaler. Denne forklaring er i overensstemmelse med, at de transverse vibrationstilstande ikke påvirker den elektriske ledningsevne af en Au/H_2 kontakt.

En detaljerede undersøgelse af platin/hydrogen kæder udspændt imellem platin kontakter er blevet udført. Ved sammenligning med eksperimentelle resultater vises det, at konduktanstoppen ved 0.2 G_0 sandsynligvis skyldes en atomar platinkæde dekoreret med hydrogen atomer og i kontakt med den molekylære H_2 ,,bro“. Undersøgelser af, hvorledes denne atomare kæde dannes viste, at det er usandsynligt at den molekylære H_2 ,,bro“ kan trække kæder, dette skyldes at hydrogen molekylet kun er svagt bundet til platinelektroderne.

List of included papers

Paper I
Evidence for a Single Hydrogen Molecule Connected by an Atomic Chain
M. Kiguchi, R. Stadler, I. S. Kristensen, D. Djukic and J. M. van Ruitenbeek
Physical Review Letters, **98**, 146802 (2007).

Paper II
Benchmark density functional theory calculations for nano-scale conductance
M. Strange, I. S. Kristensen, K. S. Thygesen, and K. W. Jacobsen
Journal of Chemical Physics, **114**, 114714 (2008).

Paper III
Trends in the Catalytic CO Oxidation Activity of Nanoparticles
Hanne Falsig, Britt Hvolbæk, Iben S. Kristensen, Tao Jiang, Thomas Bligaard, Claus H. Christensen and Jens K. Nørskov
Angewandte Chemie - International Edition, **47**, 4835 (2008).

Paper IV
Comparative study of anchoring groups for molecular electronics: structure and conductance of Au-S-Au and Au-NH_2-Au junctions
I. S. Kristensen, D. J. Mowbray, K. S. Thygesen, and K. W. Jacobsen
Journal of Physics: Condensed Matter, **20**, 374101 (2008).

Paper V
Inelastic Scattering in Metal-H_2-Metal Junctions
I. S. Kristensen, M. Paulsson, K. S. Thygesen and K. W. Jacobsen
Physical Review B, **79**, 235411 (2009).

Contents

Chapter 1

Introduction

The topic of this thesis is theoretical modeling of the electronic properties of nano-scale contacts. Here a nano-scale contact consists of two metal electrodes connected by a single molecule or a chain of single atoms.

The downscaling of semiconductor devices is characterized by Moore's law which states that the number of transistors on an integrated circuit doubles approximately every two years [11]. Ultimately the circuit components will reach the atomic limit and new device structures must emerge [12]. Molecular electronics, where individual organic molecules are tailored to act as different electronic components and atomic wires represents the smallest interconnects, could resolve the problem. Due to this prospect of replacing the conventional semiconductor devices by single-molecule junctions the study of nano-scale contacts has acquired a lot of attention.

The theoretical concept of an organic molecule acting as a rectifier goes back to Aviram and Ratner [13]. Experimental techniques for manipulating and contacting individual molecules started to appear around 1990 [14]. One approach is based on the scanning tunneling microscope (STM), where the conducting tip can approach molecules on a surface [15, 16]. Another tool for studying transport through single molecules is the mechanical controllable break junction (MCBJ) [17, 18]. Experiments on single-molecule junctions are far from trivial and the measured conductance often shows considerable junction to junction variations. This variability probably originates from details beyond experimental control such as the detailed atomic arrangement of the electrodes.

In general, experiments on nano-scale systems are quite indirect and must therefore be supplemented by theoretical models. These models can provide insight into the atomic structure and electrical properties of a single-molecule junction. For these models to describe the properties of nano-scale junctions realistically they must not only describe the quantum nature of the electrons but also give an atomistic description of the junction. Today the "standard" approach is to combine density functional theory (DFT) with non-equilibrium Green's function (NEGF) techniques [19, 20, 21, 22]. This first-principle method for calculating the conductance of a nano-scale contact only takes the atomic number and positions as input. Although the method is not rigorously justified [23, 24, 25] it has been successful for strongly coupled systems such as homogeneous metal point contacts and mono-atomic wires [26, 27, 28]. However, the NEGF-DFT method systematically overestimates the conductance of weakly coupled system like benzenedithiolate between gold contacts [29, 30].

The electrical properties of single-molecule junctions are very sensitive to changes in the scattering potential. Especially, small errors in the description of the coupling to the leads can result in significant changes in the transmission function. In fact, there are

several examples in the literature where different groups have published different results for the same or very similar systems [10, 31, 32]. Irrespective of the principal validity of the NEGF-DFT approach it is important to remove such confusions and establish a common reference for the method. For that reason a benchmark study, where two different and independent implementations of NEGF-DFT is compared, have been performed.

In this thesis, the focus is on nano-scale junctions which contains a single atom or a small molecule like H_2. In light of the difficulties encountered when (both experimentally and theoretically) studying larger organic molecules these simple contacts seems to provide a natural starting point for the study of electron transport in single-molecule junctions.

Outline of the thesis

Chapter 2 gives an introduction to density functional theory (DFT) and some aspects related to the numerical implementation.

Chapter 3 introduces a theoretical framework based on Green's functions for calculating the current through a general nano-scale contact. The effects of electron-phonon interaction is discussed in detail.

Chapter 4 demonstrates how the general Green's function transport scheme can be combined with DFT to provide a first-principle description of the electrical properties of nano-scale contacts.

Chapter 5 reviews a set of benchmark calculations for the transmission function calculated using two different NEGF-DFT methods. This chapter is based on Paper II.

Chapter 6 presents a study of the intrinsic transport properties of two commonly used anchoring groups (thiol and amine). This chapter summarizes Paper IV.

Chapter 7 presents work on H_2 in Pt and Au nano-contacts and is based on Papers I and V.

Chapter 2

Electronic structure calculations

Electronic structure theory describes the dynamics of electrons in atoms, molecules and condensed phases. *Ab initio* electronic structure calculations have, due to the increase in computer power, become a valuable tool for modeling a wide range of systems, i.e nanocontacts and surfaces, realistically.

This chapter begins with a short introduction to the many-body Hamiltonian. Then a short overview of density functional theory (DFT) is provided followed by a description of the exchange-correlation functional and its approximations. In Sec. 2.3 some important aspects of the numerical implementation of DFT are introduced. Finally the dynamics of the ions are discussed. Atomic units will be assumed throughout this chapter, $e = \hbar = m_e = 1$.

2.1 The many-body problem

In principle, all properties of an atomic system consisting of interacting electrons and nuclei can be found from the time-independent Schrödinger equation[1]

$$H\Phi_n(\mathbf{r}, \mathbf{R}) = E_n\Phi_n(\mathbf{r}, \mathbf{R}), \tag{2.1}$$

where H is the many-body Hamiltonian which, in the general case, consists of a sum of kinetic energy terms, electrostatic Coulomb interactions and external potentials from e.g. externally applied magnetic and electric fields. E_n is the total energy of the quantum mechanical state $\Phi_n(\mathbf{r}, \mathbf{R})$. The eigenstates depends on the spatial coordinates of both the electrons $\mathbf{r} = \{\mathbf{r}_i\}$ and the nuclei $\mathbf{R} = \{\mathbf{R}_I\}$.

By utilizing the Born-Oppenheimer (BO) approximation [33] the many-body Hamiltonian can be greatly simplified. The BO approximation states that due to the large difference in mass between electrons and nuclei ($m_e/M_I \approx 10^{-3} - 10^{-6}$), the nuclear and electronic degrees of freedom may be decoupled. In other words, the electrons can be considered as responding instantaneously to changes in the nuclear positions. Within the BO approximation the eigenstates of the whole system can be written as products

$$\Phi_n(\mathbf{r}, \mathbf{R}) = \chi_{n,k}(\mathbf{R})\Psi_k(\mathbf{r}; \mathbf{R}),$$

where the motion of the nuclei are described by $\chi_{n,k}(\mathbf{R})$ and the electronic motion is determined by the wave function $\Psi_k(\mathbf{r}; \mathbf{R})$ which depends parametrically on the nuclear coordinates.

[1] In general, the properties of any system is governed by the time-dependent Schrödinger equation. But as we only consider time-independent interatomic interactions in this chapter, the dynamics of the system is described by the time-independent Schrödinger equation.

The dynamics of the electrons, which move in the field of a fixed set of nuclei, is determined by the Hamiltonian

$$H_{\mathrm{e}}(\mathbf{R}) = T_{\mathrm{e}} + V_{\mathrm{ext}} + V_{\mathrm{ee}} + V_{\mathrm{nn}}. \tag{2.2}$$

The first term (Te) is the kinetic energy of the electrons. The second term (V_{ext}) is the external potential acting on the electrons, which in the absence of an external fields reduces to the attractive Coulomb interaction between the electrons and the static nuclei. The final terms (V_{ee} and V_{nn}) are the Coulomb repulsion between the electrons and nuclei, respectively.

In the position representation the Hamiltonian in Eq. (2.2) takes the form

$$H_{\mathrm{e}}(\mathbf{R}) = -\frac{1}{2}\sum_{i=1}^{N}\nabla_i^2 + \sum_{i=1}^{N} v_{\mathrm{ext}}(\mathbf{r}_i) + \sum_{i<j}\frac{1}{|\mathbf{r}_i - \mathbf{r}_j|} + \sum_{I<J}\frac{Z_I Z_J}{|\mathbf{R}_I - \mathbf{R}_J|},$$

and acts on an anti-symmetric N-electron wave function, $\Psi_k(\mathbf{r};\mathbf{R})$.

Within the BO approximation the Hamiltonian for the nuclear system reduces to

$$H_{\mathrm{n}} = T_{\mathrm{n}} + E_0(\mathbf{R}), \tag{2.3}$$

where T_{n} is the kinetic energy of the nuclei and $E_0(\mathbf{R}) = \langle\Psi_0|H_{\mathrm{e}}(\mathbf{R})|\Psi_0\rangle$ is the ground state energy of the system. That is, the nuclei moves in an effective potential given by the ground state of the electrons.

Although the BO approximation simplifies the Schrödinger equation, the determination of eigenstates and energies of a many-body system is a major task. Therefore, one of the main problems in condensed matter physics and quantum chemistry is to find approximate methods to solve Eq. (2.1). Today one of the most powerful and popular ways of finding the ground state properties of an atomic-scale system is provided by density functional theory (DFT). As the work presented in this thesis is based on DFT, the next sections are devoted to a general introduction to the method.

2.2 Density functional theory

In this section the main concepts of density function theory is described. DFT provides a method for calculating the ground state properties of an interacting electron system described by the Hamiltonian in Eq. (2.2). More complete reviews of the theory are found in Refs. [34, 35, 36].

In DFT the central quantity is the ground state electron density $\rho_0(\mathbf{r})$. By replacing the full N-particle wave function with the electron density the number of degrees of freedom is immediately reduced from 3N to 3. This replacement is formally justified by two theorems proved Hohenberg and Kohn in a paper from 1964 [37].

The first Hohenberg-Kohn (HK) theorem states that there is a one-to-one correspondence between the external potential ($v_{\mathrm{ext}}(\mathbf{r})$) and the ground state electron density ($\rho_0(\mathbf{r})$) of an interacting system. Since the external potential together with the number of electrons completely defines the electronic Hamiltonian (2.2) all ground state properties becomes functionals of the ground state electron density.

The second HK theorem provides a variational principle for the energy functional $E_0 \leq E\left[\tilde{\rho}\right]$, where $\tilde{\rho}$ is a trial density that corresponds to an external potential. To avoid the v-representability problem (i.e. the mathematical difficulties in characterizing the

set of trial densities) Levy and Lieb [38, 39] devised the more useful constrained search formalism

$$E_0[\rho] = \min_{\rho(\mathbf{r})\to \mathrm{N}} \left\{ \min_{\Psi\to\rho(\mathbf{r})} \langle \Psi | T + V_{ee} | \Psi \rangle + \int d\mathbf{r} \rho(\mathbf{r}) v_{\mathrm{ext}}(\mathbf{r}) \right\}, \tag{2.4}$$

where the larger class of N-representable[2] electron densities are searched. The first term $F[\rho] = \min_{\Psi\to\rho(\mathbf{r})} \langle \Psi | T + V_{\mathrm{ee}} | \Psi \rangle$, is a universal functional in the sense that it does not depend on the external potential. Since the HK theorems do not provide any prescriptions on how to determine $F[\rho]$, the constrained search formalism is not yet of any practical use. In a subsequent paper Kohn and Sham [40] presented an indirect but formally exact way of determining the energy functional $E_0[\rho]$.

2.2.1 The Kohn-Sham equations

Kohn and Sham realized that the many-body problem of a system of interacting electrons moving in an external potential could be replaced by an auxiliary system of non-interacting electrons moving in an effective potential. The effective potential of the non-interacting system should be chosen such that the ground state density is the same as for the real interacting system. The energy functional (2.4) can now be decomposed as

$$E_0[\rho] = T_s[\rho] + J[\rho] + E_{xc}[\rho] + \int d\mathbf{r} v_{\mathrm{ext}}(\mathbf{r}) \rho(\mathbf{r}),$$

where T_s is the kinetic energy of a non-interacting electron gas, the Hartree term $J[\rho] = \frac{1}{2} \int\int d\mathbf{r} d\mathbf{r}' \frac{\rho(\mathbf{r})\rho(\mathbf{r}')}{|\mathbf{r}-\mathbf{r}'|}$ is the classical Coulomb repulsion between the electrons and the exchange-correlation (xc) functional $E_{xc}[\rho]$ is defined as

$$E_{xc}[\rho] = T[\rho] - T_s[\rho] + V_{\mathrm{ee}}[\rho] - J[\rho].$$

The (presumably small) xc term contains the correlation contribution to the kinetic energy and the electron-electron interaction energy beyond the Hartree term. Thus, all quantum many-body interactions are incorporated into this, generally unknown, xc functional.

The so-called Kohn-Sham equations are obtained through a variational search over single-particle orbitals

$$H_{\mathrm{KS}} \psi_i(\mathbf{r}) = \left[-\frac{1}{2}\nabla^2 + v_{\mathrm{eff}}(\mathbf{r}) \right] \psi_i(\mathbf{r}) = \varepsilon_i \psi_i(\mathbf{r}), \tag{2.5}$$

$$v_{\mathrm{eff}}(\mathbf{r}) = v_{\mathrm{ext}}(\mathbf{r}) + \int d\mathbf{r}' \frac{\rho(\mathbf{r}')}{|\mathbf{r}-\mathbf{r}'|} + \frac{\delta E_{xc}[\rho]}{\delta \rho}, \tag{2.6}$$

$$\rho(\mathbf{r}) = \sum_{i=1}^{N} |\psi_i(\mathbf{r})|^2. \tag{2.7}$$

Here $\psi_i(\mathbf{r})$ is the Kohn-Sham single-particle eigenstates describing non-interacting electrons moving in the local effective potential $v_{\mathrm{eff}}(\mathbf{r})$. The ground state density is obtained from the N lowest Kohn-Sham eigenstates. Since the ground state density must reproduce the effective potential from which it was generated the Kohn-Sham equations needs to be solved self-consistenly. The ground state energy of the full system can now be obtained from the Kohn-Sham eigenvalues

$$E_0(\mathbf{R}) = \sum_{i=1}^{N} \varepsilon_i - \frac{1}{2} \int\int d\mathbf{r} d\mathbf{r}' \frac{\rho(\mathbf{r})\rho(\mathbf{r}')}{|\mathbf{r}-\mathbf{r}'|} + E_{xc}[\rho] - \int d\mathbf{r} \frac{\partial E_{xc}[\rho]}{\partial \rho} \rho(\mathbf{r}) + \sum_{I<J} \frac{Z_I Z_J}{|\mathbf{R}_I - \mathbf{R}_J|}. \tag{2.8}$$

[2]The N-representability condition demands that the electron densities are non-negative, integrates up to N and have no divergence at the boundaries.

2.2.2 The exchange-correlation functional

Physically, the exchange-correlation term (which generally lowers the energy) describes the charge depletion observed in the vicinity of a single electron, i.e. it is associated with the correlation between the positions of the electrons. Especially, the exchange part can be associated with the Pauli exclusion principle [41].

In principle, the Kohn-Sham equations provides the exact ground state density, but in practice, the exchange correlation functional (which defines the effective potential) is unknown and must be approximated. It is noted that in order to avoid non-physical behavior of the total energy it is important to ensure that an explicit approximation to the true xc functional obeys a certain set of rules [42, 43].

In their original paper Kohn and Sham presented the so-called local density approximation (LDA) [40] for the xc functional. In LDA the exchange-correlation energy of the real interacting system with the local density $\rho(\mathbf{r})$ is, at every point in space, replaced by the exchange-correlation energy of a homogeneous electron gas with the same density

$$E_{xc}^{LDA}[\rho] = \int d\mathbf{r}\rho(\mathbf{r})\epsilon_{xc}^{hom}(\rho(\mathbf{r})).$$

Here $\epsilon_{xc}^{hom}(\rho(\mathbf{r}))$ is the exchange-correlation energy of a uniform electron gas with electron density $\rho(\mathbf{r})$. In practice, the exchange energy of a homogenous electron gas is given by an explicit expression originally derived by Bloch and Dirac [44]. The correlation part, on the other hand, is represented by an analytic function [45, 46, 47] fitted to accurate quantum Monte-Carlo calculations [48]. In spite of the fact that LDA is only expected to be valid for slowly varying densities, it works surprisingly well for real systems [49].

A natural improvement on the LDA is obtained by adding a density-gradient correction term

$$E_{xc}^{GGA}[\rho] = \int d\mathbf{r} f(\rho(\mathbf{r}), \nabla\rho(\mathbf{r})),$$

where the function f is not uniquely defined and must be chosen with care. In particular the general rules, which a xc functional derived from a physical system obeys, must be imposed by hand. A number of different functionals exists [49, 50, 51, 1] each performing well for specific systems. In this work we use the PW91 [49, 52] or the closely related PBE [50].

2.3 Numerical implementations of DFT

This section deals with a number of important technical details related to the use of DFT for numerical calculations. In particular, a number of approximations (in addition to the inevitable approximation of the xc functional) have to be made. The size of the associated numerical errors relies on a compromise between computational time and accuracy. The inherent uncertainty of the employed xc functional is often used as an upper bound of the numerical errors. In this work two different implementations of DFT have been used: (i) Dacapo [1, 2] which uses plane waves and ultrasoft pseudopotentials [53]. (ii) Siesta [4] which uses a basis of localized pseudoatomic orbitals (PAOs) [5] and norm-conserving pseudopotentials [54]. Detailed reviews of the numerical implementation issues can be found in [55, 56].

2.3.1 Boundary conditions

In order to solve the Kohn-Sham equations and, in general, differential equations one must specify certain boundary conditions. In DFT calculations periodic or vanishing boundary

conditions are the most common choices. The latter, which corresponds to a cluster calculation, is well-suited for describing finite systems like molecules. Periodic boundary conditions, which is used in the supercell approach [55], are convenient for treating infinite systems such as bulk crystals. However, also non-periodic structures can be handled by forming so-called supercells. That is, the system of interest is modeled within a finite (super)cell which is repeated in all directions. Surfaces and molecules can now be modeled by including appropriate vacuum regions in the supercell. In both DACAPO and SIESTA supercells and periodic boundary conditions are applied.

In the supercell approach one can make use of Bloch's theorem for the electronic wave function [57]

$$\psi_{n,\mathbf{k}}(\mathbf{r}) = e^{i\mathbf{k}\cdot\mathbf{r}} u_{n,\mathbf{k}}(\mathbf{r}), \tag{2.9}$$

where $\mathbf{k}$ is a wave vector belonging to the first Brillouin zone (BZ) and $u_{n,\mathbf{k}}$ is a function with the periodicity of the superlattice. Consequently the Hamiltonian is diagonal with respect to the reciprocal lattice vector and one can separately obtain for each $\mathbf{k}$-point the eigenstates of the Hamiltonian. The expectation value of an observable (R) of the system can now be evaluated as an integral over the first Brillouin zone

$$\langle R \rangle = \frac{1}{V_{\mathrm{BZ}}} \int_{\mathrm{BZ}} R(\mathbf{k}) d\mathbf{k} \approx \sum_{\mathbf{k} \in BZ} w_{\mathbf{k}} R(\mathbf{k}),$$

where V_{BZ} is the volume of the first BZ and $R(\mathbf{k}) = \sum_{n \in \mathrm{occ}} \langle \psi_{n,\mathbf{k}} | R | \psi_{n,\mathbf{k}} \rangle$. In practice, the integral is approximated by a weighted sum over $\mathbf{k}$-points. Special $\mathbf{k}$-point sets with efficient sampling have developed [58, 59].

2.3.2 Basis sets

In order to solve the Kohn-Sham equations it is convenient to expand the wave function in terms of a finite basis set. In electronic structure calculations basis functions which either resembles the exact eigenstates of the system (e.g. pseudoatomic orbitals or gaussians) or which are system-independent (e.g. plane waves or wavelets) are usually applied. In the following we focus on plane waves and pseudoatomic orbitals as they are used in DACAPO and SIESTA, respectively.

Plane waves

Expanded in terms of plane waves the Kohn-Sham wave function (2.9) takes the form

$$\psi_{n,\mathbf{k}}(\mathbf{r}) = \sum_{\mathbf{G}} c_{n,\mathbf{k}}(\mathbf{G}) |\mathbf{G} + \mathbf{k}\rangle, \tag{2.10}$$

where $|\mathbf{G} + \mathbf{k}\rangle = \frac{1}{\sqrt{V}} e^{i(\mathbf{G}+\mathbf{k})\cdot\mathbf{r}}$, V is the volume of the supercell and the sum is over reciprocal lattice vectors. In order to truncate the plane wave basis one introduces a cutoff energy (E_{cut}) for the kinetic energy. In this way only plane waves that satisfy the condition $\frac{1}{2}|\mathbf{G} + \mathbf{k}|^2 \leq E_{\mathrm{cut}}$ are retained in the expansion (2.10).

The main advantages of using a plane waves basis set are the following: (i) The result can be systematically converged by increasing the cutoff energy. (ii) No assumptions about the actual shape of the wave function are made. The drawback is that the number of planes waves needed to obtain convergence is very large.

Wannier functions

In order to obtain a set of localized basis functions (which is needed for the transport scheme introduced in chapter 3) the plane waves can be transformed into partly occupied Wannier functions (WF) [3, 60]. These partly occupied Wannier functions are expanded in terms of the M Kohn-Sham eigenstates lying below a selected cutoff energy E_0 and L extra degrees of freedom

$$w_n = \sum_{m=1}^{M} U_{m,n}\psi_m + \sum_{l=1}^{L} U_{M+l,n}\phi_l, \tag{2.11}$$

where the extra degrees of freedom are expanded in terms of the $N - M$ eigenstates with energies above E_0

$$\phi_l = \sum_{m=1}^{N-M} c_{m,l}\psi_{M+m}. \tag{2.12}$$

The Wannier functions are thus constructed such that any eigenstate below the cutoff energy can be exactly represented by a linear combination of WFs. In order to localize the WFs the spread [61]

$$S = \sum_n (\langle w_n|r^2|w_n\rangle - \langle w_n|\mathbf{r}|w_n\rangle^2),$$

is minimized by varying $\mathbf{U}$ and $\mathbf{c}$ in (2.11) and (2.12) under the constraint that $\mathbf{U}$ is unitary and the columns of $\mathbf{c}$ is orthonormal. A detailed account of this scheme for constructing partly occupied Wannier functions are given in Refs. [3, 60].

Pseudoatomic orbitals

For each atom I positioned at $\mathbf{R}_I$ a set of pseudoatomic orbitals are defined as the product of a numerical radial function and a spherical harmonic [62, 5]

$$\phi_{I,lmn}(\mathbf{r}_i) = r_{I,ln}(r_i)Y_{lm}(\mathbf{r}_i). \tag{2.13}$$

Here, $\mathbf{r}_i = \mathbf{r}_i - \mathbf{R}_i$ and the angular momentum is labeled l, m. A "multiple-ζ" basis set consists of several orbitals (labeled n) with the same angular momentum, but different radial dependence. In order to accurately describe the bonding between atoms the so-called polarization functions are often added to the basis set. As the PAOs are required to be zero at a certain radial cutoff they are strictly confined.

The PAOs are the excited orbitals of a free atom and as such the required number of basis functions are much smaller than for a system-independent basis set. On the other hand, there is, in general, no systematic way for increasing the number of basis functions and thus the convergence cannot easily be controlled.

2.3.3 Pseudopotentials

In order to reduce the size of the basis set one often uses pseudopotentials to get rid of the chemically inert core electrons. The idea is to freeze the core electrons in the atomic core states and then replace the potential from the nuclei and core electrons with a softer (pseudo)potential that provides the same description for the valence electrons. In Dacapo and Siesta a parametrization of the ultra soft [53] and norm-conserving [54] pseudopotential method, respectively, is applied

2.4 Dynamics of the nuclei

In the previous sections it has been described, how the electronic ground state corresponding to a given ionic configuration can be calculated. In order to find the equilibrium geometry of a quantum mechanical system one also needs to consider the ionic system described by Eq. (2.3). If the ions are treated as classical particles their motion is determined by the forces, which are defined according to the Hellmann-Feynman theorem as

$$\mathbf{F}_I = -\nabla_{\mathbf{R}_I} E_0(\mathbf{R}_I),$$

that is the ground state energy E_0 in Eq. (2.8) defines a potential energy surface (the Born-Oppenheimer energy surface) for the ions. The equilibrium atomic configuration is then determined from the minimum of this BO energy surface. The nuclear vibrations, in turn, is obtained by diagonalizing the Hessian matrix defined as

$$\frac{\partial^2 E_0(\mathbf{R}_I)}{\partial u_{I\alpha} \partial u_{J\beta}}\Big|_{\mathbf{R}=\mathbf{R}_0},$$

where $u_{I\alpha}$ is the displacement of atom I in the direction α multiplied by the mass factor $\sqrt{M_I}$.

2.4.1 Location of transition states

When considering the dynamics of a quantum mechanical system the reaction rates of certain activated processes are often important. In an activated process the system has to cross an energy barrier to get from the initial to the final state. The reaction rate is then determined by the energy barrier. In this work the activation energy and transition state for a particular reaction has been found using the nudged elastic band method (NEB) [63, 64, 65]. In NEB the initial and final state (provided as input) are connected by a number of images generated with linear interpolation. The images, which are coupled by springs, are then relaxed in a controlled way and the minimum energy path is obtained.

Chapter 3

Quantum Electron Transport

In this chapter we provide an introduction to the basic theoretical framework used for describing electron transport in mesoscopic systems as well as in junctions containing a single atom or molecule.

During the years a variety of numerical methods for describing phase-coherent transport through atomic-sized junctions realistically have been developed. Most of these methods are based on either calculating the scattering wave functions of the system directly [66, 67] or alternatively the single particle Green's function of the central region [19, 20]. In the present work we use the latter method. It is possible to extend both the wave function [68, 69] and the Green's function [70, 71] techniques to include electron-phonon interactions. One of the main advantages of the Green's function approach is that interactions can be included by a systematic expansion [72]. Scattering states on the other hand provide a very useful tool for analyzing the transport properties of a junction. Recently it has been shown that one may derive scattering states efficiently from central region single particle Green's functions [73], hereby combining the advantages of both approaches.

This chapter is organized as follows: First a rather general expression for the current through a nano-scale contact is derived. Then the case of non-interacting electrons where the current formula reduces to the well-known Landauer-Büttiker formula is addressed. This special case is illustrated by a simple example of electron transport through a single electronic level coupled to metallic leads. After considering the Hamiltonian of a system describing interactions between the electronic and the vibrational degrees of freedom, we introduce the electron-phonon interaction explicitly by using the 1BA for the self-energy term. In order to obtain a simple explanation of the Green's function result for inelastic electron transport we then also describe the system in terms of scattering states. Finally the single level system is extended to the case of an electronic level interacting with a single phonon. Appendix A provides a short introduction of the NEGF formalism which forms the mathematical basis of our work.

For clarity we limit the discussion of the general formalism to orthogonal basis sets, while the general case of a non-orthogonal basis is postponed to the description of the implementation using DFT in chapter 4. As we only consider spin-independent Hamiltonians we suppress the spin indices. Atomic units will be assumed throughout this chapter, $e = \hbar = m_e = 1$, unless stated otherwise.

3.1 General Current Formula

This section begins with an introduction to a general framework used for calculating the quantum conductance of a nano-sized constriction. Following Meir and Wingreen [74]

we therefore introduce the non-equilibrium Green's functions (NEGF) technique, which is briefly outlined in Appendix A, and a compact expression for the current formula is derived.

In the following a central region of interacting electrons coupled to two metallic leads is considered. For times $t \leq t_0$ the three regions in Fig. 3.1 are decoupled, each being in local equilibrium. At $t = t_0$ the respective systems are brought into contact and if $\mu_L > \mu_R$ electrons will start to flow from the left lead through the constriction into the right lead. We are concerned with the steady state current the system achieves after a transient period.

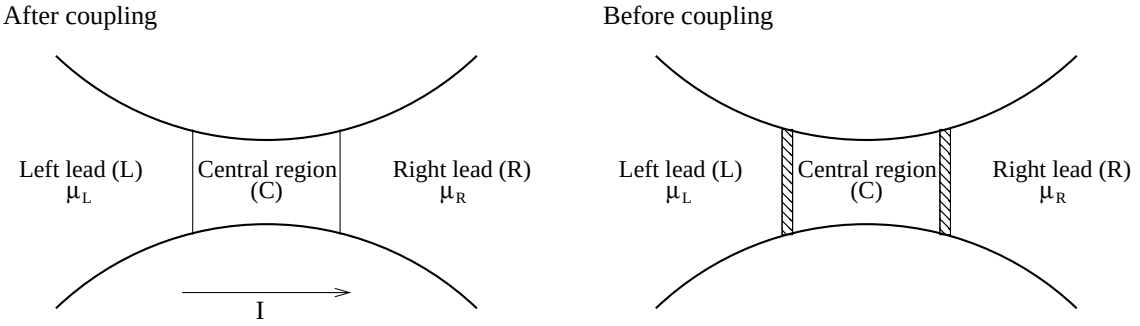

Figure 3.1: Schematics of the system setup used for transport calculations. A central region is coupled to leads assumed to be in local equilibrium and characterized by the chemical potentials $\mu_{L/R}$.

By introducing a orthonormal set of localized orbitals the Hilbert space may be decomposed into three orthogonal subspaces associated with the central region (C), left (L) and right (R) lead respectively. The Hamiltonian of the system can now be written as

$$H(t) = \begin{cases} H_L + H_R + H_C & , t < t_0 \\ H_L + H_R + H_C + V & , t \geq t_0, \end{cases}$$

where

$$H_\alpha = \sum_{i_\alpha, j_\alpha} H_{i_\alpha, j_\alpha} c^\dagger_{i_\alpha} c_{j_\alpha}, \qquad \alpha = L, R, \tag{3.1a}$$

$$H_C = H_C\left[\{c_{i_c}, c^\dagger_{i_c}\}, \{b_q, b^\dagger_q\}\right], \tag{3.1b}$$

$$V = \sum_{i_\alpha, j_c} \left[V_{i_\alpha, j_c} c^\dagger_{i_\alpha} c_{j_c} + V^*_{i_\alpha, j_c} c^\dagger_{j_c} c_{i_\alpha}\right]. \tag{3.1c}$$

H_α describes the electrons in the metallic lead α as non-interacting particles moving in a mean-field potential. The Hamiltonian for the central region (H_C) is written in a general form, so that it can contain both electron-electron interactions as well as coupling to external degrees of freedom such as atomic vibrations. V describes the coupling between the central region and the leads. The coupling term is quadratic in the field operators as we neglect interactions between electrons in the leads and the central region. This is justified by the strong screening provided by the metallic leads. We also ignore the direct coupling between leads L and R. Due to the highly localized nature of the basis functions this latter approximation can always be met by increasing the size of the central region.

The particle current (per spin) flowing into the central region from lead α is given by the time derivative of the lead number operator

$$\begin{aligned} I_\alpha(t) &= -i\big\langle [H, N_\alpha](t)\big\rangle \\ &= i\sum_{i_\alpha, j_c}\Big[V_{i_\alpha, j_c}\big\langle c^\dagger_{i_\alpha}(t)c_{j_c}(t)\big\rangle - V^*_{i_\alpha, j_c}\big\langle c^\dagger_{j_c}(t)c_{i_\alpha}(t)\big\rangle\Big], \end{aligned}$$

where i_α and j_c refers to basis functions in lead α and the central region, respectively. The expectation values are taken with respect to the state operator of the uncoupled system while the time evolution is governed by the full Hamiltonian. We recognize the expectation values as the equal time lesser Green's functions, $G^<_{i_\alpha, j_c}(t,t)$ and $G^<_{j_c, i_\alpha}(t,t)$. One can derive Dyson equations for the contour ordered counterparts by using the equation-of-motion technique (see Appendix A). The Langreth rules [75] for analytic continuation is then used to obtain expressions for the relevant real-time lesser GF's. Under steady-state conditions these Green's functions only depend on the time difference $t - t'$ and by performing a Fourier transform and using the relation $\mathbf{G}^r - \mathbf{G}^a = \mathbf{G}^> - \mathbf{G}^<$, we finally arrive at a compact expression for the particle current originating from lead α

$$I_\alpha = \frac{2e}{\hbar}\int\frac{d\varepsilon}{2\pi}\mathrm{Tr}\big[\mathbf{\Sigma}^<_\alpha(\varepsilon)\mathbf{G}^>_C(\varepsilon) - \mathbf{\Sigma}^>_\alpha(\varepsilon)\mathbf{G}^<_C(\varepsilon)\big]. \tag{3.2}$$

We note, that at this point units have been re-introduced and we have multiplied by a factor 2 due to spin degeneracy. The trace is taken over basis functions belonging to the central region, the bold face quantities indicate matrices and $\mathbf{\Sigma}_\alpha$ denotes the self-energy for the coupling to lead α. The full Green's functions of the central region obey the Dyson and Keldysh equations [76]

$$\mathbf{G}^r_C(\varepsilon) = \mathbf{G}^{0,r}_C(\varepsilon) + \mathbf{G}^{0,r}_C(\varepsilon)\left[\mathbf{\Sigma}^r_L(\varepsilon) + \mathbf{\Sigma}^r_R(\varepsilon) + \mathbf{\Sigma}^r_{\mathrm{int}}(\varepsilon)\right]\mathbf{G}^r_C(\varepsilon), \tag{3.3a}$$

$$\mathbf{G}^\lessgtr_C(\varepsilon) = \mathbf{G}^r_C(\varepsilon)\left[\mathbf{\Sigma}^\lessgtr_L(\varepsilon) + \mathbf{\Sigma}^\lessgtr_R(\varepsilon) + \mathbf{\Sigma}^\lessgtr_{\mathrm{int}}(\varepsilon)\right]\mathbf{G}^a_C(\varepsilon), \tag{3.3b}$$

where $\mathbf{G}^{0,r}_C(\varepsilon)$ denotes the retarded electronic single-particle Green's function of the uncoupled central region. The self-energy has hereby been divided into a term due to the interactions and two terms describing the coupling to the leads. As a complete separation of the two perturbations is not possible $\mathbf{\Sigma}_{\mathrm{int}}$ will also contain contributions from the coupling between the central region and the leads.

The self-energy due to the lead coupling is related to the Green's function of the uncoupled lead as

$$\left[\mathbf{\Sigma}_\alpha(\varepsilon)\right]_{i_c, j_c} = \sum_{m_\alpha, n_\alpha} V_{i_c, m_\alpha} g^0_{m_\alpha, n_\alpha}(\varepsilon) V^*_{n_\alpha, j_c}. \tag{3.4}$$

By using the fluctuation-dissipation theorem the lead self-energies can be written as

$$\mathbf{\Sigma}^\lessgtr_\alpha(\varepsilon) = \begin{cases} i n_F(\varepsilon - \mu_\alpha)\mathbf{\Gamma}_\alpha(\varepsilon) \\ i\left[n_F(\varepsilon - \mu_\alpha) - 1\right]\mathbf{\Gamma}_\alpha(\varepsilon) \end{cases},$$

where $n_F(\varepsilon)$ is the Fermi distribution function and

$$\mathbf{\Gamma}_\alpha(\varepsilon) = i\left[\mathbf{\Sigma}^r_\alpha(\varepsilon) - \mathbf{\Sigma}^a_\alpha(\varepsilon)\right] = i\left[\mathbf{\Sigma}^>_\alpha(\varepsilon) - \mathbf{\Sigma}^<_\alpha(\varepsilon)\right],$$

is the broadening of the electronic states located in the central region due to the coupling to lead α.

The general current formula (3.2) can be interpreted as the net flow of electrons from the lead α into the central region C: The lead self-energy $\mathbf{\Sigma}^<_\alpha$ ($\mathbf{\Sigma}^>_\alpha$) represents the rate of electrons scattering into (out of) C. Further $\mathbf{G}^>_C$ ($\mathbf{G}^<_C$) expresses the availability of empty (occupied) states in C.

3.2 Phase-coherent Transport

In this section we consider the case of phase-coherent transport where the general current formula (3.2) reduces to the Landauer-Büttiker formula [77].

In the phase-coherent regime the electrons behave as weakly interacting quasi-particles with a life time, which is much longer than the average time an electron spend in the central region. The central region Hamiltonian, H_C in (3.1b), is then approximated by an effective single particle Hamiltonian. In the phase-coherent case the self-energy term entering the Green's functions of the central region (3.3) is only composed of the lead contributions, i.e. $\mathbf{\Sigma} = \mathbf{\Sigma}_L + \mathbf{\Sigma}_R$. Substituting the resulting expressions of the central region GFs into the symmetrized current formula, $I = (I_L - I_R)/2$, leads to the following compact expression

$$I = \frac{2e}{h} \int \left[n_F(\varepsilon - \mu_L) - n_F(\varepsilon - \mu_R) \right] T(\varepsilon) d\varepsilon, \tag{3.5}$$

where the elastic transmission function is defined as

$$T(\varepsilon) = \mathrm{Tr}\left[\mathbf{G}_C^r(\varepsilon) \mathbf{\Gamma}_L(\varepsilon) \mathbf{G}_C^a(\varepsilon) \mathbf{\Gamma}_R(\varepsilon) \right]. \tag{3.6}$$

In the limit of small bias and low temperature, the conductance $G = dI/dV$ becomes

$$G = G_0 T(\varepsilon_F), \tag{3.7}$$

where the quantum conductance unit is given by $G_0 = 2e^2/h$. The transmission coefficient matrix, $\mathbf{t}(\varepsilon)$, as defined within Landauer-Büttiker theory, is related to the GFs by $\mathbf{t}(\varepsilon) = \left[\mathbf{\Gamma}_\mathrm{R}(\varepsilon)\right]^{1/2} \mathbf{G}_\mathrm{S}^r(\varepsilon) \left[\mathbf{\Gamma}_\mathrm{L}(\varepsilon)\right]^{1/2}$, showing the equivalence of Eq. (3.7) to the Landauer-Büttiker formula [78].

When studying the transport mechanism of a particular system, it is often very useful to decompose the total conductance into contributions from the individual eigenchannels [79, 80]. Eigenchannels are defined as separate non-mixing scattering states with well-defined transmission probabilities, $0 \leq \mathcal{T}_n \leq 1$. That is, an electron in eigenchannel $\psi_{Lp}(\varepsilon)$ is injected from the left lead in mode p and is transmitted (reflected) upon elastic scattering in the central region with probability $\mathcal{T}_{Lp}(\varepsilon)$ ($\mathcal{R}_{Lp}(\varepsilon)$). In terms of eigenchannels the Landauer-Büttiker formula takes the form

$$G = G_0 \sum_p \mathcal{T}_{Lp}(\varepsilon_F) = G_0 \sum_q \mathcal{T}_{Rq}(\varepsilon_F). \tag{3.8}$$

In the NEGF approach the eigenchannel transmissions are obtained directly as the non-negligible eigenvalues of the transmission matrix (3.6). In Ref. [73] a straight forward procedure for determining the eigenchannels within the NEGF formalism is presented, which makes it possible to calculate the eigenchannels efficiently and directly from the central region Green's function.

A different strategy for investigating the conduction mechanism consists in directly removing particular molecular orbitals from the basis set of the transmission Hamiltonian. Hereby, when neglecting interference effects, the conduction contribution from individual orbitals can be studied [19, 10].

3.2.1 Transport through a Single Level

To gain further insight into the NEGF formalism for calculating the stationary electron transport from one reservoir through a quantum conductor and into a second reservoir, we

consider the simplest case, namely a single level coupled to continuous bands. As outlined in Refs. [10, 81] this model system is well-suited as a starting point for analysis of the transport properties of more complicated molecular junctions.

For this purpose we consider the Newns-Anderson model [82] and introduce a single molecular state $|\phi_c\rangle$ located in the central region with energy ε_c coupled to left and right semi-infinite leads via the matrix elements $v_{n_\alpha} = \langle\phi_c|H|\phi_{n_\alpha}\rangle$, where $|\phi_{n_\alpha}\rangle$ denotes an orthonormal basis for lead α. The retarded Green's function for the central region reduces to

$$G_c^r(\varepsilon) = \frac{1}{\varepsilon - \varepsilon_c - \Sigma_L(\varepsilon) - \Sigma_R(\varepsilon)},$$

where Σ_α is the self-energy due to the lead α given in Eq. (3.4). By introducing the group orbital a particular elegant solution to the problem is obtained [19]. The group orbital is defined as the orthogonal projection of the state $H|\phi_c\rangle$ onto the subspace spanned by the lead states

$$|g_\alpha\rangle = \frac{1}{V_\alpha}\sum_{n_\alpha} v_{n_\alpha}|\phi_{n_\alpha}\rangle,$$

where $V_\alpha = (\sum_{n_\alpha}|v_{n_\alpha}|^2)^{1/2}$ is a normalization constant. The group orbital is a linear combination of basis functions located in lead α with the weights given by the corresponding coupling strength. As a consequence the group orbital is expected to be localized near the molecular state on the level-lead interface. Another property of $|g_\alpha\rangle$ is that the molecular state only couples to the lead via the group orbital. Therefore the self-energy takes the particular simple form $\Sigma_\alpha = |V_\alpha|^2 g_{g_\alpha}^{0,r}$, with $g_{g_\alpha}^{0,r}$ being the Green's function of the group orbital in the uncoupled system. By using these properties in combination with the general relation between a diagonal element of the retarded Green's function and the projected density of states (DOS), $\mathrm{Im}\,[G_{n,n}] = -\pi\rho_n$, it can be shown that in the case of symmetric coupling the transmission function (3.6) becomes

$$T(\varepsilon) = 2\pi^2|V|^2\rho_c(\varepsilon)\rho_g^0(\varepsilon). \tag{3.9}$$

We notice that the transmission at a given energy depends on the coupling strength, the density of states of the molecular level and the DOS of the group orbital in the uncoupled lead. Consequently if an electron should move from the left lead through the molecular orbital and into the right lead there should be states available in the lead which match the energy ε of the level (or are within the level broadening) and the coupling should be sufficiently strong.

3.3 Inelastic Transport

In the following we consider electron transport through a central region with electron-phonon interactions. To this end we need the full Green's functions (3.3) where the electron-phonon interaction enters as a self-energy term. The methodology presented below follows the same lines as Frederiksen *et al.* in Ref. [70].

The Hamiltonian of the system is given by

$$H = H_{\mathrm{ph}} + H_{\mathrm{el}} + H_{\text{el-ph}}$$

where

$$H_{\text{ph}} = \sum_{\lambda} \hbar\omega_{\lambda}(b_{\lambda}^{\dagger}b_{\lambda} + \frac{1}{2}), \tag{3.10a}$$

$$H_{\text{el}} = \sum_{i,j} H_{ij}c_i^{\dagger}c_j, \tag{3.10b}$$

$$H_{\text{el-ph}} = \sum_{\lambda}\sum_{i,j} M_{i,j}^{\lambda}c_i^{\dagger}c_j(b_{\lambda}^{\dagger} + b_{\lambda}). \tag{3.10c}$$

Here $b_{\lambda}^{\dagger}/b_{\lambda}$ ($c_i^{\dagger}/c_i$) creates/destroys a phonon in mode λ (an electron in state i). $H_0 = H_{\text{ph}} + H_{\text{el}}$ naturally arises from the Born-Oppenheimer (BO) approximation, which states that due to the large mass difference between electrons and ions the dynamics of the system may be decoupled into an electronic and ionic part. This means that the electrons are considered as responding instantaneously to changes in the ionic positions. The ions will thus move in an effective potential given by the ground state of the electrons. Seen from another perspective the electrons move in a self-consistent potential corresponding to the static arrangement of ions. More rigorously the BO approximation expresses that an electron remains in state i as the ions move, i.e. the electronic states do not couple.

By further assuming small ionic displacements, the harmonic approximation can be used to describe the nuclear motion as a sum of independent oscillators (3.10a). For systems without translational invariance this can be shown by expanding the ionic Hamiltonian to second order in the displacements and introducing the normal mode coordinates, $\{\mathbf{Q}, \mathbf{P}\}$, together with the usual canonical quantizations of the position and momentum operators.

H_{el} (3.10b) is a single-particle Hamiltonian describing non-interacting electrons moving in the static equilibrium structure of the ions. The effective potential (V_{eff}) felt by the electrons includes a mean-field approximation for the electron-electron interaction as well as interactions with the fixed ions.

To go beyond the BO approximation and study interactions between electrons and moving ions we expand the effective potential (V_{eff}) to first order in the ionic displacements. The electron-phonon Hamiltonian (3.10c) is then obtained by the coordinate transformation described above. The electron-phonon coupling matrix ($\mathbf{M}^{\lambda}$) entering Eq. (3.10c) is given by

$$M_{i,j}^{\lambda} = \sum_{I} \sqrt{\frac{\hbar}{2M_I\omega_{\lambda}}} \langle \phi_i(\mathbf{r}) | W_I^{\lambda} | \phi_j(\mathbf{r}) \rangle, \tag{3.11}$$

where the index I runs over all dynamic ions and the displacement potential, $W_I^{\lambda} = \nabla V_{\text{eff}}\left[\{\mathbf{R}_i\}\right](\mathbf{r}) \cdot \mathbf{Q}_I^{\lambda}$, is the derivative of the effective electronic potential in the direction defined by the normal mode λ. It is noted that $M_{i,j}^{\lambda}$ gives the probability amplitude for an electron in state ϕ_j to be scattered into state ϕ_i accompanied by the emission (absorption) of a phonon in mode λ.

3.3.1 The Born Approximation

When allowing for electron-phonon interactions in the central region the question naturally arises whether to study the influence of the interaction on the electrons or on the phonons first [83, 84, 85]. Again the large mass difference between electrons and ions provides a straight-forward answer. First one must solve the problem for the bare electronic Green's functions taking the ions to be fixed at their equilibrium positions. Next the influence of the bare electron states on the phonon Green's functions should be incorporated and

afterwards the effect of the renormalized phonon states on the electronic GF should be calculated. In spite of that, we will in the following only study the influence of the interaction on the electronic GFs, simply assuming phonons can be described by the non-interacting phonon GFs (3.12) and take the parameters ω_λ and $\mathbf{M}_\lambda$ to be the renormalized ones. As we use a self-consistent density functional theory (DFT) calculation to determine the vibrational frequency (ω_λ) and the coupling matrix element ($\mathbf{M}_\lambda$) both parameters will include a renormalization due to electronic screening effects. It is noted that, by utilizing this approximation for the phonon Green's function we neglect an eventual reduction of the phonon life time.

As we only study the interactions between electrons and atomic vibrations localized in the central region we disregard the phonon self-energy term due to the coupling to the left and right regions [70]. As a consequence, the vibrational degree of freedom is described by free phonon Green's functions

$$D^{0,r}(\lambda,\omega) = \frac{1}{\omega-\omega_\lambda+i\eta} - \frac{1}{\omega+\omega_\lambda+i\eta}, \tag{3.12a}$$

$$D^{0,\lessgtr}(\lambda,\omega) = -2\pi i\left[\langle n_\lambda\rangle\delta(\omega\mp\omega_\lambda) + (\langle n_\lambda\rangle+1)\delta(\omega\pm\omega_\lambda)\right], \tag{3.12b}$$

where $\langle n_\lambda\rangle$ is the expectation value of the occupation in phonon mode λ and ω_λ is the renormalized phonon frequency. For weak electron-phonon coupling the phonon occupation can be approximated by the steady-state solution to a rate equation describing the heating of the central region [86]. From this two regimes can be identified; (i) the externally damped limit and (ii) the externally undamped limit. In the following we consider the externally damped limit where the vibrations are strongly damped by coupling to a heat bath. The occupation is then simply given by the Bose-Einstein distribution. Throughout this work we assume a zero-phonon temperature which corresponds to setting the number of phonons to zero [27].

Writing up the perturbation expansion for the electronic Green's function the lowest order self-energy terms are the "Hartree" and "Fock" diagrams (both shown in Fig. 3.2). In the first Born approximation (1BA) the electron self-energy term originating from the electron-phonon interaction is approximated by these diagrams.

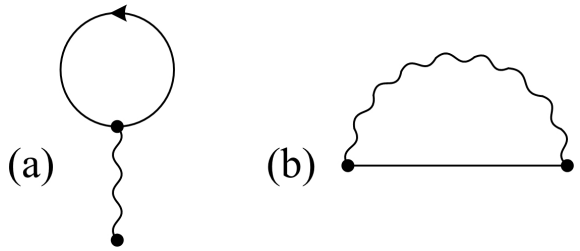

Figure 3.2: Diagrammatic representation of the lowest order terms in the perturbation expansion for the electronic Green's function in a coupled electron-phonon system. In the first Born approximation the "Hartree" (a) and "Fock" (b) diagrams dress the unperturbed electronic Green's function (plain line). The renormalization of the phonons Green's function (wiggly line) due to the electron-phonon interaction is only taken into account on the level of DFT.

In order to obtain the real time versions of the self-energies due to the electron-phonon interaction we use the Feynman rules to evaluate the contour-ordered diagrams and afterwards the Langreth rules for analytic continuation. In this way we find for the "Hartree"

diagram

$$\mathbf{\Sigma}^{H,\lessgtr}_{\mathrm{ph},\lambda}(\varepsilon) = 0, \tag{3.13a}$$

$$\mathbf{\Sigma}^{H,r}_{\mathrm{ph},\lambda}(\varepsilon) = i\sum_{\lambda}\frac{1}{\pi\omega_\lambda}\int_{-\infty}^{\infty}\mathbf{M}^{\lambda}\mathrm{Tr}\left[\mathbf{G}^{0,<}(\varepsilon')\mathbf{M}^{\lambda}\right]d\varepsilon', \tag{3.13b}$$

where $\mathbf{G}^0(\varepsilon)$ denotes an electronic Green's function calculated without the electron-phonon interaction but including the self-energy due to the coupling to the leads. As seen from Eq. (3.13a) the lesser/greater part doesn't contribute to the phonon self-energy. This is due to energy conservation which implies that the wiggly line corresponds to a factor $d^{\lessgtr}(\lambda, \varepsilon' = 0) = 0$. The retarded part (3.13b) gives an energy-independent contribution to the phonon self-energy and thus no signal at the phonon threshold voltage. The term can be understood as a static phonon-induced change in the mean-field electronic potential originating from the polarization response of the vibrating atoms [87]. In order to properly account for this static potential shift it must be included in the DFT self-consistency loop for calculating the mean-field potential. In doing so we expect this small static contribution to the potential to be at least partially screened. Consequently we will, as often done, omit this term from the electron-phonon self-energy [70, 88]. It is noted that, when studying phenomena for which the polaron shift of the levels are important it is essential to include the retarded "Hartree" self-energy [89].

For the "Fock" term we find

$$\mathbf{\Sigma}^{F,\lessgtr}_{\mathrm{ph},\lambda}(\varepsilon) = \mathbf{M}^{\lambda}\mathbf{G}^{0,\lessgtr}_{C}(\varepsilon \pm \omega_\lambda)\mathbf{M}^{\lambda}, \tag{3.14a}$$

$$\mathbf{\Sigma}^{F,r}_{\mathrm{ph},\lambda}(\varepsilon) = \frac{1}{2}\left[\mathbf{\Sigma}^{>}_{\mathrm{ph},\lambda}(\varepsilon) - \mathbf{\Sigma}^{<}_{\mathrm{ph},\lambda}(\varepsilon)\right] - \frac{i}{2\pi}\int\frac{\mathbf{\Sigma}^{>}_{\mathrm{ph},\lambda}(\varepsilon') - \mathbf{\Sigma}^{<}_{\mathrm{ph},\lambda}(\varepsilon')}{\varepsilon' - \varepsilon}d\varepsilon', \tag{3.14b}$$

where the last equation follows from the general identity $\mathbf{G}^r - \mathbf{G}^a = \mathbf{G}^> - \mathbf{G}^<$ together with the Kramers-Kronig relations between Re $\mathbf{\Sigma}^r$ and Im $\mathbf{\Sigma}^r$. We notice that, as a consequence of the assumption of $\langle n_\lambda \rangle = 0$ no phonons are present in the central region and therefore electrons can only loose energy during a scattering event.

The self-consistent Born approximation (SCBA) is obtained by replacing the bare electronic Green's functions in the "Fock" self-energy diagram with the full ones. Hereby a wider subclass of diagrams are included in the perturbation expansion. It is noted that in contrast to the 1BA the SCBA is a current conserving approximation [90]. In spite of this rather unphysical feature of the 1BA we will utilize this approximation when studying the inelastic transport characteristics of atomic junctions. The level of approximation is justified by tight-binding results indicating that for strongly coupled systems the difference between SCBA and 1BA is nearly non-existent [91]. By using the 1BA we achieve a reduction in the computational costs since a self-consistency loop can be omitted when calculating the self-energies.

Another scheme for reducing the computational costs when exploring the consequences of the electron-phonon interaction is the lowest order expansion (LOE). Here the Green's functions and coupling self-energies are assumed to be energy-independent [86, 92, 93]. In LOE the current expression consists of three terms: (i) the Landauer-Büttiker term, Eq. (3.7), corresponding to phase-coherent transport of the electrons, (ii) a symmetric term giving rise to steps in the conductance curve at the vibrational energies, (iii) an asymmetric term which vanishes for geometrically symmetric contacts.

3.3.2 Scattering Theory

In this section we use scattering theory to give a simplified description of how interactions between the conduction electrons and the atomic vibrational degrees of freedom affects the conductance. By using the first Born approximation, the scattering formalism offers a simple and physically appealing explanation of the NEGF results. A comprehensive introduction to scattering theory can be found in [94, 95].

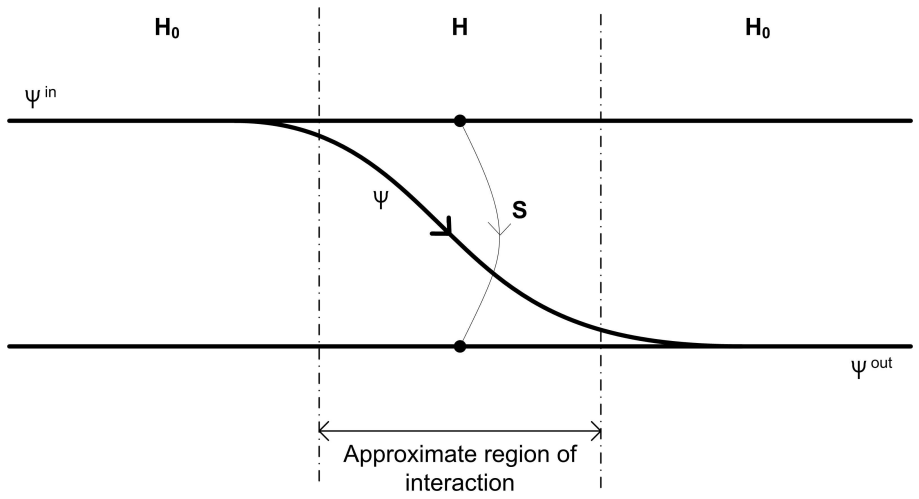

Figure 3.3: The scattering operator S maps the in-asymptote $U_0(t)|\psi^{\text{in}}\rangle$ onto the out-asymptote $U_0(t)|\psi^{\text{out}}\rangle$, thereby avoiding any reference to the actual (and for experiments irrelevant) state vector, $U(t)|\psi\rangle$. Outside the approximate region of interaction the time evolution of the scattering states are governed by the simple Hamiltonian H_0.

The scattering of a free electron by some fixed atom or the mutual scattering of two free particles are typical scenarios which are well described within scattering theory. In general the Hamiltonian of the system is written in the form

$$H = H_0 + V,$$

where H_0 is translationally invariant and quadratic in the field operators and the localized scattering event is described by V.

During a typical scattering event the time evolution of the state vector[1], $U(t)|\psi\rangle$, can be divided into three parts:

(1) The approach of the particle long before the actual collision occurs. Experimentally the evolution of the state vector is indistinguishable from that of the so-called in-asymptote. In general, the in-asymptote $|\psi_{in}\rangle$ is defined by the limit $U(t)|\psi\rangle \rightarrow U_0(t)|\psi^{\text{in}}\rangle$ for $t \rightarrow -\infty$. That is, well before the collision occurs $U(t)|\psi\rangle$ behaves like a free wave packet (the in-asymptote) localized far away from the scattering center. In practice, the in-asymptote is often constructed from the stationary scattering states which are improper eigenstates of the free Hamiltonian H_0.

(2) The scattering event where the interaction causes the actual wave packet to diverge from the in-asymptote.

[1]The time evolution of any state vector is, in general, determined by the time-dependent Schrödinger equation $i\frac{d}{dt}|\psi(t)\rangle = H|\psi(t)\rangle$. Formally the solution can be expressed as $|\psi(t)\rangle = U(t)|\psi\rangle$. For conservative systems, where H is independent of time, the time evolution operator can be written as $U(t) = e^{-iHt}$.

(3) The departure of the particle. The full wave function is now approaching some other free wave packet, the out-asymptote (defined as $U(t)|\psi\rangle \to U_0(t)|\psi^{\text{out}}\rangle$ for $t \to +\infty$).

As seen from their definition the in- (out-) asymptote is, in principle, only identical with the full wave function when $t \to -\infty$ ($t \to \infty$). In practice, however, the respective asymptotes will be indistinguishable from the full wave function outside the approximate region of interaction (see Fig. 3.3). Experimentally, only the asymptotes will be observed because a typical collision time for quantum scattering is on the order of nano seconds.

For the interpretation of such experiments the asymptotes can, with no reference to the actual state vector, be related through the scattering operator

$$|\psi^{\text{out}}\rangle = S|\psi^{\text{in}}\rangle. \tag{3.15}$$

Further the probability amplitude that, a particle entering the collision with in-asymptote $|\psi^{\text{in}}\rangle$ will leave it with out-asymptote $|\psi^{\text{out}}\rangle$ is given as

$$\langle\psi^{\text{out}}|S|\psi^{\text{in}}\rangle = \langle\psi^{\text{out}}|\psi^{\text{in}}\rangle - 2\pi i\delta(E_{\text{out}} - E_{\text{in}})\langle\psi^{\text{out}}|T(E_{\text{in}} + i0^+)|\psi^{\text{in}}\rangle, \tag{3.16}$$

where $T(z) = V + V\mathbf{G}^0(z)T(z)$ is the T operator. The first term in (3.16) represents the probability that the particle leaves the region of interaction without being scattered. The second term is the amplitude for the particle to become scattered, where the delta function is added as the total energy must be conserved during the interaction. The expectation value is easily generalized to cover the scattering of two particles, where the asymptotes would then simply be interpreted as eigenstates of the two-particle system and the energies as the total energies of the combined system.

For weak interactions one often applies the first Born approximation for the T operator, where T is replaced by the interaction part of the Hamiltonian (V).

Having set the general framework we now consider the scattering of a single electron by a molecule in its vibrational ground state.

In the following $H_{\text{el-ph}}$ (3.10c) is regarded as a perturbation to $H_0 = H_{\text{el}} + H_{\text{ph}}$. The asymptotic states of the combined system are constructed as products of scattering states of the electronic and phonon systems. For convenience we chose the scattering states of H_{el} as the eigenchannels incident on the molecule from the left, $|\psi_{Lp}\rangle$, or right, $|\psi_{Rq}\rangle$ (see the discussion following Eq. (3.8)). The actual electronic asymptotic states are then corresponding to a wave packet constructed from the states $|\psi_{\alpha p}\rangle$ in a narrow interval around the energy ε, initially located far from the molecule in lead α[2]. The state of the molecule is specified by the number of phonons in each mode, $|\mathbf{n}\rangle$. The asymptotes of the full wave function is now written as $|\Psi\rangle = |\psi_{\alpha q};\mathbf{n}\rangle$.

We assume that $eV = \mu_L - \mu_R > 0$ and consider an asymptotic in state of the form, $|\Psi^{\text{in}}\rangle = |\psi_{Lp};\mathbf{0}\rangle$. The state corresponds to an electron incident on the junction from the left in channel p with energy $\mu_R < \varepsilon < \mu_L$ and the molecule in its vibrational groundstate, $|\mathbf{0}\rangle$. In the first Born approximation (3.16) we now have the transition amplitudes

$$\langle\psi_{\alpha q};\mathbf{n}|S|\psi_{Lp};\mathbf{0}\rangle \approx \langle\psi_{\alpha q};\mathbf{n}|\psi_{Lp};\mathbf{0}\rangle - 2\pi i\delta(E_{\text{out}} - E_{\text{in}})\langle\psi_{\alpha q};\mathbf{n}|\hat{H}_{\text{el-ph}}|\psi_{Ln};\mathbf{0}\rangle. \tag{3.17}$$

By using the completeness relation for the asymptotic out states and Eqs. (3.10c), (3.15)

[2]For future convenience and as Eq. (3.16) is fullfilled for the improper scattering states $|\psi_{\alpha p}\rangle$ we will just use those in the following expressions.

and (3.17) the out state can be expressed as

$$\begin{aligned} |\Psi^{\text{out}}\rangle &= \sum_{\alpha q,\mathbf{n}} |\psi_{\alpha q};\mathbf{n}\rangle\langle\psi_{\alpha q};\mathbf{n}|S|\psi_{Lp};\mathbf{0}\rangle \\ &= C_p\Big[|\psi_{Lp}(\varepsilon);\mathbf{0}\rangle + \sum_{q,\lambda}{}' c_{pq}^{\lambda}|\psi_{Rq}(\varepsilon-\omega_\lambda);1_\lambda\rangle\Big], \end{aligned} \tag{3.18}$$

where the expansion coefficients are

$$c_{pq}^{\lambda} = D_{Rq}(\varepsilon-\omega_\lambda)\langle\psi_{Rq}(\varepsilon-\omega_\lambda)|W^{\lambda}(\mathbf{r})|\psi_{Lp}(\varepsilon)\rangle. \tag{3.19}$$

Here $D_{Rq}(\varepsilon)$ is the electronic density of states for channel Rq and W^λ is the displacement potential for mode λ. The normalization constant, $C_p = (1+\sum_{q,\lambda}{}' |c_{pq}^{\lambda}|^2)^{-1/2}$, has been introduced because the first Born approximation is not a unitary approximation to S.

The prime in the sum in (3.18) means that only modes with $\omega_\lambda < eV$ are included. This and the fact that only states coming from the right electrode are included in the sum in (3.18) is a simple consequence of the Pauli exclusion principle [41]. It is noted that we have invoked the ansatz that the populations of the electronic scattering states can be described by the equilibrium Fermi distributions. An alternative approach is to determine the non-equilibrium electron distributions self-consistently imposing particle conservation as a constraint [68, 96].

From the second term of Eq. (3.18), which gives the amplitude for scattering, it is seen that (at least in the first Born approximation), a scattering event leaves the molecule in its first vibrational state whereas the electron is back-scattered with lowered energy.

In the elastic case the probability for an electronic wave packet constructed from the state $|\psi_{Lp}\rangle$ to make it into the right electrode and thereby contribute to the current is $\mathcal{T}_{Lp}(\varepsilon_F)$. In contrast an electronic wave packet constructed from the scattered state (3.18) makes it to the right electrode only with probability

$$P_p = |C_p|^2\Big[\mathcal{T}_{Lp}(\varepsilon_F) + \sum_{q,\lambda}{}' |c_{pq}^{\lambda}|^2\mathcal{R}_{Rq}(\varepsilon_F)\Big],$$

where it is assumed that $\mathcal{T}$ and $\mathcal{R}$ varies little on the scale of ω. From the Landauer-Büttiker formula the total change in conductance due to the inelastic scattering is obtained

$$\Delta G = G_0\sum_p |C_p|^2\sum_{q,\lambda}{}' |c_{pq}^{\lambda}|^2\Big[\mathcal{R}_{Rq}(\varepsilon_F) - \mathcal{T}_{Lp}(\varepsilon_F)\Big]. \tag{3.20}$$

From this follows that the change in conductance due to the inelastic scattering with a given mode λ involves all pairs of electronic channels for which the electron-phonon matrix element, $\langle\psi_{Lp}|W^\lambda(\mathbf{r})|\psi_{Rq}\rangle$, is non-zero. The physical argument underlying Eq. (3.20) is illustrated in Fig. 3.4. We note that by using a generalized Landauer-Büttiker picture Imry *et al.* [97] found a similar result for the linear conductance with inelastic scattering.

The formula for the total change in conductance was derived under the assumptions of weak electron-phonon interaction and instantaneous cooling of the phonons, assumptions which also underlies the NEGF results. Apart from these approximations we also invoked the ansatz that the occupation of the scattering states can be described by the equilibrium Fermi distributions.

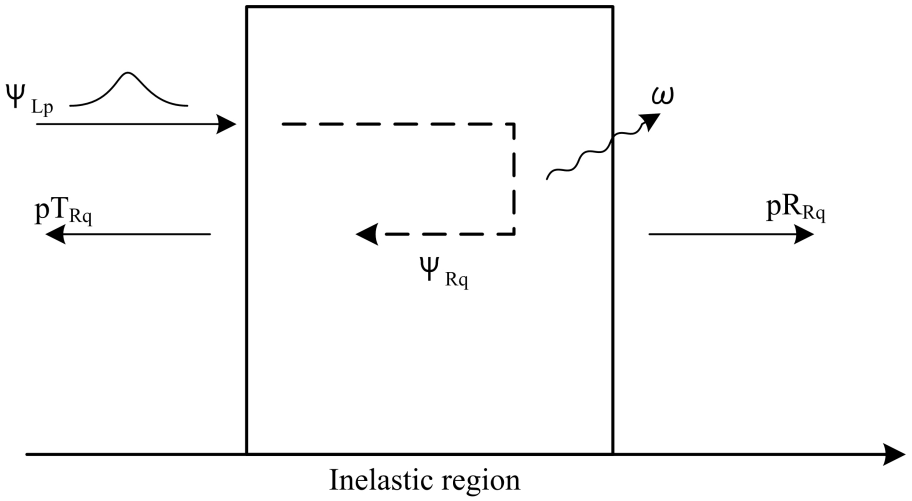

Figure 3.4: An electron incident on the central region from the left described by a wave packet constructed from states ψ_{Lp} will upon inelastic scattering end up in a state ψ_{Rq}. This follows from energy conservation and the Pauli principle. The probability for the electron to enter the right electrode is consequently changed from $\mathcal{T}_{Lp}$ to $\mathcal{R}_{Rq}$. The total change in conductance (3.20) now follows by summing over all possible incoming and outgoing states. The special case of a single scattering channel discussed in Sec. 3.3.3 simply follows by restricting the summation to one channel.

3.3.3 Transport through a Single Level Revisited

In order to illustrate and develop a physical understanding of the general formalism for including electron-phonon interaction in the current calculation, we consider a single level coupled to a left and a right lead. This electronic level interacts with a localized vibration with frequency, ω. As seen from Eq. (3.9) the junction supports a single scattering channel at the Fermi energy with a transmission probability of $\mathcal{T} = |t(\varepsilon_F)|^2$. At low temperatures the dynamical atoms sits in their vibrational ground state and the electron can only loose the energy ω during a scattering event. Assuming a bias voltage $eV = \mu_L - \mu_R > \omega$ an electron incident on the level from the left with an energy just below μ_L, must end up in a left moving scattering state after interacting with a phonon. This follows from energy conservation and the Pauli principle. Upon inelastic scattering, the probability for the electron to enter the right electrode is thus changed from $\mathcal{T}$ to $\mathcal{R} = 1 - \mathcal{T}$. Consequently, the change in conductance due to the electron-phonon interaction should be proportional to $1-2\mathcal{T}$, i.e. an increase (decrease) in the conductance is expected for $\mathcal{T} < 0.5$ ($\mathcal{T} > 0.5$). The same conclusion has been reached using the LOE [86, 92, 93]. Recently the theoretical conclusions have been supported by measurements on Pt-H_2O junctions [98].

We notice that within the LOE the direction of the change in conductance for a single level model depends on both the elastic transmission and the asymmetry factor (Γ_R/Γ_L) [99]. In fact the transition is in general determined by all parameters [100]. From Eq. (3.20) it is seen that our scattering result for the conductance change does not capture this dependence on the asymmetry of the contact.

Chapter 4

NEGF-DFT formalism

Since the transport properties of molecular electronics devices are expected to be sensitive to the details of the atomic structure, a combination of the general transport formalism described in chapter 3 and a first principle description of the electronic structure is necessary for making our results useful for a comparison with experiments. Therefore we describe in this chapter how the NEGF approach can be combined with Kohn-Sham density functional theory (DFT) to provide a model for electron transport.

The NEGF-DFT formalism offers a numerically efficient way of evaluating the current due to electrons moving in the effective Kohn-Sham potential. Although the method is not rigorously justified, it has been successful in describing qualitative features and trends [31, 29]; however quantitative agreement with experiments has mainly been obtained for strongly coupled system [10, 101, 26].

The chapter begins with some comments on the validity of DFT for transport calculations. In Sec. 4.2 the general setup for electron transport is described in a more technical way and the implications of periodic boundary conditions are discussed. Finally, two different and independent, albeit similar implementations of NEGF-DFT are described and compared.

4.1 DFT for transport

In principle the NEGF formalism presented in chapter 3 provides the exact current through a central region containing interactions. In practice, though, when considering transport through a molecular device an exact determination of the Green's functions entering the current formula (3.2) is not possible. Consequently, we approximate the exact Green's function with the ground state Kohn-Sham single-particle Green's function.

It is generally accepted that although the Kohn-Sham Hamiltonian in principle provides the exact electron density of the ground state, there is no obvious reason to expect that it also yields the true conductance. Indeed there is no rigorous justification for approximating the real single particle states with the Kohn-Sham energies and orbitals from a ground-state DFT calculation. Especially when the molecule is weakly coupled to the leads the misplacement of the resonance peaks resulting from approximations of the exchange-correlation potential is expected to affect the magnitude of the conductance [23, 24, 25].

The true Green's function, G, of the central region can be expressed in terms of the Kohn-Sham Green's function, G_s, through a Dyson equation

$$G = G_s + G_s\tilde{\Sigma}G,$$

where $\tilde{\Sigma}$ is the true irreducible self-energy with the local Hartree and xc-potential subtracted

$$\tilde{\Sigma}(\mathbf{r}, \mathbf{r}', \varepsilon) = \Sigma(\mathbf{r}, \mathbf{r}', \varepsilon) - \delta(\mathbf{r} - \mathbf{r}')v_H(\mathbf{r}) - \delta(\mathbf{r} - \mathbf{r}')v_{xc}(\mathbf{r}).$$

That is, by replacing the real many-body Hamiltonian by the Kohn-Sham Hamiltonian we replace the nonlocal, energy-dependent self-energy by the sum of the local Hartree and exchange-correlation potentials.

We mention that more sophisticated methods for quantum transport based on configuration interaction [102], the *GW* method [103, 104], time-dependent DFT [105], and the Kubo formula [106] have recently been proposed. However, these schemes are considerably more demanding than NEGF-DFT and at present they cannot replace it for practical applications. In the following we shall therefore make the assumption that the electrons can be described as quasi-particles moving in the effective Kohn-Sham potential (see Eq. (2.6)) and therefore replace the full GF by the KS GF.

Besides of this more fundamental question concerning the validity of DFT for describing electron transport, there is a number of numerical approximations involved in the actual implementation. These include, as discussed in Chapter 2, the choice of exchange-correlation functional, pseudopotentials, boundary conditions and basis functions.

4.2 General setup

In this section the general formalism for calculating the conductance of a molecular device using a combination of the non-equilibrium Green's function theory (NEGF) and a ground state density functional theory (DFT) is presented.

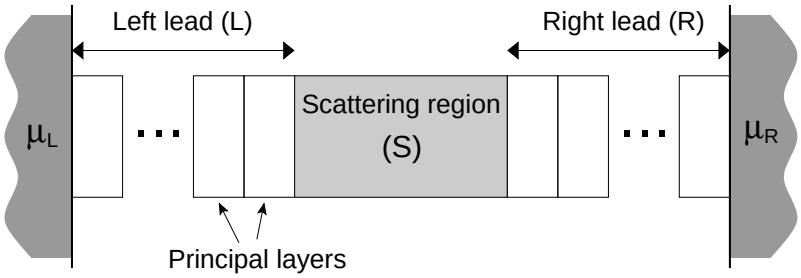

Figure 4.1: Schematic of the system setup used to study electron transport through a central device. Due to the finite support of the basis functions the system can be divided into a central region coupled to a left and right lead. As the lead potential is assumed to be periodic each lead can be build from a principal layer containing an integer number of potential periods. Reproduced from Ref. [19].

The starting point for the NEGF-DFT approach is the formal partitioning of the system into a central region coupled to periodic non-interacting leads (see Fig. 4.1). In a basis, $\{\phi_i\}$, consisting of functions localized in the transport direction (this could be Wannier functions or pseudo atomic orbitals) the electronic Hamiltonian, $\mathbf{H}_{ij} = \langle\phi_i|H|\phi_j\rangle$, and

overlap matrix[1], $\mathbf{S}_{ij} = \langle \phi_i | \phi_j \rangle$, are then partitioned into

$$\mathbf{H} = \begin{pmatrix} \mathbf{H}_L & \mathbf{H}_{CL}^\dagger & 0 \\ \mathbf{H}_{CL} & \mathbf{H}_C & \mathbf{H}_{CR} \\ 0 & \mathbf{H}_{CR}^\dagger & \mathbf{H}_R \end{pmatrix},$$
$$\mathbf{S} = \begin{pmatrix} \mathbf{S}_L & \mathbf{S}_{CL}^\dagger & 0 \\ \mathbf{S}_{CL} & \mathbf{S}_C & \mathbf{S}_{CR} \\ 0 & \mathbf{S}_{CR}^\dagger & \mathbf{S}_R \end{pmatrix},$$

where the zeros reflect that due to the localized nature of the basis functions the direct coupling and overlap between the leads are strictly zero.

The retarded electronic single-particle Green's function of the entire system is defined by $[(\varepsilon + i0^+)\mathbf{S} - \mathbf{H}]\,\mathbf{G}^r(\varepsilon) = \mathbf{I}$. From this it is possible to write its representation in the central region as

$$\mathbf{G}_C^r(\varepsilon) = \left[(\varepsilon + i0^+)\mathbf{S}_C - \mathbf{H}_C - \mathbf{\Sigma}_L^r(\varepsilon) - \mathbf{\Sigma}_R^r(\varepsilon)\right]^{-1}, \tag{4.1}$$
$$\mathbf{\Sigma}_\alpha^r(\varepsilon) = \left[(\varepsilon + i0^+)\mathbf{S}_{C\alpha} - \mathbf{H}_{C\alpha}\right] \mathbf{g}_\alpha^{0,r}(\varepsilon) \left[(\varepsilon + i0^+)\mathbf{S}_{C\alpha}^\dagger - \mathbf{H}_{C\alpha}^\dagger\right], \tag{4.2}$$

where $\mathbf{\Sigma}_\alpha^r$ is the self energy due to the coupling to lead α and $\mathbf{g}_\alpha^{0,r}$ is the retarded Green's function of the uncoupled lead.

4.2.1 Coupling to leads

For obtaining the self-energy due to the coupling to lead α (4.2) one needs the Green's function of the uncoupled lead defined as

$$\mathbf{g}_\alpha^{0,r}(\varepsilon) = \left[(\varepsilon + i0^+)\mathbf{S}_\alpha - \mathbf{H}_\alpha\right]^{-1}.$$

In order to avoid handling infinite matrices we assume that the electrons move ballistically in the leads. As a consequence the electronic potential in the metallic leads will have the periodicity of the underlying bulk crystal. The leads may then be divided into principal layers each containing an integer number of potential periods (see Fig. 4.1). Due to the localization of the basis functions in the transport direction, one can always choose a principal layer size such that only neighboring layers couple. In this case the lead Hamiltonian can be written on a block-tridiagonal form

$$\mathbf{H}_L = \begin{pmatrix} \ddots & \vdots & \vdots & \vdots \\ \dots & \mathbf{h}_0 & \mathbf{h}_1 & 0 \\ \dots & \mathbf{h}_1^\dagger & \mathbf{h}_0 & \mathbf{h}_1 \\ \dots & 0 & \mathbf{h}_1^\dagger & \mathbf{h}_0 \end{pmatrix}$$

where $\mathbf{h}_0$ is the Hamiltonian matrix of a single principal layer and $\mathbf{h}_1$ is the coupling between neighboring layers. This form of the lead Hamiltonian implies that the central region only interacts with the first principle layer. It then follows from Eq. (4.2) that only the Green's function of the first principle layer, the "surface" Green's function, is needed to calculate the lead self-energy. By utilizing the periodic nature of the leads the "surface" Green's function can be calculated using the efficient iterative decimation technique [107].

It is noted that, by enlarging the central region until all perturbations are screened, the assumption of a periodic lead can (in principle) always be fulfilled. In practice the mobile

[1] The overlap matrix is introduced in order to deal with non-orthogonal basis sets.

electrons in the metallic leads screen such perturbations effectively and the mean-field potential converges to its bulk value after a few atomic layers.

When calculating the conductance a reduction in computational costs can be obtained by further subdividing the central region into a left and right layer coupled to a reduced central region. We write the central region Hamiltonian[2] as

$$\mathbf{H}_C = \begin{pmatrix} \mathbf{h}_l & \mathbf{h}_{cl}^\dagger & 0 \\ \mathbf{h}_{cl} & \mathbf{h}_c & \mathbf{h}_{cr} \\ 0 & \mathbf{h}_{cr}^\dagger & \mathbf{h}_r \end{pmatrix},$$

where the hopping between the left and right layer on each side of the reduced central region is set to zero, hereby neglecting direct coupling. The electronic Green's function for the reduced central region can now be written as

$$\mathbf{G}_c^r(\varepsilon) = \left[(\varepsilon + i0^+)\mathbf{s}_c - \mathbf{h}_c - \mathbf{\Sigma}_l'^r(\varepsilon) - \mathbf{\Sigma}_r'^r(\varepsilon)\right]^{-1}, \tag{4.3}$$

where $\mathbf{\Sigma}_\alpha'^r(\varepsilon) = \left[(\varepsilon + i0^+)\mathbf{s}_{c\alpha} - \mathbf{h}_{c\alpha}\right] \mathbf{g}_\alpha'^{0,r}(\varepsilon) \left[(\varepsilon + i0^+)\mathbf{s}_{c\alpha}^\dagger - \mathbf{h}_{c\alpha}^\dagger\right]$ is the self-energy due to the coupling to the new lead α and the "surface" Green's function of the left layer is

$$\mathbf{g}_l'^{0,r}(\varepsilon) = \left[(\varepsilon + i0^+)\mathbf{s}_l - \mathbf{h}_l - \mathbf{\Sigma}_L^r(\varepsilon)\right]^{-1},$$

and similarly for the right layer "surface" Green's function. Starting from some initial "surface" Green's function, this scheme can also be applied iteratively. The obtained simple iterative scheme has the advantage of not being restricted to periodic leads.

4.2.2 Phase-coherent transport

In the case where non-interacting electrons move phase-coherently through a central conductor connected to a left and right lead the conductance is simply given by the Landauer-Büttiker formula

$$G = G_0 \mathrm{Tr}\left[\mathbf{G}_C^r(\varepsilon)\mathbf{\Gamma}_L(\varepsilon)\mathbf{G}_C^a(\varepsilon)\mathbf{\Gamma}_R(\varepsilon)\right].$$

As discussed in Refs. [108] and [21] this formula remains valid for non-orthogonal basis sets provided that the retarded Green's function of the system is defined as the inverse of $[(\varepsilon + i0^+)\mathbf{S} - \mathbf{H}]$.

4.2.3 Inelastic scattering

The starting point for studying electron transport through a central region with electron-phonon interactions is the current formula (3.2). In order to utilize this equation we need the lesser/greater Green's functions (3.3b) evaluated in the presence of coupling to the leads (discussed above) and the phonons. For the electron-phonon self-energy due to mode λ we use the first Born approximation (3.14). Apart from the electronic Green's functions the self-energies also depend on the electron-phonon coupling matrix element, $M_{i,j}^\lambda \propto \sum_I \langle \phi_i(\mathbf{r}) | W_I^\lambda | \phi_j(\mathbf{r}) \rangle$, where the displacement potential, W_λ is the derivative of the effective Kohn-Sham potential in the direction defined by the eigenmode λ. In practice W^λ is obtained as a finite difference between equilibrium Hamiltonians describing the electronic system when the vibrating atoms have been moved in the positive and the negative normal mode direction

$$W_I^\lambda \approx \sum_I \frac{1}{2\delta_I} \left[\mathbf{H}(\delta_I) - \mathbf{H}(-\delta_I)\right]. \tag{4.4}$$

[2]The overlap matrix is written in a similar form.

In this work we evaluate the KS Hamiltonians of the displaced configurations using a fixed basis set. As a consequence terms involving the change in the basis orbitals with displacements are avoided [109]. We notice that, when calculating the displacement potential using DFT the electronic screening effects due to the ionic displacements are included through the effective potential in the self-consistent Kohn-Sham Hamiltonian. As shown by Thygesen [110] the scheme for calculating the current through a region including electron-phonon interactions remains valid in the non-orthogonal case.

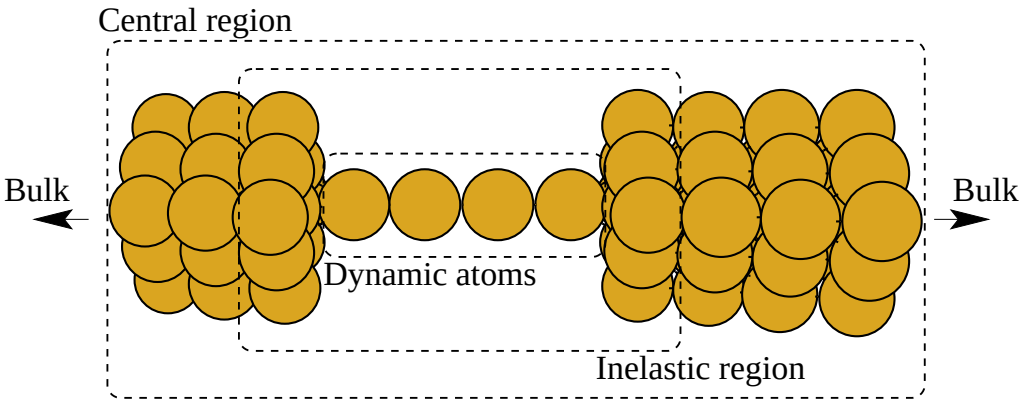

Figure 4.2: Schematic of the generic system setup used for inelastic calculations. The system consists of a central region outside which the potential must be converged to bulk values. To reduce computational costs we introduce an inelastic region which is a reduced central region in which the field generated by the vibrating atoms is taken into account. The dynamical atoms is the relevant subset of the central region atoms, which are allowed to vibrate.

The generic system setup used for inelastic calculations is shown in Fig. 4.2. The current through the inelastic region is calculated using the formalism discussed above together with the Green's functions of the reduced region (4.3).

4.2.4 Periodic boundary conditions

Throughout this work we use density functional theory (DFT) calculations performed with supercells repeated in all directions to construct the system Hamiltonian. Fig. 4.3 shows an example of a central region in the supercell description.

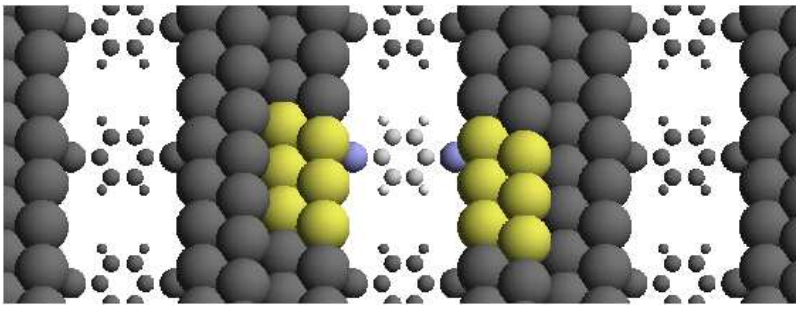

Figure 4.3: The supercell setup used to model a central region consisting of a single molecule placed between metal surfaces. Reproduced from Ref. [19].

To obtain the generic transport setup, the central region should be extended by appropriate semi-infinite leads (illustrated in Fig. 4.4). That is, the mean-field potential at

the left and right end-planes of the supercell must be extended by the lead potential. In practice, the central region Hamiltonian and lead Hamiltonians are constructed from separate supercell calculations. Two different methods for calculating the coupling between the finite central region and infinite leads are discussed in Sec. 4.3. We require, in general, that the electronic potential at the supercell end-planes has converged to the value in the leads. As a consequence the central region C must always contain an appropriate portion of the lead material on both sides of the nano-contact.

As the system remains periodic in the surface plane directions we are in fact considering the conductance of a periodic array of junctions instead of a single junction. It is noted, that whether this provides a good approximation depends on the degree of interference between the repeated junctions. Because of the transverse periodicity we must instead of the localized basis functions $\phi_n(\mathbf{r})$ (these could be Wannier functions or pseudo atomic orbitals) consider the Bloch function

$$\chi_{n\mathbf{k}_\perp} = \frac{1}{\sqrt{N_{R_\perp}}} \sum_{\mathbf{R}_\perp} e^{i\mathbf{k}_\perp \cdot \mathbf{R}_\perp} \phi_n(\mathbf{r} - \mathbf{R}_\perp),$$

where $\mathbf{R}_\perp$ runs over supercells in the surface plane and $\mathbf{k}_\perp$ is a wave-vector in the corresponding two-dimensional Brillouin zone (BZ). Due to the periodicity of the system $\mathbf{k}_\perp$ are good quantum numbers and we can construct the Hamiltonian, $H(\mathbf{k}_\perp)$ and overlap matrix $S(\mathbf{k}_\perp)$ for each $\mathbf{k}_\perp$-point separately. Consequently the conductance *per* junction is given by an integral over the two-dimensional BZ

$$G = \int \frac{d\mathbf{k}_\perp}{A_{BZ}} G(\mathbf{k}_\perp),$$

where A_{BZ} is the area of the first transverse BZ. However, in practice the integral is approximated by a finite sum: $G = \sum_{\mathbf{k}_\perp} w_{\mathbf{k}_\perp} G(\mathbf{k}_\perp)$, where $w_{\mathbf{k}_\perp}$ are symmetry determined weight factors which add up to 1. It is noted that a $N \times N$ Monkhorst-Pack sampling of the surface Brillouin zone corresponds to a Γ-point calculation for a supercell consisting of the original supercell repeated $N \times N$ in the surface plane [3, 60]. The repeated supercell introduces a periodic array of molecules on the surface, which can give rise to interference effects. However, as discussed in Ref. [111] for a supercell containing 3×3 atoms in the surface plane the error introduced by the interference effects are insignificant when compared to the error coming from an insufficient $\mathbf{k}_\perp$-point sampling.

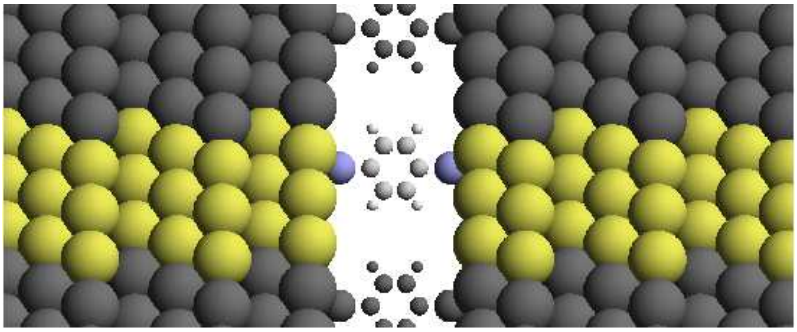

Figure 4.4: The system setup used for calculating the electronic current is obtained by extending the effective potential to the left and right of the supercell by the bulk potential. It is noted that the system remains periodic in the perpendicular directions. Reproduced from Ref. [19].

4.3 Two methods

In this section we present the two different NEGF-DFT implementations used throughout this work. Moreover the advantages and disadvantages of the two methods are compared and discussed.

4.3.1 Method 1: Wannier functions from plane-wave DFT

In this method the Kohn-Sham Hamiltonian is obtained from an accurate plane-wave pseudopotential DFT code [1, 2]. For the plane-wave expansion we use an energy cutoff of 25 Ry and replace the ion cores by ultrasoft pseudopotentials [53]. Exchange-correlation effects are treated with the PW91 functional [49] except in Paper II where the PBE functional [50] is used. Unless stated otherwise a 4×4 Monkhorst-Pack $\mathbf{k}_\perp$-point sampling of the surface BZ were used. For all systems studied this sampling yields conductances converged within a few percentage points.

To obtain a tight-binding like representation of the Hamiltonian we transform the Kohn-Sham eigenstates into partly occupied Wannier functions (WFs) [3] (see Sec. 2.3.2). To ensure that, the accuracy of the plane-wave calculation is carried over to the WF basis for all energies relevant for transport we chose the cut-off energy E_0 in the range of 2-4 eV above the Fermi level. A set of WFs for each region is obtained by performing separate DFT calculations for the (periodic) leads and the central region. As the WFs in the lead will in general differ from those in the outermost lead unit cells of the central region, care must be taken to evaluate the coupling and overlap matrices $H_{C\alpha}$ and $S_{C\alpha}$. Also note that although the WFs by construction are orthogonal within each region, WFs belonging to different regions will in general be non-orthogonal. To ensure a smooth matching at the interface between lead and central region we take the Fermi level of the bulk lead as the common Fermi level of the combined system. This is done by shifting the levels in the central region by a constant, i.e. adding to H_C the matrix δS_c, where $\delta = [H_L]_{0,0} - [H_C]_{0,0}$ and the $(0,0)$ element corresponds to the onsite energy of a basis function located near the interface between L and C. In Ref. [19] a detailed description of the construction of the WFs and the calculations of the Hamiltonian matrix for the combined $L - C - R$ system can be found.

For the inelastic conductance calculations we construct the displacement potential (4.4) by using the WFs of the unperturbed system to obtain the Hamiltonians of the displaced configurations.

The main advantages of the Wannier functions in relation to conductance calculations are:

Accuracy: Below the cut-off energy, E_0, the accuracy of the plane wave calculation carries over to the WF basis set.

Size: The WFs basis set is truly minimal and often results in even fewer basis functions than a single zeta basis.

Localization: The WFs are spatially localized.

Analysis: WFs provide insight into chemical properties and are thus well suited for analysis.

The WFs basis set thus combines high accuracy with high efficiency. The drawbacks of using the WFs basis set are:

Construction: The actual construction of well localized WFs is not always straightforward, and requires some user interaction, particularly for metallic systems. Further, the risk of obtaining different WFs for two similar but non-identical systems renders it less straightforward to patch regions together using Hamiltonians obtained from separate calculations.

Localization: Although the WFs are well localized the rapidly decaying tails do not vanish, i.e. the WFs do not have bounded support. Consequently the WFs must be truncated in order to achieve a decoupling of the leads. In practice this truncation is only expected to be problematic in the low tunneling regime.

Extension: There exists no systematic way of improving the obtained result by expanding the basis set.

4.3.2 Method 2: PAO Siesta basis

In the second method the KS Hamiltonian is obtained from the DFT code Siesta [4] which uses finite range PAOs [62, 5] as basis functions and replaces the ion cores by Troullier-Martins norm-conserving pseudopotentials [54]. We restrict ourselves to the standard PAOs for Siesta: single zeta (SZ), SZ polarized (SZP) and double ZP (DZP). Unless otherwise stated we use 0.01 Ry for the confinement energy, which determines the range of the PAOs, and 200 Ry for the mesh cutoff. Exchange-correlation effects are described with the PBE functional [50] and a $1 \times 4 \times 4$ Monkhorst-Pack grid is used for the **k**-point sampling.

The Hamiltonians of the leads and the central region are obtained from separate calculations. As the KS potential to the left and right of C, by definition has converged to the value in the leads, we can take the coupling between central region and lead α, $H_{C\alpha}$, from the pure lead calculation. This is in contrast to method 1, where the different shape of the WFs in the periodic lead and the lead part of the central region makes it essential to evaluate the coupling matrix directly. Note also that this approximation, i.e. the use of the intra-lead coupling matrix elements ($H_{\alpha\alpha}$) in $H_{C\alpha}$, can be controlled by including a larger portion of the lead in C. In practice we find that 3-4 atomic layers must be included in C on both sides of the junction to ensure converged conductances.

We obtain a fixed basis set for the displacement potential by placing PAOs at the coordinates of the dynamic atoms displaced in both the negative and positive normal mode directions as well as at the equilibrium positions. A drawback of this approach is that, to avoid linear dependence in the basis set the vibrating atoms must be moved quite far away from their equilibrium positions.

Most of the disadvantages of the WF basis are resolved by the PAO basis:

Construction: By definition the PAOs are identical as long as the atomic species on which they are located are the same. This makes it straightforward to patch together Hamiltonians for separate subsystems as long as the KS potential can be smoothly matched at the interfaces.

Localization: The PAOs have finite support.

Extension: It is straightforward to expand the basis set.

The main drawbacks of using the PAO basis for conductance calculations are:

Size: Longer computational times for transport calculations as compared to method 1 is a result of the significantly larger number of basis functions needed to obtain the

accuracy of the WF result.

Extension: There exists no consistent way to extend the basis and thereby converge the result with respect to the basis size.

Chapter 5

Benchmark calculations

First-principles calculations of electrical conductance in nano-scale contacts represents a main challenge in computational nanophysics. The interest for this type of calculations began in the mid-nineties where advances in experimental techniques made it possible to contact individual molecules thereby making it possible to study the transport of electrons through true nano-scale structures [14, 112]. Apart from the scientific interest, the development of reliable simulation tools for nano-scale quantum transport is relevant in relation to the continued miniaturization of conventional semi-conductor electronics, as well as for the introduction of a new generation of molecule based electronics.

As described in chapter 4 it has by become standard to calculate conductance in nano-scale contacts by employing a combination of non-equilibrium Green's function theory (NEGF) and ground state density functional theory (DFT). Irrespective of the validity of the NEGF-DFT approach (see the discussion in Sec. 4.1) and the role played by the approximate functionals, it remains important to establish a general consensus concerning the exact result of a NEGF-DFT calculation for a given xc-functional and specified system geometry: A benchmark. Although this might seem trivial, the present situation is in fact rather unsatisfactory. A variety of different results have been published by different groups for the same or very similar systems. A good example is provided by a benzenedithiolate molecule trapped between gold contacts, where the calculated conductance varies by up to two orders of magnitude for similar geometries [29, 30, 113, 114, 115, 116].

The relatively large variation of the results indicates that the conductance, or more generally the elastic transmission function, is a highly sensitive quantity. Indeed, the implementation of the open boundary conditions defining the scattering problem represents some numerical challenges. Small errors in the description of the coupling between the finite central region and the infinite leads as well as improper **k**-point samplings in supercell approaches, can introduce significant errors in the resulting transmission function.

The chapter is organized as follows: First the main result of the benchmark study is presented. In the study the elastic transmission function of five representative systems is calculated using two independent NEGF-DFT methods. Three of the reference systems, namely Pt-H_2-Pt, Au-BDT-Au and Au-BP-Au, will then be discussed in more details. The two latter junctions contain organic molecules with different anchoring groups (the characteristics of different anchoring groups is the subject of chapter 6). Besides that, the study of the benzenedithiolate system illustrates the effect of the transverse dimensions of the supercell in comparing to cluster based transport calculations. The platinum/hydrogen junction is used to illustrate the importance of a sufficient **k**-point sampling (the system is heavily studied in chapter 7).

This chapter provides a review of Paper IV.

5.1 Reference systems

In this section we compare the transmission function of five representative nano-scale contacts calculated using two different NEGF-DFT implementations (see Sec. 4.3).

The five reference systems chosen for this benchmark study are:

- A monatomic gold chain with a single CO molecule adsorbed.
- A 3-atom Pt chain suspended between Pt electrodes.
- A H_2 molecule bridging two Pt electrodes.
- Benzenedithiolate (BDT) between Au electrodes.
- Bipyridine (BP) between Au electrodes.

The reference systems have been chosen according to the criterion that both experimental data as well as previous NEGF-DFT calculations are available in the literature. Furthermore they are representative in the sense that they cover a broad class of systems; homogeneous and heterogeneous, computationally simple (one-dimensional) and more complex, and strongly as well as weakly coupled.

The main results of the benchmark study is summarized in Fig. 5.1 where we show the overall deviation

$$\Delta = \frac{1}{E_0 - E_1} \int_{\varepsilon_F + E_1}^{\varepsilon_F + E_0} |T_{\mathrm{WF}}(\varepsilon) - T_{\mathrm{PAO}}(\varepsilon)| \mathrm{d}\varepsilon, \tag{5.1}$$

between the transmission functions calculated using the Wannier function (WF) and pseudo atomic orbital (PAO) basis sets, respectively. The energy E_1 is taken as the lowest lying band edge in the lead while the cutoff energy E_0 is taken to be the energy above which the WFs are no longer able to reproduce the exact KS eigenstates of the system which is typically ~ 3 eV above the Fermi level.

For all reference systems the deviation (Δ) decreases as the Siesta basis is enlarged meaning that the Siesta transmission functions converge toward the WF result. This is taken as evidence for the correctness of the WF results and as justification for the use of the term *benchmark* calculation.

In general, we found that the double-zeta polarized (DZP) basis provides very good agreement with the WF basis, whereas the single-zeta polarized (SZP) and, in particular, the single-zeta (SZ) basis can produce substantially incorrect features in the transmission function.

5.2 Pt-H_2-Pt contact

In this section, conductance calculations for one of the simplest possible molecular junctions, namely a single hydrogen molecule between metallic Pt contacts, is presented.

Experimentally, the Pt-H_2-Pt junction shows stable and reproducible behavior in conductance measurements. In particular, a very pronounced peak close to 1 G_0 appears in the conductance histogram obtained when a Pt contact is broken in a hydrogen atmosphere [7]. Although reported conductance calculations show significant variations (see below), substantial evidence has been given that the structure responsible for this peak consists of a single hydrogen molecule bridging the Pt contacts [7, 8]. In chapter 7 the main experimental and theoretical results for this junction are reviewed.

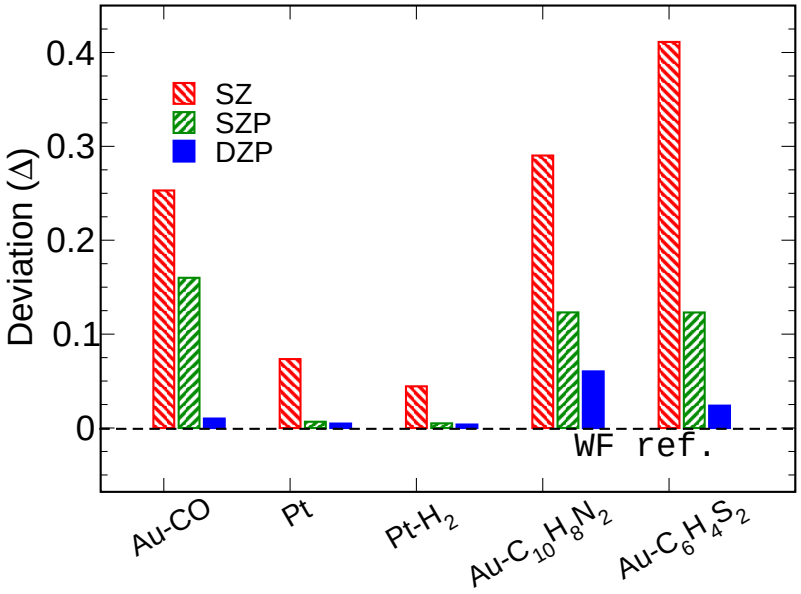

Figure 5.1: Overall deviation between the WF and SIESTA transmission functions for the five reference systems studied. It is noted that in all cases the SIESTA result converge toward the WF result as the PAO basis is enlarged. From Paper II.

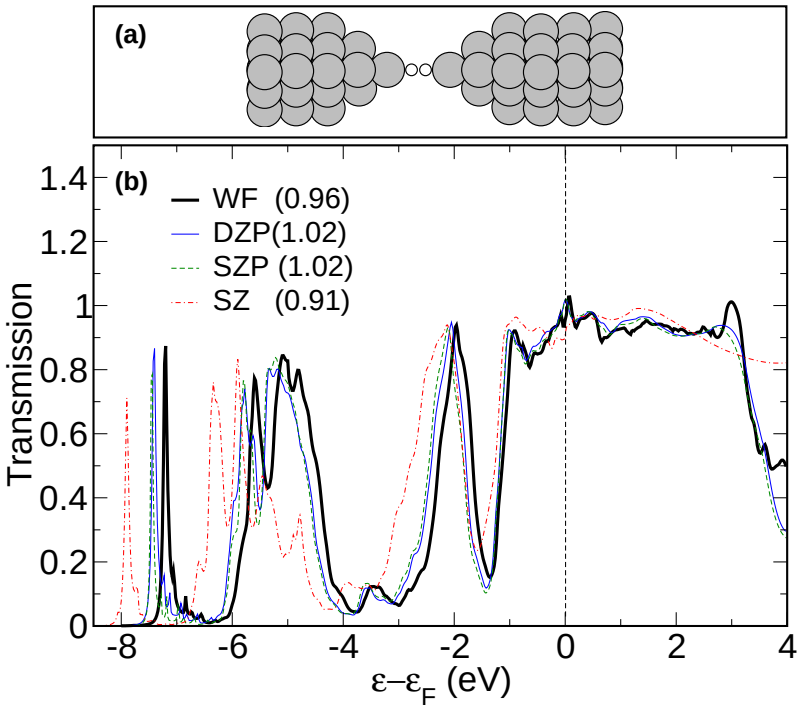

Figure 5.2: (a) Supercell used to model the central region of a Pt-H_2-Pt junction. (b) The transmission function of a hydrogen molecule bridging platinum electrodes calculated using method 1 (WF) and method 2 for three different basis sets. The conductance is indicated in parentheses following the legends. From Paper II.

The supercell geometry of the Pt-H_2-Pt contact is shown in Fig. 5.2(a). The hydrogen molecule is placed in a bridge position between two four-atom pyramids attached to (111)

surfaces containing 3×3 atoms in the surface plane. In order to ensure that the effective KS potential has converged to its bulk value at the end planes of the supercell we include 3-4 atomic layers (ABC-CABC stacking) on either side of the pyramids. To obtain a stable junction structure we relaxed the Pt pyramids and the hydrogen atoms while keeping the rest of the structure fixed in the bulk configuration. We used a lattice constant of 3.93 Å and a distance of 14.60 Å between the two (111) surfaces. With these constraints the relevant bond lengths are $d_{\text{Pt-H}} = 1.7$ Å and $d_{\text{H-H}} = 1.0$ Å.

In Fig. 5.2(b) we show the transmission function calculated using the WF basis set (method 1) and three different PAO basis sets (method 2), respectively. The qualitative agreement between the two methods is striking, especially in the important region around the Fermi level. Quantitatively agreement is however, only provided by the SZP and DZP basis sets. The SZ basis set although reproducing the qualitative features of the larger basis sets also introduces a considerable down shift of the low-lying peaks.

The very good agreement between the two methods indicates that the transmission function for this system is rather insensitive to the basis set. On the other hand, we find that a proper $\mathbf{k}_\perp$-point sampling of the transmission function is crucial to obtain meaningful results independently of the quality of the basis set. If we restrict the calculation to the Γ point a transmission function with a (unphysical) peak at the Fermi level is found (shown in Fig. 5.3 and Ref. [10]). Such unphysical features resulting from an insufficient $\mathbf{k}_\perp$-point sampling are not properties of the molecular junction, but are rather due to van Hove singularities in the quasi one-dimensional leads [111]. From Fig. 5.3 we conclude that the transmission function has converged using 8 irreducible $\mathbf{k}$-points, this conclusion was more generally reached in Ref. [111] for systems containing 3×3 atoms in the surface plane.

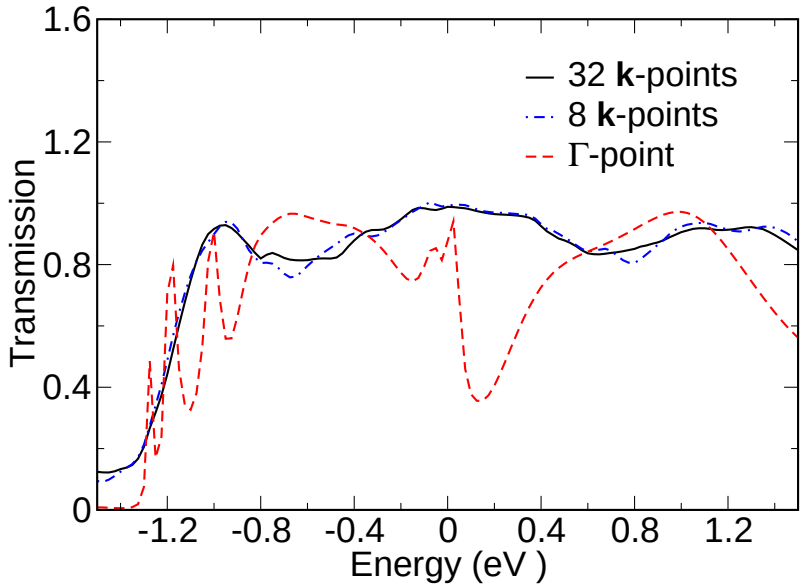

Figure 5.3: The transmission function of the molecular hydrogen contact calculated for three different $\mathbf{k}$-point samplings of the surface BZ. All calculations are performed using method 2 and a SZP basis set. Reproduced from [117].

Several groups have published NEGF-DFT calculations for the transmission function of the Pt-H_2-Pt system. Most find a conductance between 0.9 G_0 and 1.0 G_0 [10, 31, 7, 118]. However, also much lower values between 0.2 G_0 and 0.5 G_0 have also been reported in

Ref. [32].

When comparing the transmission function in Fig. 5.2(b) to the results reported in Ref. [118] which are based on SIESTA DFT code we find very good agreement.

On the contrary the conductance obtained in one of the early theoretical calculations [32] on the hydrogen molecular bridge are considerably lower than what we find. The calculational method applied in Ref. [32] is, however, the same as applied in the study of pure Pt contacts [119] which agrees well with our results (see Sec. IV in Paper II). We speculate if the discrepancy may be related to the smaller size of the Pt cluster used to model the electrodes in Ref. [32] as compared to the one in Ref. [119]. Another possible explanation of the discrepancies is the use of the B3LYP xc-functional in Ref. [32] instead of an LDA/GGA functional used in most other works on Pt-H_2-Pt.

The transmission function reported by Cuevas *et al.* in Ref. [31] has a peak at the Fermi level. We speculate if this is related to the fact that only the Γ point has been used.

5.3 1,4-Benzenedithiolate between gold surfaces

In this section a computational benchmark for the 1,4-Benzenedithiolate (BDT) molecule suspended between gold electrodes is presented.

The Au-BDT system was among the first single-molecule junctions to be studied and has become the standard reference for calculations of nano-scale conductance. Depending on the experimental setup, measured conductances vary between 10^{-4} G_0 and 10^{-1} G_0 [17, 120, 121, 122, 123], while the calculated values typically lie in the range $(0.05-0.4)$ G_0 [23, 124, 29, 115, 30, 113, 116, 125].

In general, it has been found that the transmission function is strongly dependent on the bonding site of the S atom [116, 124], while variations in the Au-S bond length only weakly affects the transmission function [23]. However, as our objective is to establish a computational benchmark for the Au-BDT system, we choose the simple junction geometry shown in Fig. 5.4(a). The S atoms are placed at the minimum energy positions in the fcc hollow sites of the Au(111) surface and the molecule has been relaxed while keeping the Au atoms fixed in the bulk crystal structure. We use a Au lattice constant of 4.18 Å, and a distance between the Au(111) surfaces of 9.68 Å. With these constraints, the relevant bond lengths determining the structure are $d_{\text{Au-S}}$=2.45 Å, $d_{\text{S-C}}$=1.73 Å, and $d_{\text{C-H}}$=1.09 Å.

In Fig. 5.4(b) we show the transmission function calculated using method 1 and method 2 (the SZ result has been omitted for clarity). We notice that the transmission function is only plotted up to 2 eV above the Fermi level. This is because the WF result at larger energies is sensitive to the parameters used in the construction of the basis set, in particular, the cutoff energy. Thus we cannot be sure about the WF result above 2 eV+ε_F. The calculated transmission functions agree very well in the energy range from 2 eV below the Fermi level to 1 eV above the Fermi level, while only the DZP result agrees quantitatively with the WF result in the entire energy range. We notice again the down shift of the PAO transmission functions relative to the WF result.

In general, the presence of a broad transmission peak positioned ~ 1 eV below the Fermi level is in qualitative agreement with previous results [23, 124, 29, 115, 126, 127]. We notice that, for more stretched configurations, i.e. for larger values of the S-C bond length, this broad peak splits into two more narrow peaks [19].

The transmission function presented in Ref. [29] was calculated using a method very similar to our method 2; however, the reported conductance of 0.4 G_0 is almost twice as

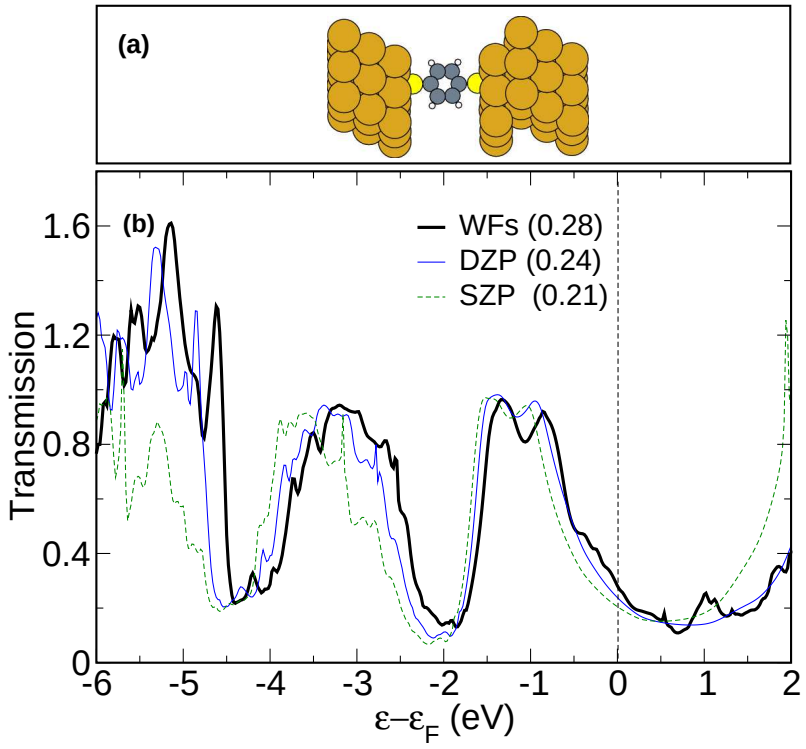

Figure 5.4: (a) Central region used to describe a BDT molecule placed between Au electrodes in the case where the S atoms bind at the fcc hollow sites. (b) The transmission function calculated using method 1 (WF) and method 2 (for clarity the SZ result has been omitted). The conductance is indicated in parentheses following the legends. From Paper II.

high as our DZP results of 0.24 G_0. The large conductance arises because the transmission peak closest to the Fermi level is considerably broader than what we find. If, however, we restrict the calculation to the Γ-point we find the same broadening as in Ref. [29] and a very similar conductance of 0.37 G_0. Another feature of the transmission function in Ref. [29] which is reproduced by a Γ-point calculation is the fact that the second peak positioned at ~ 3 eV below the Fermi level separates into a number of more narrow peaks.

In Ref. [115] the transmission function is calculated using the linear muffin-tin orbitals-atomic sphere approximation (LMTO-ASA) method and averaged over 36 irreducible $\mathbf{k}_\perp$-points. Both the width and the position of the two peaks in the transmission function at 1 eV and 3 eV below the Fermi level, are in good agreement with our results. The height of the former peak is, however, lower than in our calculation and this reduces the conductance to a value of 0.07 G_0. We suspect that this difference could be due to differences in the adopted contact geometries.

When comparing transmission functions calculated using a supercell approach to a cluster based calculation (as the one in Ref. [23]) it is essential that both calculations have been converged. That is

(i) for the supercell calculation the number of $\mathbf{k}_\perp$-points and the supercell size must be converged, and

(i) for the cluster based calculation the cluster size must be converged.

To prove that our supercell calculations are converged and thereby directly comparable to fully converged single molecule cluster calculations we investigate the effect of enlarging

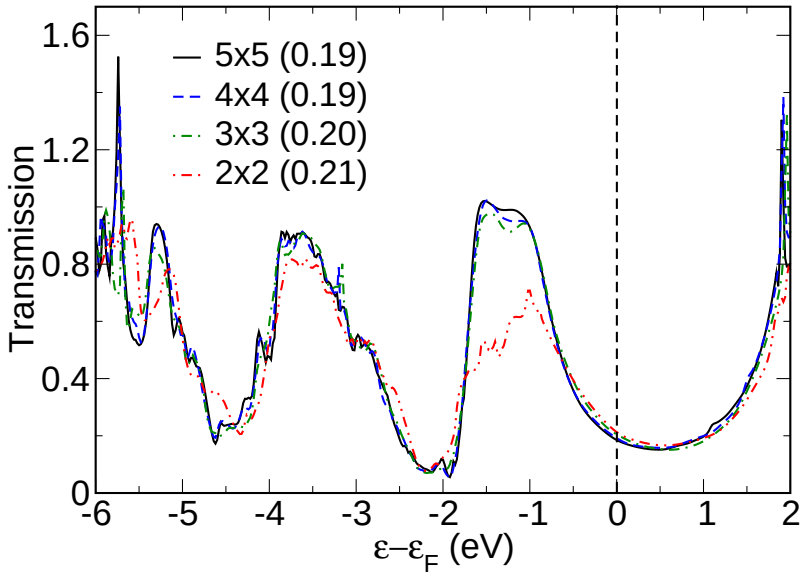

Figure 5.5: The calculated transmission function for the Au-BDT system, where the number of surface atoms is varied from 2×2 atoms to 5×5 atoms, as indicated in the legends. All calculations apply the SZP basis and have been converged with respect to the number of $\mathbf{k}_\perp$-points. The conductance is indicated in the parentheses. From Paper II.

the supercell size (see Fig. 5.5). Extrapolating our converged calculations for 3×3 atoms within the surface plane of the supercell and 4×4 $\mathbf{k}_\perp$-point to a Γ-point calculation gives a supercell consisting of ~ 1000 atoms. We speculate that clusters of similar sizes are needed to reach the same level of convergence. Interference effects between the periodic array of junctions could, however, blur the comparison to single molecule cluster calculations. To quantify the inter-molecular interference effects, we show in Fig. 5.5 the SZP transmission function for the Au(111)-BDT-Au(111) system, where the number of Au atoms in the surface plane is varied from 2×2 atoms to 5×5 atoms. Each calculation has been converged with respect to the number of $\mathbf{k}_\perp$-points by a 4×4 Monkhorst-Pack sampling for all the supercells, except the smallest supercell for which 8×8 $\mathbf{k}_\perp$-points was needed. From Fig. 5.5 it is evident that the transmission function is well converged with 3×3 atoms in the surface plane.

5.4 4,4-Bipyridine between gold surfaces

In this section, we consider a 4,4-Bipyridine (BP) molecule placed between two gold-electrodes.

STM experiments on BP molecules in a toluene solution [15] show a quantization of the conductance in multiples of 0.01 G_0. This quantization effect was interpreted as the formation of certain stable contacts containing one or more BP molecules.

Although the conductance through a BP molecule is expected to be sensitive to the details of the Au-contact geometry [128], the junction structure of molecules linked by nitrogen atoms via their lone electron pairs is, in general, found to be more well-defined than thiol linked molecules [6, 129]. For the benchmark calculation we use a flat Au(111) surface with bipyridine binding at an on-top site which is the minimum energy configuration, as shown in Fig. 5.6(a). To obtain a stable junction we relax the molecule while keeping the Au atoms fixed in the bulk crystal structure. We use a Au lattice constant

of 4.18 Å, a distance between the Au surfaces of 11.53 Å and the Au(111)-N distance is 2.18 Å.

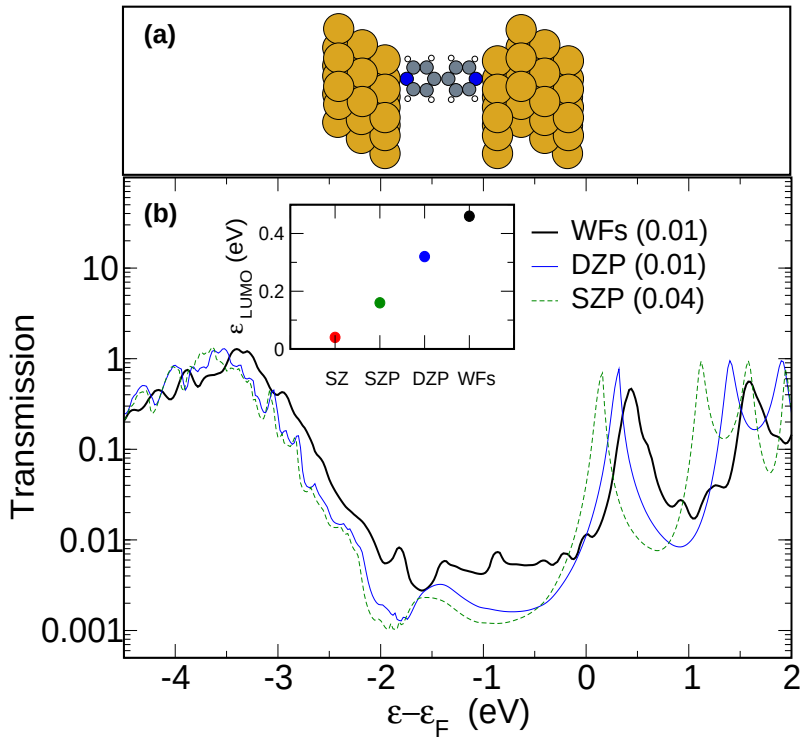

Figure 5.6: (a) Supercell used to model the central region of the Au-BP-Au junction. (b) Calculated transmission functions (the SZ result has been omitted for clarity). In the inset we show the dependence of the LUMO position on the basis sets. The conductance is indicated in the parentheses following the legends. From Paper II.

The transmission functions calculated using either PAOs (SZ has been omitted for clarity) or WFs are shown in Fig. 5.6(b). Notice that, to make the differences in the low transmision regime more visible we have used a logarithmic scale. Overall, the structures of the different transmission functions are similar. As the narrow LUMO peak is close to the Fermi level small changes in the position of this peak is expected to change the conductance considerably [130]. In the inset of Fig. 5.6(b) we show the position of the LUMO peak for the different basis sets. It is observed that ϵ_{LUMO} is underestimated for the PAO basis sets but converges towards the WF result as the basis set is enlarged from SZ to DZP. In spite of the fact, that the position of the LUMO peak differs for the DZP basis and WF basis set the conductance is unchanged. This result is due to the different tails observed in the high barrier tunneling regime of the transmission function for the PAO and WF basis sets. The origin of this can be two-fold: (i) The density of states of the Au-surface, which influence the DOS of the LUMO, could be different in the two cases. (ii) The truncation of the WFs could introduce artificial features in the transmission function in the low tunneling regime.

Several groups have investigated the transport properties of bipyridine-gold junctions, and in general it has been found that the low bias conductance depends on the details of the contact geometry [128, 131, 132]. As different groups have chosen different geometries and models for the gold electrodes a direct comparison of the reported transmission functions is difficult.

Calculations by Wu *et al.* [132, 133] obtained using a SIESTA-based transport code [20], for bipyridine attached to the on-top site of a gold surface show overall good agreement with our results (see Fig. 7(a) in paper [132]). The minor differences are probably related to the fact that only the Γ-point has been used.

To the best of our knowledge, the first theoretical paper on the Au-BP-Au system is by Tada *et al.* [134]. In their calculations, bipyridine is adsorbed on-top of an Au-atom in a rather small Au cluster. The coupling to the infinite electrodes is then modeled by a broadening parameter fitted to experimental data. The zero-voltage transmission function contains some of the same peak structures as we observe.

Hou *et al.* [131, 135, 136] have published several papers on the gold-bipyridine junction. Like Tada *et al.* they include only a few gold atoms in the *ab-initio* calculation and treat the coupling to electrodes through a model self-energy term. The peak structure of the transmission function is quite different from ours. And while most other groups observe tunneling through the LUMO tail [128, 130, 137], Hou *et al.* argue that the transport is mainly taking place via the HOMO-2 state. We speculate if, the differences could be due to the small size of the gold clusters used to mimick the electrodes.

5.5 Summary

A set of benchmark calculations for the Kohn-Sham(PBE) elastic transmission function was established. We studied five representative single-molecule junctions using two different methods based on independent DFT codes: (i) A plane wave DFT code in combination with maximally localized Wannier functions. (ii) The SIESTA program which applies finite range pseudoatomic orbitals.

For all five systems it was found that the SIESTA result converges towards the WF result as the SIESTA basis is enlarged from SZ to DZP with the latter yielding very good quantitative agreement with the WF transmission. In the SIESTA calculations the transmission peaks relative to the peaks obtained with the plane-wave calculation are systematically shifted toward lower energies. The problem can be overcome by enlarging the SIESTA basis, however, the convergence can be rather slow.

Chapter 6

Characterization of anchoring groups

A detailed, quantitative understanding of the electron transport properties of molecular junctions composed of a single molecule between two metallic electrodes is an essential step for the development of molecular electronics. Experiments on single-molecule junctions often suffer from a large variability in the measured conductance, probably originating from details beyond experimental control such as the atomistic details of the local contact geometry. In the case of molecules linked to metal electrodes via a sulphur atom, that is, through thiol linking groups, the conductance shows strong junction to junction variation within the same experiment [138], as well as between different sets of experiments [17, 120, 121, 123]. On the other hand, more recent experimental and theoretical work suggest that the use of amine (NH_2) anchoring groups yields junctions with a more well defined conductance [6]. These findings indicate that the electrical properties of a single organic molecule captured between metallic electrodes are, at least partly, determined by the anchoring group.

In this chapter, we identify and compare the intrinsic properties of two commonly used anchoring groups, namely the thiol and amine groups, by performing DFT calculations for both structure and conductance of different Au-S-Au and Au-NH_2-Au nano-junctions. In the case of sulphur we consider two different geometries: a top-top configuration where the sulphur atom is bonded to a single gold atom on each side, and a top-hollow configuration where sulphur is bonded to a single gold atom on one side and three gold atoms on the other side. We simulate a break junction experiment by calculating the conductance as the contact is pulled apart, and we find a strong dependence on the local atomic structure. In contrast to sulphur, we find that the amine group always binds to a single Au atom on each side of the junction. We consider two junction geometries: a symmetric top-top configuration similar to the one found for S, and an asymmetric top-top configuration. The pronounced structural selectivity of the amine group leads to very similar conductance traces for the two configurations.

This chapter is a review of Paper IV.

6.1 Sulfur and amine in gold junctions

In this section we compare the transport properties of the thiol and amine anchoring groups.

We concentrate on two different structures for the gold contacts:

(i) Two opposing pyramids,

(ii) A pyramid opposing a pyramid with the tip atom removed,

with geometries as shown schematically in Figs. 6.1 and 6.3. In the supercell description the sulfur atom or amine group sandwiched between two four-atom Au-pyramids are attached to Au(111) surfaces. In order to ensure that the KS potential has converged to bulk values six Au atom layers each containing 3×3 atoms in the surface plane are included. To obtain stable junction structures we use DACAPO [1, 2] to relax the position of the anchoring group and the pyramids keeping the rest of the Au atoms fixed in the bulk positions. When increasing the electrode distance, all atomic distances between them have been proportionally increased and subsequently relaxed. The transmission functions are calculated using method 1 described in Sec. 4.3.1.

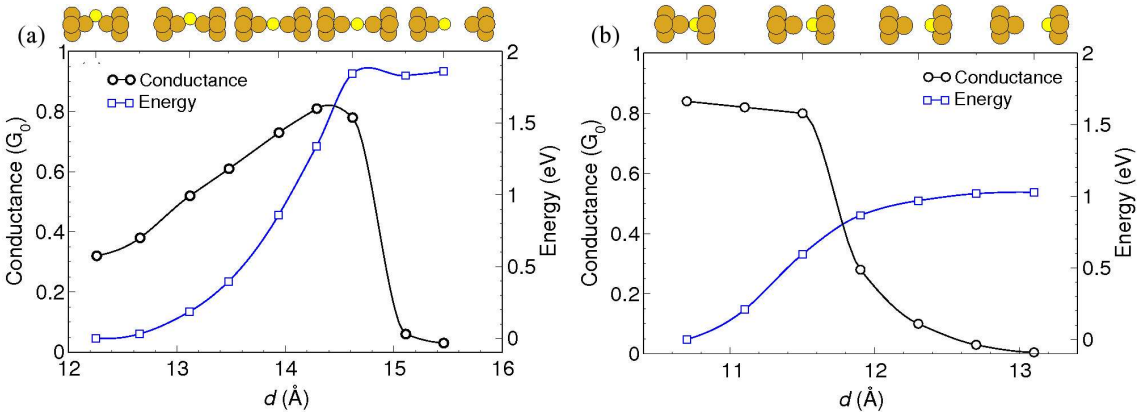

Figure 6.1: Conductance (circles) and total energy (squares) for Au-S-Au nano-junctions in (a) the symmetric top-top and (b) the top-hollow configuration as a function of distance between the outermost Au(111)-surfaces. For the top-top configuration the conductance increases as the contact is pulled apart due to the linearization of the contact geometry. The breaking forces are approximately 1.8 and 1.0 eV/Å, respectively. The zero points of the energy have been chosen arbitrarily. From Paper IV.

To gain insight into the possible structures of an Au-S/NH_2-Au contact, we have made successive relaxations of the system as the distances between the outermost surface layers is varied, thereby simulating the contact formation in a break junction experiment. For gold contact (i) both S and NH_2 bind symmetrically to the tip atoms of the two pyramids. These structures are referred to as (symmetric) top-top configurations. For gold contact (ii), S adopts the site of the removed Au tip atom, thus forming a top-hollow configuration. However, NH_2 forms a bridge between the pyramid tip atom and one of the three gold atoms forming the pyramid base (the asymmetric top-top configuration). It is noted that the sulphur top-top and top-hollow configurations correspond to the configurations proposed in [139]. Moreover molecular dynamics simulations of sulphur-contaminated gold contacts frequently result in Au-S-Au contacts similar to the ones studied here [140].

We start by considering the sulphur top-top configuration, shown in Fig. 6.1(a). For short distances between the Au(111)-surfaces, the S atom is situated at the side of the contact bridging the two Au tip atoms. As the contact is pulled apart, the sulphur atom moves into the contact resulting in a linear contact configuration. Interestingly, the conductance increases from 0.3 G_0 to 0.8 G_0 as the contact is pulled apart, demonstrating how small changes in the local atomic structure of the contact can lead to significant changes in the conductance of the junction. In general, such behavior is characteristic of

the phase-coherent transport regime and is a direct manifestation of the wave nature of the charge carriers.

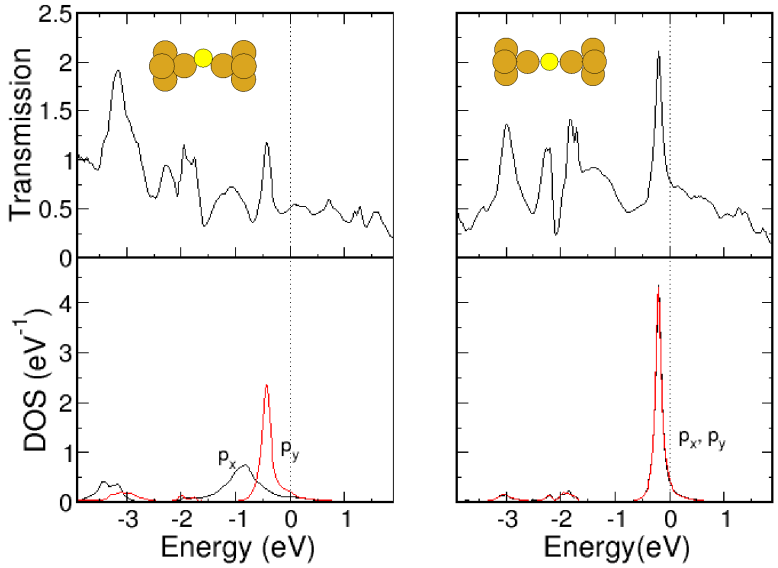

Figure 6.2: Total transmission (upper panels) and projected density of states (PDOS) for the p-orbitals perpendicular to the contact axis (lower panels) for a contracted (left) and stretched (right) Au-S-Au contact. The center of both the p-orbitals moves closer to the Fermi level as the contact is elongated. The p_x-orbital (pointing towards the sulphur atom) is completely quenched for the contracted contact due to the coupling to the gold s-band. Both effects result in the observed increase in the conductance as the contact is stretched. From Paper IV.

The observed increase in conductance as the contact is stretched is mainly due to the gradual opening of a new eigenchannel originating from the sulphur p_x orbital (the x-axis is vertical on all plots of the structure). To illustrate this effect, we compare in Fig. 6.2 the transmission function and the projected density of states (PDOS) for the p_x and p_y orbitals at two different elongations of the contact. The peak in the transmission function just below the Fermi level is clearly correlated to the PDOS of the p_x and p_y orbitals. For the contracted configuration the PDOS of p_x is broadened and shifted downwards by the coupling to the gold s-band which effectively closes the p_x channel. In the linear configuration, this coupling is prohibited by symmetry and p_x and p_y are degenerate. Consequently, the peak in the transmission function grows in intensity and is shifted closer to ε_F as the contact is stretched. Besides the contribution from the p_x- and p_y-orbitals, the total transmission also includes a background contribution from the p_z-orbital pointing in the transport direction. However, this background contribution stays almost constant when the system is elongated. In more general terms, we conclude that a sharp peaks in the transmission function very close to ε_F makes the conductance sensitive to changes in the surrounding potential.

In the Au-S-Au top-hollow configuration, the sulphur atom occupies the site of the removed tip atom of one of the two pyramids (illustrated in the schematics of Fig. 6.1(b)). When the junction is pulled, no major rearrangements of the atoms occur and the conductance stays rather constant around 0.8 G_0 until the contact breaks. The conductance trace of the top-hollow configuration is seen to be distinctly different from the trace of the top-top configuration in Fig. 6.1(a). In particular, the conductance does not increase

upon pulling but stays almost constant until the breaking point.

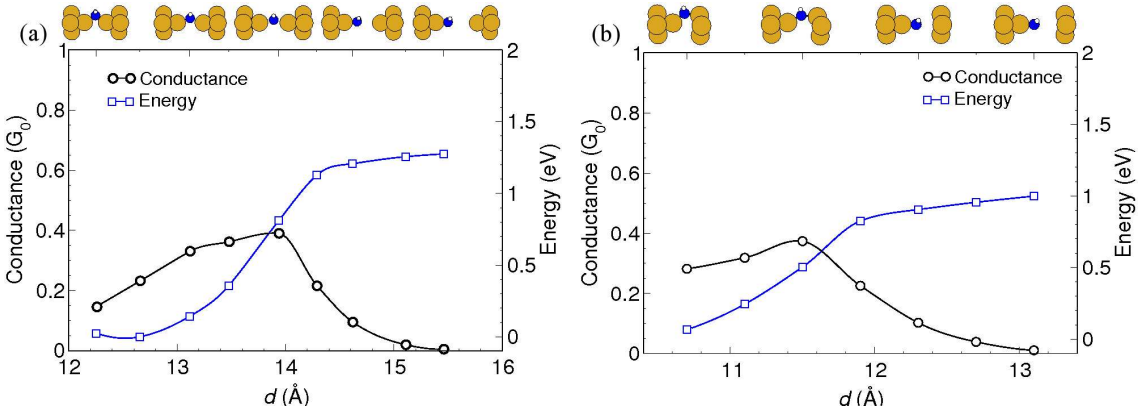

Figure 6.3: Conductance (circles) and total energy (squares) for Au-NH_2-Au nanojunctions in (a) the symmetric top-top and (b) the asymmetric top-top configurations as a function of distance between the outermost Au(111)-surfaces. It is noted that, the amine group is found to be structural selective and always bind to a single Au atom on each side of the junction. The breaking forces are approximately 1.0 and 0.9 eV/Å, respectively. From Paper IV.

Next, we consider the symmetric NH_2 top-top configuration shown in Fig. 6.3(a). The structural change upon pulling is rather similar to the changes observed for the symmetric sulphur junction. However, the conductance is somewhat lower and increases from about 0.2 G_0 to 0.4 G_0. It is observed that the drop in conductance when the contact breaks is less abrupt than for the sulphur junction. This is a consequence of the weakness of the Au-NH_2 bond as compared to the Au-S bond, which implies that the gold pyramids retract less when the NH_2 junction breaks. More generally, the continuous drop in conductance upon rupture is an artifact of the finite size of the supercell which prohibits a large retraction of the contact when it breaks.

The transmission functions of the NH_2 junction for two different elongations are shown in Fig. 6.4. In comparison with the sulphur junction, the transmission functions of the amine junction show only little variation around ε_F. Thus small changes in the nearby electron potential due to changes in the gold contacts should only have little effect on the conductance.

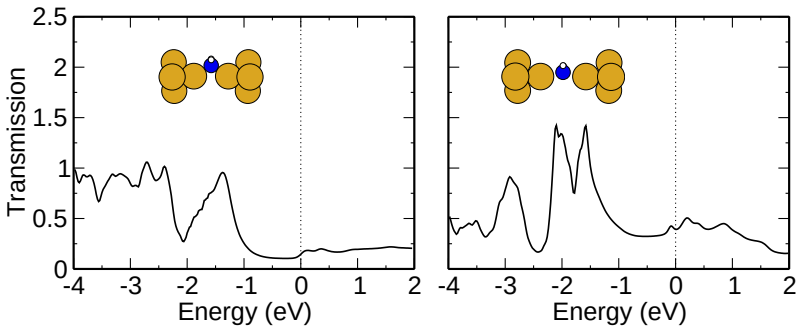

Figure 6.4: Total transmission for a contracted (left) and stretched (right) Au-NH_2-Au contact. Notice that the transmission function varies little around the Fermi level as compared to the transmission function of the Au-S-Au contact shown in Fig. 6.2. From Paper IV.

The calculated conductance trace of the asymmetric NH_2 top-top configuration (the same Au contact geometry as for the sulphur top-hollow) is shown in Fig. 6.3(b). The conductance increases from 0.3 G_0 to 0.4 G_0 as the junction is pulled and is quite similar to the symmetric NH_2 top-top configuration. The reason for the similarity with the symmetric top-top configuration is that in both cases NH_2 binds to a single gold atom on each side of the contact. This structural selectivity is due to the fact that the hydrogen atoms occupy two of the four available sp^3 hybrid sites, which leaves only two unoccupied orbitals for the gold bonds. Obviously this is in contrast to sulphur, which can form bonds to four gold atoms as in the top-hollow configuration of Fig. 6.1(b).

6.2 Summary

The main result of this study is that the structural selectivity of the amine group leads to small junction to junction fluctuations in the conductance traces of the Au-NH_2-Au junctions, whereas the larger variability in sulphur-gold bonding geometries leads to significantly different Au-S-Au conductance traces depending on the atomic structure of the gold contacts. We notice that this trend is further enhanced by the angular flexibility of the preferred binding site of the amine group [141] and the fact that the strong Au-S bond can complicate the junction structure. Overall we find that, the intrinsic transport properties of the amine group are more well defined than those of the thiol. This supports the experimental finding that amine bonded molecules are easier to characterize in terms of conductivity than thiol bonded molecules.

We expect that, the similarity of the conductance traces of the Au-NH_2-Au junctions will lead to a peak around $0.4G_0$ in an experimental conductance histogram. On the other hand, the structural sensitivity of Au-S-Au junctions may produce a histogram without clear features. However, it should be possible to identify the sulphur top-top structure from its characteristically rising conductance trace.

Chapter 7

Hydrogen in metal junctions

In recent years it has become possible to measure the electrical properties of single molecules captured between metallic electrodes [142, 143, 7]. Such experiments provide a unique opportunity to develop our understanding of basic quantum mechanical phenomena at the nanometer length scale. At the same time the single-molecule contacts constitute the first steps towards molecular-based electronics [144], where a small functional molecule represents the ultimate miniaturization of a transistor [13] and metallic mono-atomic wires are the corresponding smallest possible electronic device interconnects.

As experiments on single-molecule junctions are quite involved and depend on many factors they must be supplemented by theoretical calculations. Compared with experimental data, such as peaks in the conductance histogram and vibrational excitation energies, these calculations provide insight into the atomic structure of the molecular junction. Especially the interactions between the conduction electrons and the molecule's vibrational degrees of freedom can be used to characterize the atomic structure of molecular junctions by exploiting the sensitiveness of the molecule's vibrational frequencies and the electron-phonon interaction on the junction geometry [145, 8, 27, 72, 146].

Experiments on molecular junctions are far from trivial. One of the main problems arises from the difficulty in establishing a stable and reproducible contact to the metallic electrodes. Perhaps the simplest molecular junction consists of a single hydrogen molecule sandwiched between Pt electrodes. In view of the difficulties encountered for contacts containing larger molecules (see the discussions in chapter 5 and 6) this junction seems to provide a natural starting point for the study of electron transport in single molecules.

In the first experiments contacting hydrogen molecules by platinum leads it was found that the presence of hydrogen changed the conductance from 1.5 G_0 to 1.0 G_0 [7, 8, 9]. The system was characterized in details by using point contact spectroscopy and shot noise measurements. A close agreement between the experimental data and an atomistic model calculation was obtained when the structure giving rise to the 1 G_0 peak was identified as the linear bridge configuration [10, 8, 118]. In spite of the apparent simplicity of this contact structure it is highly unexpected from a chemical point of view that the linear bridge configuration is stable. This is because Pt is well known as an excellent catalyst for hydrogen dissociation. Besides the main peak at 1 G_0 there is more structure in the conductance histogram for the Pt/H_2 system. In particular, a strong peak is found at about 0.1-0.2 G_0. More recently these low conductance features were attributed to the formation of a hydrogen decorated Pt atomic chain that forms one of the leads contacting the hydrogen molecule (see Paper I). After the first Pt/H_2 experiment also other metal wires (e.g. Au [147, 148], Pd [149], Al in the superconducting state [150]) have been broken in a hydrogen environment.

This chapter starts with a short overview of the main experimental and theoretical results for the Pt/H_2 system. Among other we present a possible formation path that may lead to the linear bridge configuration (the result on the dissociation barrier is unpublished). The material presented on the low conductance features is a summary of Paper I. In Sec. 7.2 we discuss the Au/H_2 system. In particular, we compare the transport properties of a H_2 molecule bridging Au and Pt electrodes, respectively. It is found that the differences in the transmission function to a large extend can be explained by the change in d-band position and work function when going from Au to Pt. Finally, we present DFT calculations for the dI/dV curves of Pt/H_2 and Au/H_2 junction in the presence of electron-phonon interactions (the results are summarized in Paper V).

7.1 The platinum/hydrogen junction

In this section we review the main experimental and theoretical results for the Pt/H_2 system.

The measurements on the Pt/H_2 contact were performed using the mechanically controlled break-junction (MCBJ) technique. In Fig 7.1 the working principle of the MCBJ, which were introduced by Moreland and Ekin [151] and further developed by Muller *et al.* [152], is sketched.

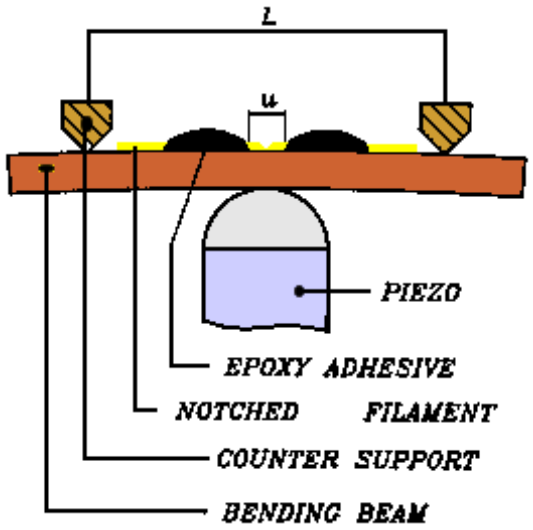

Figure 7.1: A notched sample metal wire is glued on to a flexible substrate. By using a piezo element to bend the substrate the wire will be stretched and eventually broken. When afterwards releasing the bending strain, contact between the clean fractured surfaces is regained. Reproduced from Ref. [152].

Initially a notched Pt wire is glued onto an insulating elastic substrate (the bending beam). The substrate is then mounted in a three-point bending configuration between the top of a piezo element and two fixed counter supports. The whole setup is placed in a vacuum chamber and cooled to 4.2 K. By moving the piezo element forward the substrate will bend causing the Pt wire to be stretched with subatomic precision until it eventually breaks. A new atomic-sized contact can now be formed by relaxing the substrate, thereby bringing the clean fracture surfaces back into contact.

A conductance trace, like the ones in Fig. 7.2(a,b), is obtained by measuring the conductance at a fixed time rate during a contact breaking and remaking cycle. The plateaus in the conductance traces corresponds to elastic deformation of particular stable atomic structures. While the abrupt jumps in between are caused by atomic reconfigurations inside the contact in response to the applied stress. As these deformations and reconfigurations will depend on the detailed atomic structure of the contact, which even in the last stage before rupture involves a large number of atoms, the form of the individual conductance traces are nearly impossible to predict beforehand. In contrast, common features shared by many independently prepared contacts can be revealed by analyzing conductance histograms produced from a large number of traces.

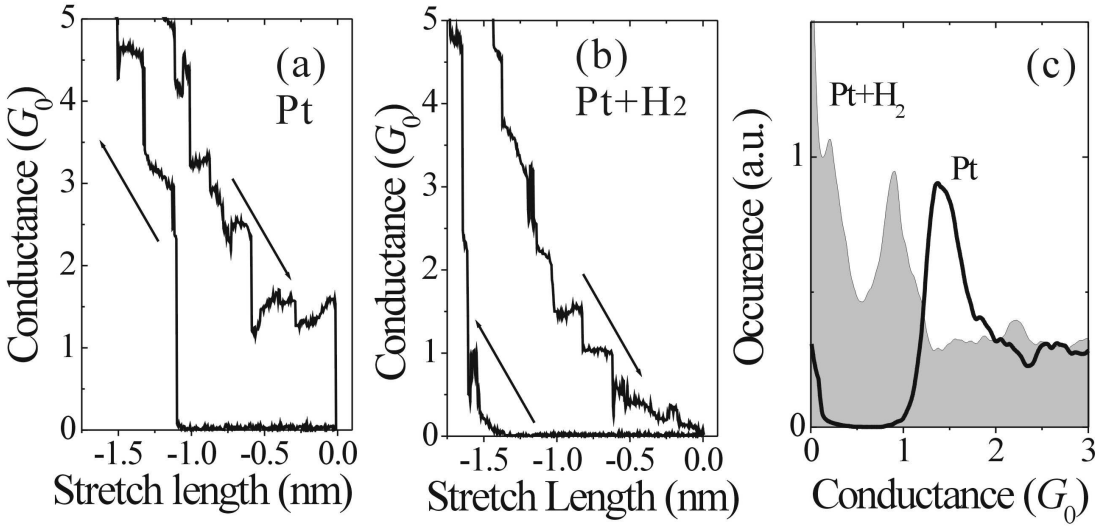

Figure 7.2: Conductance traces for clean Pt (a) and for Pt when H_2 has been admitted (b). Conductance histograms for clean Pt (black curve) and Pt in a H_2 atmosphere (grey area) is shown in (c). From Paper I.

The black curve in Fig. 7.2(c) is a conductance histogram for a clean Pt wire The large peak around 1.5 G_0 indicates that just before rupture a clean Pt contact with a conductance around 1.5 G_0 are frequently formed. NEGF-DFT calculations have shown that (zig-zag) monatomic Pt chains indeed have conductances close to this value [101, 26, 153].

When admitting a small amount of hydrogen gas into the chamber the average breaking and remaking cycle, and thereby the conductance histogram, is drastically changed [7, 154]. The main peak at 1.5 G_0 disappears and instead two strong peaks, one at 1 G_0 and the other near 0.2 G_0 on top of a low-conductance tail, is observed (see Fig. 7.2(c)). Looking at the individual traces the conductance in most cases decreases stepwise after the appearance of a plateau around 1 G_0. A sudden conductance drop into the tunneling regime from 1 G_0 is a rare event. This suggests that at the last stages of stretching there is a strong tendency towards the formation of first a certain stable contact structure with a conductance near 1 G_0. And second by further stretching the formation of new structures with lower conductance.

In the following sections the origin of these two peaks will be discussed separately.

7.1.1 The plateau near 1 G_0

In this section, a summary of the main experimental and theoretical findings for the histogram peak close to 1 G_0 is presented. The overall conclusion is that the most probable atomic structure responsible of this peak consists of a single hydrogen molecule bridging the platinum electrodes.

Conductance channels

In general (as described in Sec. 3.2) the phase-coherent conductance can be written as $G = G_0 \sum_n \mathcal{T}_n$, where $\mathcal{T}_n$ is the eigenvalues of the transmission matrix. Experimentally information about the number of channels and individual eigenchannel transmissions can be obtained by various methods. These include measurements of the reproducible conductance fluctuations as a function of bias voltage [155, 156], shot noise measurements [157, 158] and analysis of the superconducting subgap structure [159, 14]. In the following we focus on the two former methods as both have been used to extract information about the channel content of the platinum/hydrogen junction.

The conductance fluctuations originate from interference patterns in the electron wave functions due to the repeated scattering of the contact and defects nearby. As the applied bias is varied the wave length of the electron will change producing random variations in the interference and thereby making the conductance fluctuate. When all $\mathcal{T}_n$ is either 0 or 1 the reflection at the contact vanishes and thus the fluctuations will be suppressed.

In their original paper on the Pt-H_2-Pt junction Smit *et al.* reported that, for structures with a conductance around 1 G_0 the conductance fluctuation amplitude is suppressed [7]. This indicates that the atomic junction is characterized predominantly by a single almost fully open channel.

Due to the discreteness of the electronic charge, the current through any system is observed to fluctuate around the average value. For single molecular junctions these fluctuations originates from the quantum mechanical probability for the electron to be either transmitted or reflected. As the Fano factor depends on the sum $\sum_n \mathcal{T}_n(1-\mathcal{T}_n)/\sum_n \mathcal{T}_n$ information about the number of conducting channels and their transmission can be obtained by measuring the shot noise [14].

Later shot-noise measurements on the platinum/hydrogen system confirmed that the electron transport through structures at the 1 G_0 plateau is carried predominantly by a single, nearly open channel with only very small contributions from additional channels [9].

Point contact spectroscopy

In order to further characterize the atomic structure of the molecular contact giving rise to the 1 G_0 peak, the local vibrations were probed by point contact spectroscopy (PCS) [7, 8]. In PCS [14] the differential conductance is measured as a function of the bias voltages applied across the junction. At the point where eV exceeds the energy of a vibrational mode ($\hbar\omega$) an inelastic scattering event involving the emission of a phonon may take place. If the junction has a single fully transmitting channel the electrons can only be backscattered and a drop in the dI/dV curves at voltages corresponding to $\hbar\omega$ is observed (see Sec. 3.3.3). In the general case, the sign of the conductance correction depends on the transmission and reflection coefficients of the involved channels (3.20). We notice that, in some measurements peaks rather than steps are observed in the differential

conductance curve, in this case the analysis outlined in Ref. [160] can be used to identify the characteristic frequencies.

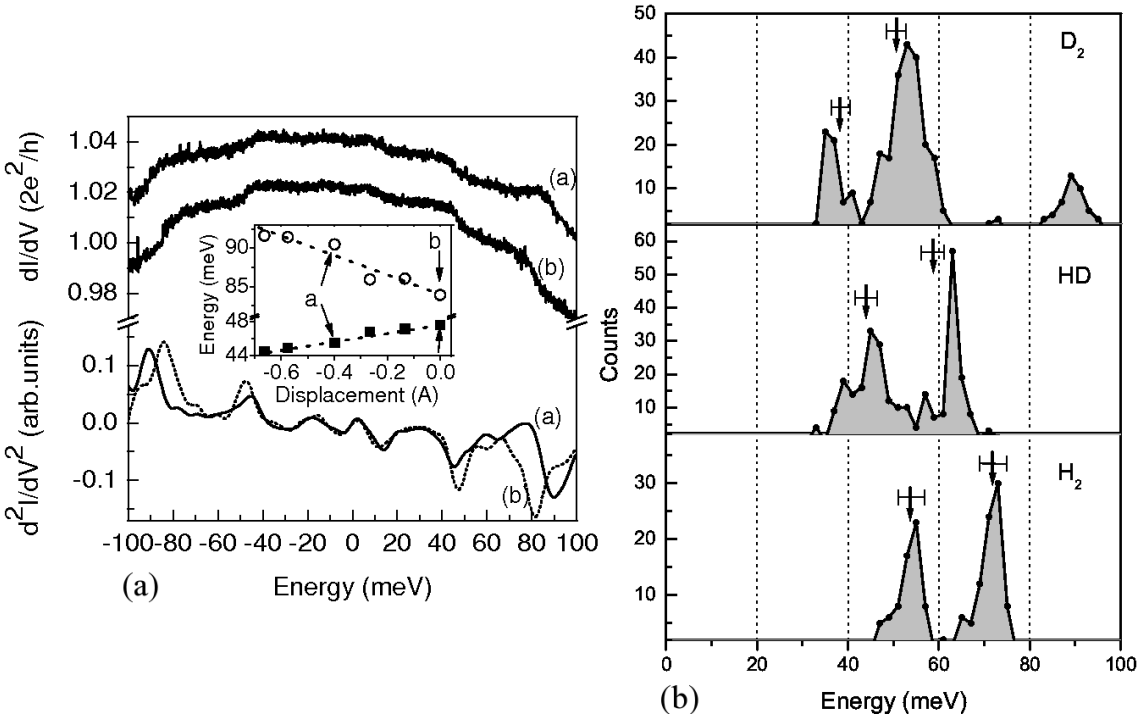

Figure 7.3: (a) dI/dV curves (top) and their numerical derivatives (bottom) for a Pt-D_2-Pt contact at two different stretching length. The complete evolution of the frequencies of the two highest measurable vibrational modes is shown in the inset. (b) Histograms of the vibrational mode frequencies measured for a Pt junction containing H_2, HD and D_2 respectively. The peak centers (marked by arrows) and widths (marked by error margins) have been scaled by the expected isotope shift. Reproduced from Ref. [8]

In Fig. 7.3(a) differential conductance curves for a Pt-D_2-Pt contact are shown. The downward steps in the differential conductance can be interpreted as inelastic scattering events. In general the observed frequencies are in the range 40-100 meV which is much higher than the typical phonon frequencies of bulk Pt [161]. The associated vibrational modes must therefore involve deuterium, and similarly hydrogen, in either its molecular or atomic form.

A comparison between PCS measurements on junctions containing H_2 and the isotopes HD and D_2 respectively (see Fig. 7.3(b)) reveals that the frequencies scales with the mass factors $\sqrt{m_{HD}/m_{H_2}} = \sqrt{3/2}$ and $\sqrt{m_{D_2}/m_{H_2}} = \sqrt{2}$. Strong evidence that the junction contains molecular and not atomic hydrogen is provided by the fact that the vibrational frequencies observed for HD is not simply a statistical mixture of the frequencies found for H_2 and D_2.

For particular stable contacts it is possible after measuring a dI/dV curve to stretch the contact further within the 1 G_0 regime and measure a new differential conductance curve. Hereby, the response of the vibrational modes to stretching is revealed (see inset in Fig. 7.3(a)). In general, it is observed that the two lowest lying modes increase their frequencies as the contact is stretched whereas the energy of the highest observable mode (only accessible experimentally for D_2) decreases.

Theoretical analysis

In the following sections we present theoretical evidence that the idealized structure consisting of a hydrogen molecule bridging the platinum electrodes represents a good model for the real experimental junction. The majority of the material presented in this section represents a literature study. However the estimation of the dissociation barrier of H_2 are new not yet published material.

In their original paper on the platinum/hydrogen junction Smit *et al.* proposed, on the basis of their experimental results and a relatively sparse set of DFT calculations that the plateau at 1 G_0 is due to a stable structure where a single hydrogen molecule is bridging the Pt electrodes (see inset of Fig. 7.7) [7]. Although later reported conductance calculations have shown significant variation (see Sec. 5.2) there is substantial evidence that the relevant structure is indeed the linear bridge configuration [8]. An alternative configuration where the H_2 molecule is dissociated in the contact has been proposed, however, this junction yields a conductance larger than 1 G_0 with contributions from three channels [32]. In the remaining part of this section the focus will be on the theoretical results by Thygesen *et al.* [10, 8, 162] as they form the starting point for the results presented in Paper I and V.

Stability issues

The strong experimental evidence for the repeated formation of a stable Pt junction containing molecular hydrogen seems to contradict with the well known fact that hydrogen dissociation on Pt surfaces is non-activated [163]. Moreover, the activation barrier for dissociation of hydrogen over stretched atomic gold wires is lowered by a factor 10 as compared to flat gold surfaces. An enhancement of reactivity which is also expected to be found in the case of platinum wires [164, 165]. A hypothesis which is supported by the fact that low-coordinated Pt atoms found at steps, kinks and edges are even more chemical active than surface atoms enhancing the dissociation rates at these sites [166, 167, 168]. We notice that, in the case of CO oxidation, this enhanced activity for low-coordinated sites actually makes platinum a worse catalyst [169] as the reactants and products are bound to strongly. This is an observation which might help explaining how the bridge junction can be formed experimentally.

A possible formation path involves the immediate dissociation of all hydrogen molecules at the platinum electrodes. As a consequence the surface will be covered with a monolayer of strongly bound atomic hydrogen, which makes the surface inactive as a catalyst. When the contact is broken the hydrogen atoms are expected to be to strongly bound to diffuse into the contact neck. Instead a chemisorbed or free hydrogen molecule can sometimes be incorporated into the hydrogen covered metal neck. We do not expect the elastic transport properties of the contact to change significantly by hydrogen adsorption at the electrode sides.

Next the question of whether the molecular hydrogen bridge is stable once the contact is formed arises. DFT calculations[1] presented by Thygesen in Ref. [162] (see Fig. 7.4) indicates that for sufficiently low coordinated platinum contacts and electrode displacements in the range 1.2-2.3 Å the linear bridge is stable and even energetically favorable.

In order to quantify the stability of a hydrogen molecule in a platinum junction we employed the nudged elastic band method (see Sec. 2.4.1) to get a crude estimate of

[1]Total energies were found by relaxing at least the hydrogen molecule and platinum tip atoms using the DFT code Dacapo [1, 2].

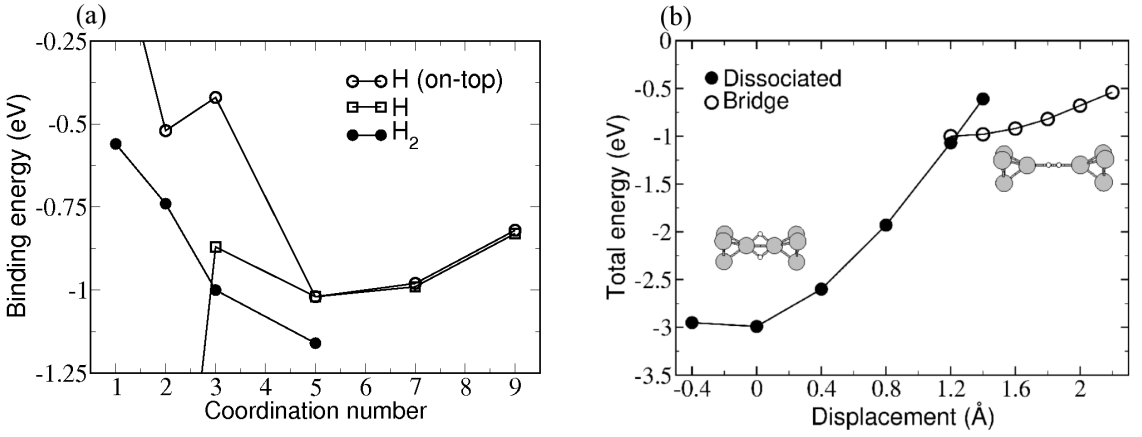

Figure 7.4: (a) Binding energy of a linear H_2 bridge (filled circles) placed between Pt electrodes with varying coordination number, N_c, for the tip atom. For comparison the binding energy of a single H atom - either being allowed to relax (squares) or constrained to the on-top sites (circles) - adsorbed at the Pt tip atom is shown. (b) Total energies of the dissociated configuration (filled circles) and the linear bridge configuration (circles) for different electrode displacements and in the case where $N_c = 3$. For both (a) and (b) the energy is measured relative to the gas phase H_2 and two infinitely separated Pt electrodes. Reproduced from Ref. [162].

the actual dissociation barrier. The initial structure was model by a hydrogen molecule bridging platinum tip atoms with $N_c = 3$, and the final state was found by relaxing both hydrogen atoms and the platinum pyramids in a dissociated structure (see inset of Fig. 7.5). In the supercell description the hydrogen atoms and pyramids are attached to Pt (111) surfaces with 2×2 atoms in the surface plane. We used the total-energy code DACAPO [1, 2] to relax both hydrogen molecule and platinum pyramids in order to obtain stable junction structures.

Once the hydrogen molecule is captured between the two electrodes we find that the barrier for the molecule to dissociate and escape the constriction is in the order of 0.35 eV (see Fig. 7.5). This indicates, that the linear bridge configuration is indeed stable in the experiments performed by the group of Ruitenbeek where the temperature is around 4.2 K[2]. We notice that, if the experiments were performed at room temperature the configuration is predicted to be highly unstable and the captured molecule would dissociate immediately.

In passing we notice that Barnett *et al.* [170] find no barrier for incorporation of a hydrogen molecule in an almost broken Au contact. This barrierless insertion of the hydrogen molecule likewise indicates that the linear bridge configuration is energetically stable.

Vibrational modes

In this section the vibrational frequencies of a molecular hydrogen bridge between platinum electrodes are discussed and compared to the experimental values. As the inelastic calculations presented in Sec. 7.3 relies heavily on these results we discuss them in more detail.

[2]To obtain an estimate of the dissociation rate we have used the rate equation $r = \nu e^{-E_{TS}/k_B T}$, where ν is taken as the highest vibrational mode (M1) (see Sec. 7.1.1).

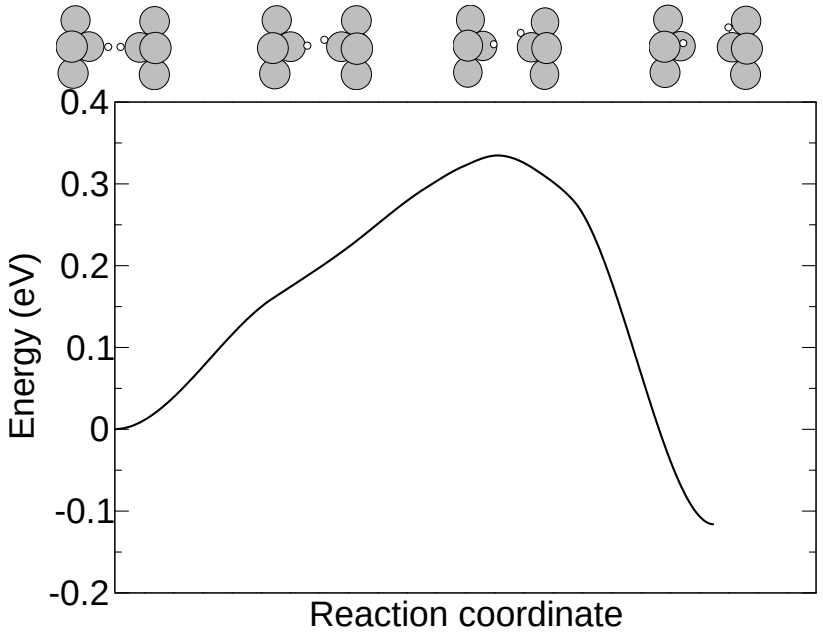

Figure 7.5: Potential energy diagram for the dissociation of a hydrogen molecule bridging two platinum tip atoms. The initial and final state together with some representative intermediate states are shown as insets.

The vibrational eigenmodes, $\{\mathbf{Q}_\lambda\}$, and corresponding frequencies, $\{\omega_\lambda\}$, of the H_2 molecule in the linear bridge configuration (see inset of Fig. 7.6) are obtained by diagonalizing the dynamical matrix of the system which in turn is calculated from the DFT total energies [3] by finite differences. Thanks to the large difference in mass between the metal and hydrogen atoms, the dynamical matrix for the two H atoms can be calculated keeping all metal atoms fixed. Following this procedure a longitudinal stretching mode (M1), a longitudinal center-of-mass mode (M2), as well as two pairwise degenerate transverse modes referred to as hindered rotations (M3) and hindered transverse center of mass modes (M4) are obtained.

In Fig. 7.6 the stretching dependence of the six vibrational frequencies of the captured hydrogen molecule are shown [8]. For comparison with the experimentally observed frequencies Djukic *et al.* [8] focused on electrode displacements in the range 1.7-2.0 Å as the calculated conductance of these structures are found to be close to 1 G_0. Taking the experimental error bars into account the agreement between the mean values or peak centers of the experimentally observed frequencies (see Fig. 7.3(b)) at 54, 72 and 126 meV and the range of calculated frequencies at 30-42, 64-92 and 123-169 meV is satisfactory.

For moderate stretching length the two longitudinal modes, M1 and M2, are highest in frequency. Up to an electrode displacement of around 1.9 Å the frequency of M1 decreases as the H-H bond becomes stretched. As the molecule starts to retract the frequency increases approaching that of the free molecule. The M2 mode becomes softer as the Pt-H bond is stretched and is thereby characterized by a decreasing frequency as the contact is stretched. The lowest lying frequencies are the two doubly degenerate transverse vibrations M3 and M4. Both types of modes are characterized by an increasing frequency

[3] The self-consistent DFT code DACAPO [1, 2] is employed to calculate the ground state energies.

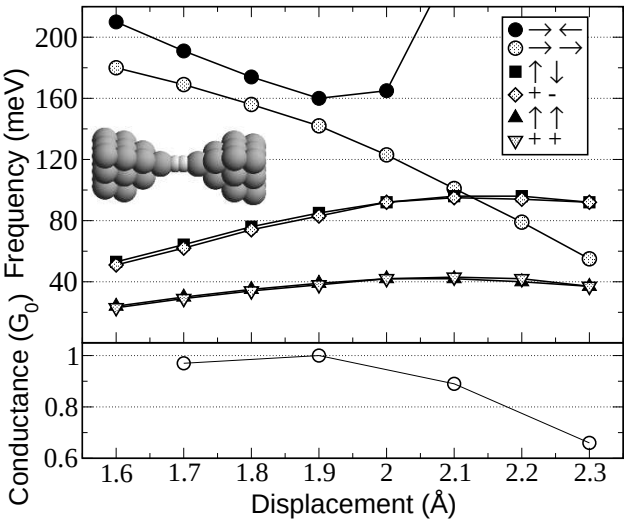

Figure 7.6: Stretching dependence of the calculated vibrational frequencies for a hydrogen molecule in the linear bridge configuration. The symmetries of the oscillations are shown by arrows in the inset. Reproduced from Ref. [8].

as the contact is stretched.

Experimentally the two lowest lying frequencies are observed to increase as the junction is stretched while the highest frequency (only observable for D_2) decreases. Clearly, this agrees qualitatively with the variations of the calculated frequencies. Quantitatively, though, the calculated frequency shift is about an order of magnitude larger than the one observed experimentally (see Fig. 7.6 and 7.3(a)). A possible explanation of this discrepancy is built on the fact that experimentally the electrode displacement is controlled far away from the molecular junction. Consequently the elastic response of the electrode region has to be taken into account when directly comparing stretching lengths. In fact simulation of atomic chain formation in gold during contact breaking reveals that most of the deformation happens in the nearby contact-necks [171].

Conductance calculations

In this section we discuss the electrical properties of a hydrogen molecule bridging two platinum electrodes.

In Ref. [10] Thygesen *et al.* present calculations of the transmission function of a platinum/hydrogen junction. The supercell structure used in the calculations is shown in Fig. 7.16, where the electrode distance of 14.60 Å has been chosen to make the calculated vibrational frequencies of the captured H_2 molecule match the experimental values as close as possible. The conductance calculations have been performed using method 1 as described in Sec. 4.3.1.

In agreement with the experimental results the conductance was found to be close to 1 G_0, where indeed the transmission function has a wide plateau with $T \approx 1$ around the Fermi energy (see Fig. 7.7). In order to gain insight into the conduction mechanism of the platinum/hydrogen system, Thygesen *et al.* resolved the full transmission into contributions from the H_2 bonding and anti-bonding states. This revealed that for energies above -3 eV the removal of the bonding state does not affect the transmission significantly (see Fig. 7.7). From this observation the authors concluded that the conductance is mainly

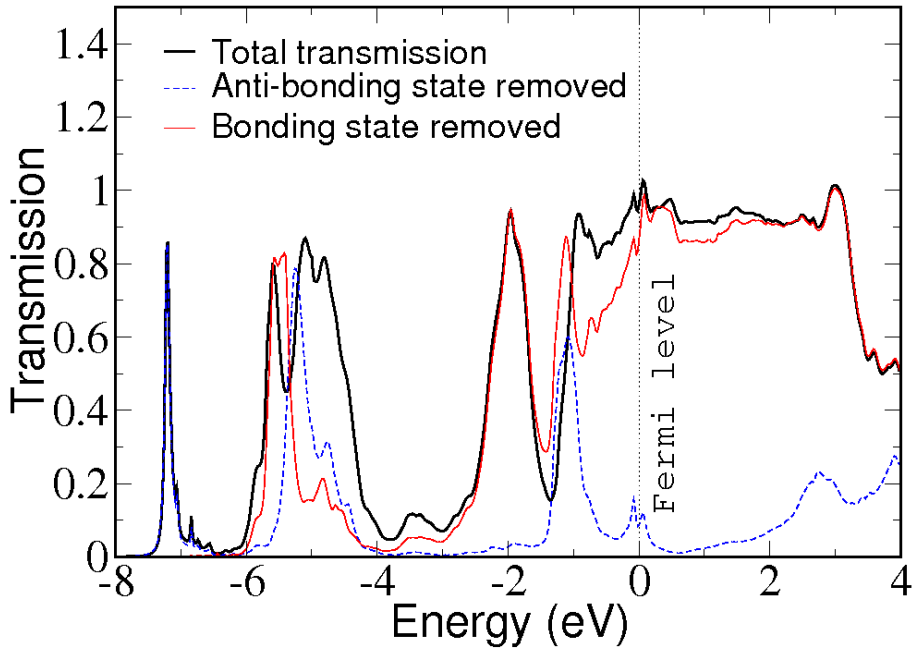

Figure 7.7: Transmission function (black curve) for the Pt-H_2-Pt junction. The calculated transmission when all coupling to the hydrogen bonding (anti-bonding) state has been cut is shown in the red (blue) curve. Reproduced from [10].

due to transmission through the H_2 anti-bonding state.

We find further support for this explanation of the conduction mechanism by visualizing in Fig. 7.8 the *s* symmetric eigenchannel which carries more than 95% of the current. Clearly, the electron transport is mainly mediated by the H_2 anti-bonding state. The eigenchannels were determined using the calculational procedure described in Ref. [73] in combination with method 2, Sec. 4.3.2, and a SZP basis set. As the transmission functions calculated using the two implementations of NEGF-DFT are almost identical around the Fermi level (see Sec. 5.2) we expect the respective eigenchannels to be very similar.

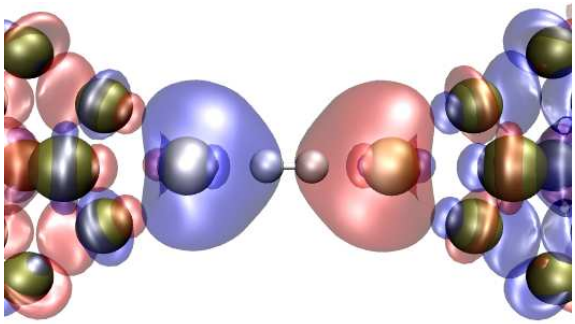

Figure 7.8: Isosurface of the almost fully open eigenchannel at the Fermi level for a platinum/hydrogen contact. It is seen that the electron transport is mediated by the anti-bonding H_2 molecular orbital. The eigenchannel is found using the method of Paulsson *et al.* [73] and method 2 with a SZP basis set.

The important factors in the conduction mechanism described above are the close proximity of the H_2 anti-bonding state to the Fermi level of the electrodes and its strong

hybridization with platinum states. This is in good agreement with the traditional picture of hydrogen dissociation on metal surfaces [163]. When the hydrogen molecule is approaching the surface the anti-bonding state is shifted downwards, and when crossing the Fermi level it is partially filled, which weakens the H-H bond. This expected weakening of the H-H bond is in accordance with the observed increase of the H-H bond length for the hydrogen molecule in the platinum junction.

7.1.2 The plateau at low conductances

In this section, we present experimental and theoretical evidence that the low conductance peak in the platinum/hydrogen histogram is due to the formation of a hydrogen decorated Pt chain. The material discussed in this section is a summary of Paper I.

For 92 % of the individual traces the conductance decreases by small steps after the plateau around 1 G_0. This indicates that atomic structures having conductance below 1 G_0 are formed by stretching the original Pt/H_2 linear bridge configuration beyond elastic deformation. As can be seen from the conductance trace in Fig. 7.2(b) the structure can be stretched over quite long lengths suggesting the formation of an atomic wire.

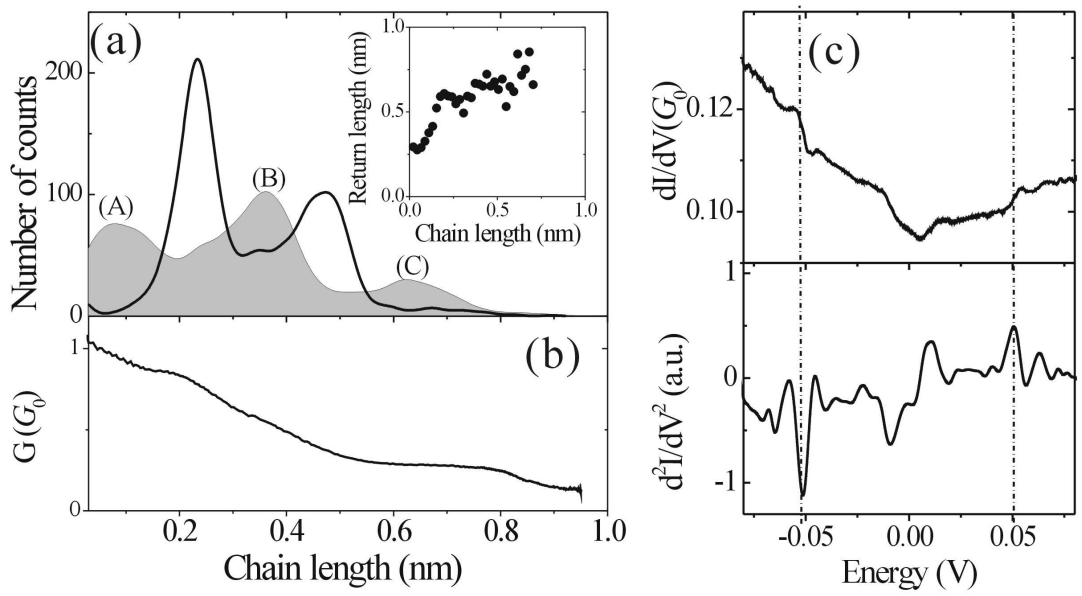

Figure 7.9: (a) Length histogram for clean Pt (black curve) and Pt when H_2 has been admitted (filled graph). The average return lengths as a function of chain length is shown in the inset. (b) Average conductance as a function of chain length. (c) dI/dV curves (top) and their numerical derivatives (bottom) for a Pt/H_2 junction taken at a conductance of 0.1 G_0. From Paper I.

In Fig. 7.9(a,b) we show, for platinum/hydrogen junctions, the length histogram and the average conductance as a function of the chain length. The length histogram is constructed by recording the distance a Pt/H_2 contact may be pulled from the point where the conductance drops below 1.3 G_0 until it reaches 0.1 G_0. A sequence of peaks with a distance of 0.27 nm is observed indicating the repeated occurrence of certain stable chain configurations. The average conductance (shown in Fig. 7.9(b)) of these characteristic

structures denoted (A), (B) and (C) are 0.96, 0.56 and 0.28 G_0, respectively.

Since the average conductance of structure (A) is close to 1 G_0, it is identified as the linear bridge configuration discussed in the previous section. Looking at the individual traces, it is observed that in most cases the conductance decreases in small steps after the appearance of a plateau near 1 G_0. This suggests that the hydrogen molecule is still bridging the contact after stretching it beyond the 1 G_0 plateau. Further support for this interpretation is found from PCS measurements taken at low conductances. In Fig. 7.9(c) the differential conductance and its derivative is shown for a Pt/H_2 junction having a conductance of 0.1 G_0. The upward steps in the dI/dV curve is interpreted as vibrational excitations with a frequency of 51 meV. It is noted that, in most measurements peaks are observed in the first derivative instead of the second derivative [160]. A vibrational excitation energy of 57 $\pm$ 4 meV is commonly observed for Pt/H_2 contacts taken at conductances in the range 0.1-0.6 G_0. This frequency agrees with the vibrational energy of the hindered transverse CM modes (M4) of the hydrogen molecule in the linear bridge configuration. The close agreement indicates that H_2 is indeed still bridging the stretched contact.

In the inset of Fig. 7.9(a) the average return length as a function of chain length is shown. This is the average distance over which the two electrodes need to be moved back after the junction breaks in order to reestablish contact. The approximately proportional relation suggests that a fragile structure not able to support itself and with a length corresponding to the last plateau is formed. This interpretation is further strengthened by the results presented in Fig. 7.9(a,b). The peak distance observed for the Pt/H_2 contact is slightly larger than the distance between atoms in a clean Pt-wire (0.23 nm) [172] indicating that the low conductance structure is probably not a clean Pt-wire. Further support for this interpretation is found by the rapid decrease of the average conductance observed as the chains are being pulled (see Fig. 7.9(b)). Although the conductance of pure Pt chains decrease with length [173] it is always well above 1 G_0.

We notice that, in the conductance histogram an additional peak is only observed at 0.2 G_0 corresponding to structure (C). This observation can be explained by the fact that the conductance varies more slowly with stretching for structure (C) than for structure (B) in fact a stable level near 0.2-0.3 G_0 is observed at 0.6-0.8 nm (see Fig. 7.9(b)).

Based on the experimental evidence presented above we arrive at the chain formation model. First, a single hydrogen molecule is bridging the Pt contact. Further stretching incorporates one and later two Pt atom into the chain. The larger distances in the length histogram and the low conductance should then be attributed to additional hydrogen decorating the Pt atomic chain.

Theoretical analysis

In this section, we present NEGF-DFT calculations which provides additional support for the chain formation process used to explain the low conductance peak in the Pt/H_2 histogram.

Based upon the experimental evidence presented above we came to consider the model structures for the hydrogen decorated platinum wires illustrated by the insets in Fig. 7.10. Due to high computational costs the energy/conductance traces and the analysis of the transport mechanism have been performed for an atomic wire system (see inset in Fig. 7.11(b)). For structure (B) we have compared the transmission functions of the atomic wire system with that of the more realistic contact. Qualitatively, the results

are similar in terms of the main peak structures illustrating that the analysis is robust with respect to the atomic arrangement. In a quantitative comparison, however, the conductance of the wire system is approximately a factor of 2 lower. In order to ensure that the KS potential is converged to bulk values we include 3-4 surface layers on each side of the platinum pyramids and a chain of six platinum atoms on each side of the hydrogen atoms, respectively. To obtain stable junction structures we used DACAPO [1, 2] to relax the pyramids and the hydrogen decorated chain segment using a linear constraint to avoid buckling of the wire. Hereby investigating the characteristics of a quite stretched platinum/hydrogen contact. The conductance is calculated using method 1 as described in Sec. 4.3.1 and each transmission function has been sampled by 8 irreducible $\mathbf{k}_\perp$ points.

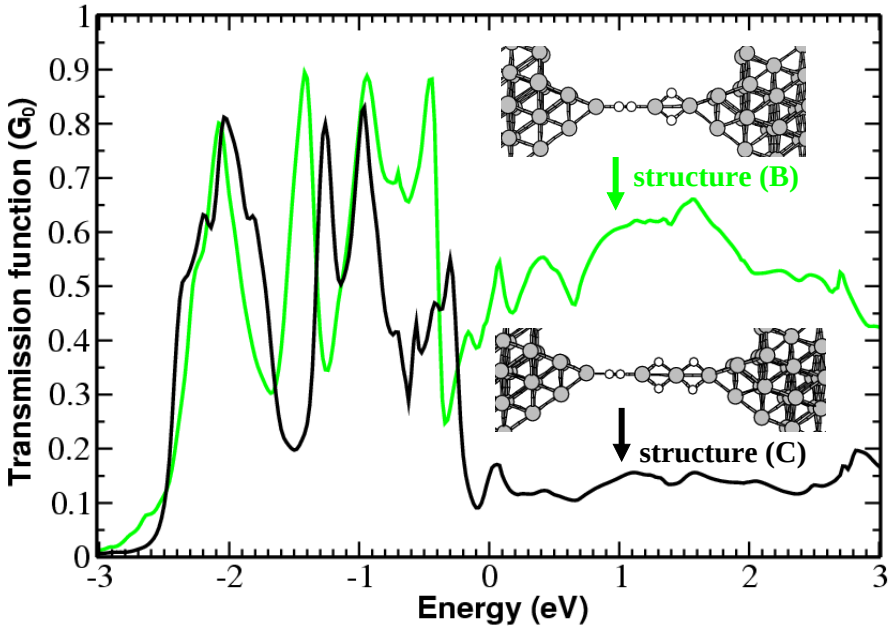

Figure 7.10: Calculated transmission functions for the structures (B) [green line] and (C) [black line] proposed to explain the low conductance features in the histogram. The conductance of the structures is read-off at the zero-point of the x axis which is taken to be the Fermi level. The explicit geometries of the structures are shown as insets. From Paper I.

By performing total energy calculations for varying contact distances the optimal length of a hydrogen decorated platinum wire segment was found to be 0.272 nm in good agreement with the experimental results. In Fig. 7.10 the transmission functions for the optimized structures (B) and (C) is shown. By comparing with Fig. 7.7 it is seen that the 1 G_0 plateau found for structure (A) - the linear bridge configuration - is lowered when additional hydrogen decorated platinum atoms is incorporated into the chain. The conductances are found as 0.46 and 0.15 G_0 for structures (B) and (C), respectively, which is in reasonable agreement with the experimental values of ≈ 0.6 and ≈ 0.3 G_0.

In principle, there are three possible explanations of the lowering of the 1 G_0 plateau observed when going from structure (A) to (C):

(i) An interference effect, where the orbitals of the additional hydrogen atoms would play a direct role in the scattering at the Fermi level.

(ii) The hydrogen decoration modifies the conductance by changing the Pt-Pt distance.

(iii) The additional hydrogen changes the conductance by modifying just the electronic structure of the Pt atoms.

All three possible effects were investigated independently and the first two could be ruled out. By resolving the full transmission of structure (A) into contributions from the *s*- and *d*-orbitals at the neighboring Pt atoms, we show that the effect of hydrogen decoration can be simulated by systematically removing different orbitals at the neighboring platinum atom from the basis set. This technique is illustrated in Fig. 7.11(a) where the results of calculations for a clean chain of single platinum atoms bridged by a H_2 molecule is shown. Removing the *s*-orbital for one and two subsequent platinum wire atoms accounts for the successive reduction of the transmission for energies above 1 eV. For reduction of the transmission at lower energies, and therefore the conductance, also part of the platinum *d*-orbitals must be removed from the basis set. It is noted that, the removal of the *d*-orbitals alone does not have a large effect on the conductance.

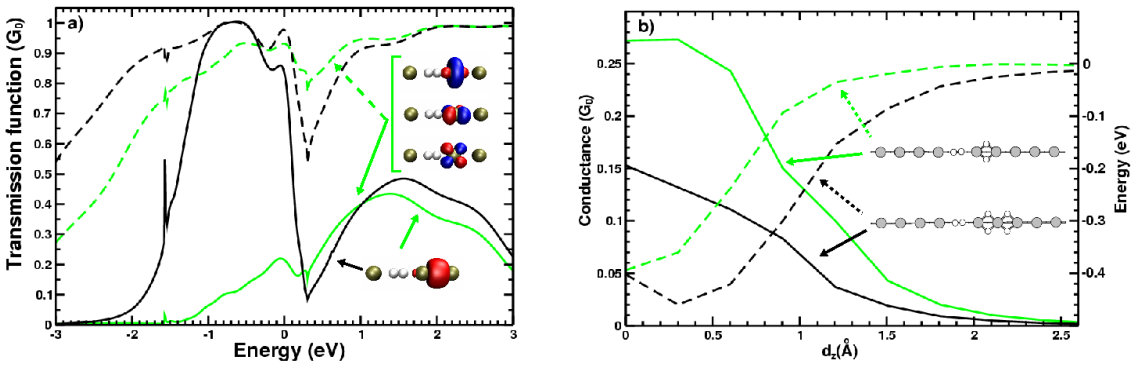

Figure 7.11: (a) Transmission function obtained for a hydrogen molecule bridging atomic platinum wires [dashed black curve]. To illustrate the effect of hydrogen decoration on the first neighboring platinum atom the *s*-orbitals [solid black curve], *d*-orbitals [dashed green curve] and both *s*- and *d*-orbitals [solid green curve] have been removed from the basis set. In the inset the relevant *s*- and *d*-orbitals are shown superimposed on the atomic position. (b) Simulated conductance traces [solid curves] and DFT binding energies [dashed curves] as a function of electrode displacement (d_z) for structures (B) and (C). As shown in the inset the three dimensional electrodes have been replaced by Pt atomic wires. From Paper I.

Our analysis shows that the conductance reduction is due to the additional hydrogen atoms saturating the *s*- and part of the *d*-orbitals between the platinum atoms they are attached to, thereby making them unavailable for transport. We point out that this explanation of the conductance reduction is not in contradiction with the one given by Barnett *et al.* [170] for Au-H_2-Au system but just offers a different perspective.

The stretching dependence of the conductance for structure (B) and (C) in the atomic wire system is shown in Fig. 7.11(b). Although there is a the short plateau in the conductance for structure (B) when stretched beyond the optimal bonding distance, for structure (C) the overall decrease with length seems to be slower up to a stretching length of 0.1 nm. This trend was also found in the experimental histograms.

Formation path

To gain some insight into the formation path that may lead to the structures (B) and (C) we investigated whether the hydrogen bridge is strong enough to pull out a Pt wire. The chain formation process were simulated by changing the electrode distance gradually by

hand and relaxing the atomic structures at each step. Within this scheme we could pull a wire for the pure platinum contact but when placing the hydrogen bridge in the middle of the contact, the contact always broke in such a fashion that the molecule was split into its atomic compounds. In Fig. 7.12 the approach is illustrated for a geometry designed to help the wire pulling as much as possible by uplifting the Pt tip atom.

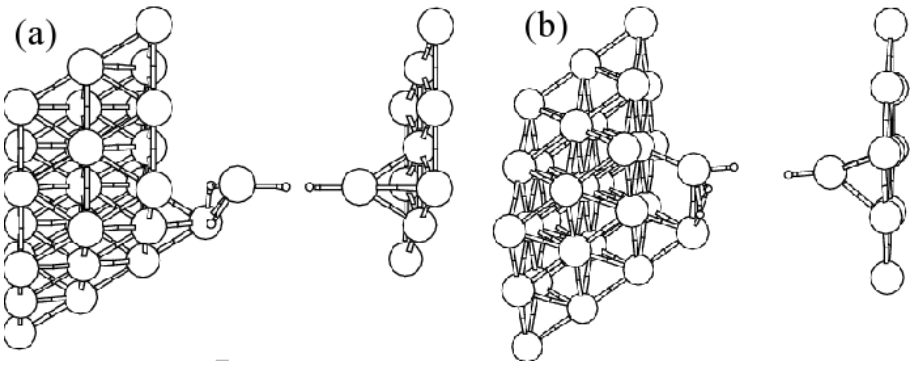

Figure 7.12: (a) The unrelaxed configuration. By uplifting the Pt tip atom (which is supposed to be pulled) away from the surface by hand wire pulling was favored as much as possible. (b) The relaxed configuration. Even for this favorable geometry the Pt tip atom relaxed backwards and wire pulling was prevented.

The simulations indicate that, since the bridging H_2 molecule is very weakly bond to the Pt electrodes, "wire pulling" seems unlikely. Instead we imagine structure (B) and (C) to be formed by a concerted process. A possible scenario involves the displacement of platinum atoms at the surface due to phonons and the formation of intermediate structures with the additional hydrogen adsorbed on the electrodes. The configurational space for covering all possibilities for atomic movements in such a process is though too large to be explored by our calculations in detail.

7.1.3 Summary

Conductance histograms for a platinum junction in a hydrogen atmosphere show peaks at 1 G_0 and 0.2 G_0, respectively. By reviewing experimental and theoretical results for the 1 G_0 plateau it was found that a complete agreement between the number of vibrational modes, the sign of their stretching dependence, the conductance and the number of conductance channels exist if the experiments are interpreted in terms of a configuration where a single hydrogen molecule is bridging the platinum electrodes.

Furthermore experimental evidence that stretching of the linear bridge configuration can form an atomic wire giving rise to the peak at 0.2 G_0 was presented. An interpretation of this result in terms of the formation of an atomic platinum chain decorated with hydrogen was compared to DFT calculations. The numbers for the bond distances and conductances was found to be in fair agreement with experiments. The pathway that brings new atoms into the atomic chain structure remains problematic though.

7.2 The gold/hydrogen junction

In this section, we provide a short overview of the main experimental and theoretical results on a gold/hydrogen junction. Moreover, the calculated transmission function of a

hydrogen molecule bridging gold electrodes is presented and compared to the transmission of a platinum/hydrogen junction.

Csonka *et al.* [147] used the mechanically controlled break junction technique to measure conductance traces for gold wires broken in a hydrogen environment at T = 20 K. In the resulting conductance histograms they observed a clear peak around 0.5 G_0. This half-conductance quantum was interpreted as the onset of a dimerization within the atomic gold wire in the last stage of breakage. The formation of gold dimers was thought to be accompanied by a stabilization effect due to the adsorbed molecular hydrogen. More recent calculations by Jelinek *et al.* [164] show that the histogram peak at 0.5 G_0 can also be due to hydrogen atoms chemisorbed to the atomic gold chain. In MCBJ experiments reported by Thijssen *et al.* [148] it is found that the fractional conductance peak disappears when the temperature is lowered from 20 to 5 K. This observation might be due to the fact that at higher temperatures hydrogen is more easily dissociated.

Conductance histograms for the Au/H_2 junction recorded at T = 5 K shows a clear peak around 1 G_0 as well as a large background with no clear features at lower conductances [148]. In all individual conductance traces a stable plateau around 1 G_0 is observed, indicating that a contact consisting of a single gold atom is reached [174]. Upon further stretching the conductance drops considerably and varies between 0 and 1 G_0 until the contact finally breaks. To further characterize the Au/H_2 junction Thijssen *et al.* investigated the vibrational properties of the junction by performing point contact spectroscopy measurements. For Au/H_2 junctions with conductances below 1 G_0, conductance fluctuations often mask the regular vibrational mode signal. Instead, the vibrationally induced two-level fluctuation model can be used to identify the frequencies from the symmetric features (peaks/dips) observed in the dI/dV curves [160]. By comparing the combined measurement of the stretching dependence of the vibrational modes and the zero-bias conductance to calculations reported in the literature [175, 164, 170] substantial evidence was found that hydrogen is mostly incorporated in the gold junction in molecular form at T = 5 K.

7.2.1 Conductance calculations

In this section we address the electron transport properties of a gold contact with a hydrogen molecule at the linear bridge site. Based on the first principle calculations of the transmission function we find that as compared to the platinum/hydrogen system the plateau determining the conductance is lowered and the overall peak structure is downshifted. The conductance mechanism of the Au/H_2 junction is complicated by the delocalized gold *s*-states which lead to a direct coupling across the hydrogen molecule.

The supercell geometry (shown in Fig. 7.13(a)) represents a model structure of a single Au/H_2 junction taken at a specific stretching length. The corresponding distance between the Au electrodes were chosen by total energy minimization. We used DACAPO [1, 2] to relax the hydrogen molecule and the pyramids keeping the rest of the Au atoms fixed in the bulk positions. The transmission function is calculated using method 1 as described in Sec. 4.3.1 and averaged over 8 irreducible $\mathbf{k}_\perp$ points. The eigenchannels are found by the technique described in detail in Ref. [73] and method 2 (see Sec. 4.3.2) with a SZP basis set. In Fig. 7.13(b), we show the transmission functions calculated using method 1 and 2. As qualitatively the results are similar we expect the symmetry of the eigenchannels found using method 1 or 2 to be identical.

In Fig. 7.14(black) we show the calculated transmission function. Notice that the

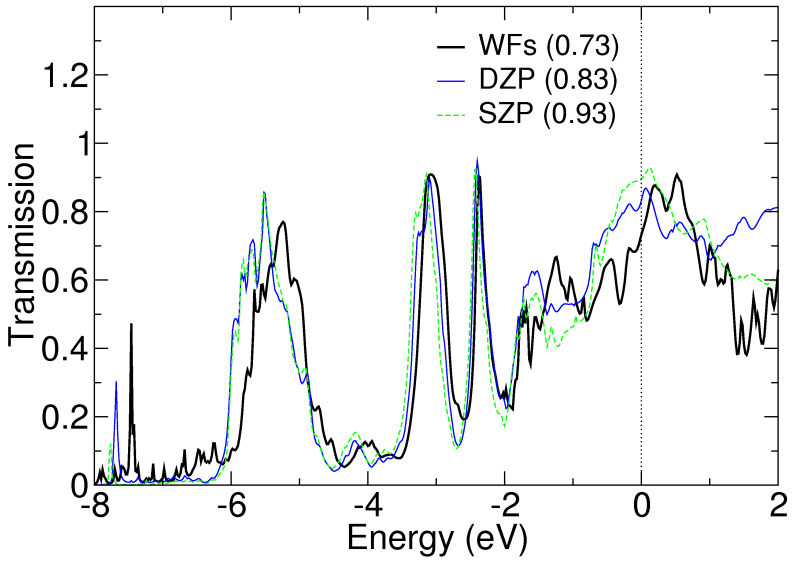

Figure 7.13: (a) Supercell used to model the central region of the Au-H_2-Au junction. (b) The calculated transmission function for the Au/H_2 contact using method 1 and 2. The conductance is indicated in the parenthesis following the legends.

transmission is only plotted up to 2 eV above the Fermi level. This is because at higher energies the result is sensitive to the parameters used to construct the Wannier functions.

In the following, we compare the transmission functions of a Pt/H_2 (see Fig. 7.7) and a Au/H_2 junction. Qualitatively, the peak structure of the two junctions are very similar. Quantitatively, we observe a downshift of the peaks and a lowering of the 1 G_0 plateau when replacing Pt with Au. The latter effect is a consequence of the fact that Au have no *d*-states at the Fermi level. This is because removing part of the platinum *d*-orbitals from the basis set accounts for a lowering of the 1 G_0 plateau as illustrated in Fig. 7.11(a). The observed downshift is of the order of 1 eV which is consistent with the fact that the work function of Pt(111) is 0.6 eV lower than that of Pt(111) [176].

To further analyze the reduced plateau crossing the Fermi level we resolve the full transmission into contributions from the bonding and anti-bonding H_2 states. As seen in Fig. 7.14 for energies above -4 eV the removal of the bonding state has no significant effect on the transmission. Unlike what is found for the Pt/H_2 junction a significant conductance is still observed when the anti-bonding state is removed from the basis set. This transmission is due to the delocalized Au *s*-states which lead to a direct coupling across the hydrogen molecule. We thus conclude that the plateau determining the conductance is due to transmission through a state located at the hydrogen molecule and formed as a linear combination of the H_2 anti-bonding state and the *s*-states at the Au tip atoms.

We test this interpretation by plotting in Fig. 7.15 the right-going eigenchannel which carries almost 100% of the current. As compared to the Pt/H_2 eigenchannel (see 7.8), which clearly has anti-bonding character at the hydrogen molecule, the Au/H_2 is seen to have a more complicated conduction mechanism. This could well be explained by the the fact that the *s*-states of Au is more delocalized than for Pt. We notice that the asymmetry of the eigenchannel reflects that a substantial amount of electrons are back-scattered at the interface.

Note that the calculated conductance agrees well with the results of Ref. [175], but differs significantly from Ref. [170] that ascribes less than 0.25 G_0 to a Au/H_2 junction.

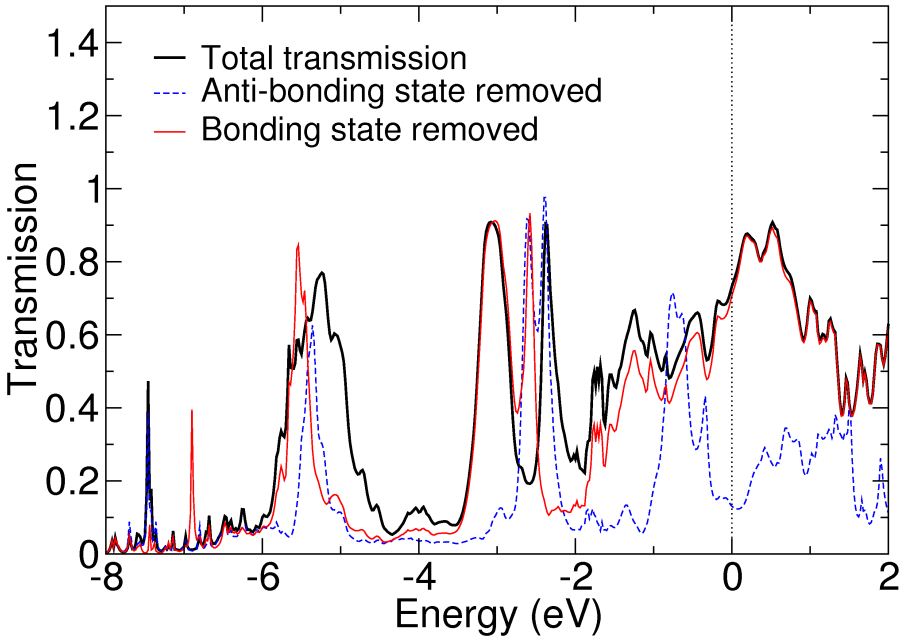

Figure 7.14: Calculated transmission (black curve) for the gold/hydrogen contact as shown in Fig. 7.13(a). The transmission when all coupling to the hydrogen bonding (anti-bonding) state has been cut is shown in the red (blue) curve.

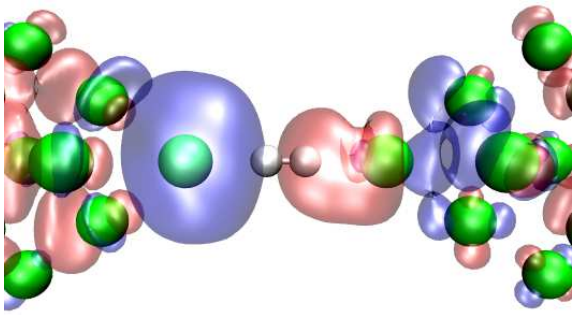

Figure 7.15: Isosurface of the left eigenchannel which conduct almost 100% of the current through a gold/hydrogen contact. It is seen that the electron transport is mediated by a combination of the anti-bonding H_2 molecular orbital and the delocalized *s*-states from the neighboring Au atoms.

7.3 Inelastic scattering in metal-H_2-metal junctions

In this section we present first-principle calculations of the dI/dV characteristics of a H_2 molecule bridging Pt and Au electrodes in the presence of electron-phonon interactions. The fact, that the hydrogen junction supports a single, almost fully open conductance eigenchannel suggests that the inelastic-scattering processes should be particular simple to understand (see Sec. 3.3.3). As expected the conductance is found to decrease at threshold voltages corresponding to the excitation energy of the longitudenal vibrational modes of the H_2 molecule. Surprisingly, in the case of Pt electrodes the transverse modes lead to an *increase* in the differential conductance, while for gold electrodes they have no effect on the transport. Scattering theory is used to show that this feature is a result of a

coupling between the nontransmitting d-channels and the transmitting s-channel mediated by the transverse vibrational modes.

The supercell geometry of the considered hydrogen contact is shown in Fig. 7.16. The distance between the two electrodes, or equivalently the length of the supercell, has for the case of Pt been chosen to make the calculated vibrational frequencies of the H_2 molecule match the experimental values as close as possible (see Sec. 7.1.1). For the case of Au where the experimental data is less conclusive, we have chosen the distance by minimizing the energy. The vibrational modes of the junctions are sketched in the inset of Fig. 7.17 and the corresponding frequencies are given in the caption. Using DACAPO [1, 2] we have relaxed the pyramids and hydrogen molecule to obtain stable junction geometries. The conductance is calculated using method 1 as described in Sec. 4.3.1 and each differential conductance curve has been sampled by 8 irreducible $\mathbf{k}_\perp$ points.

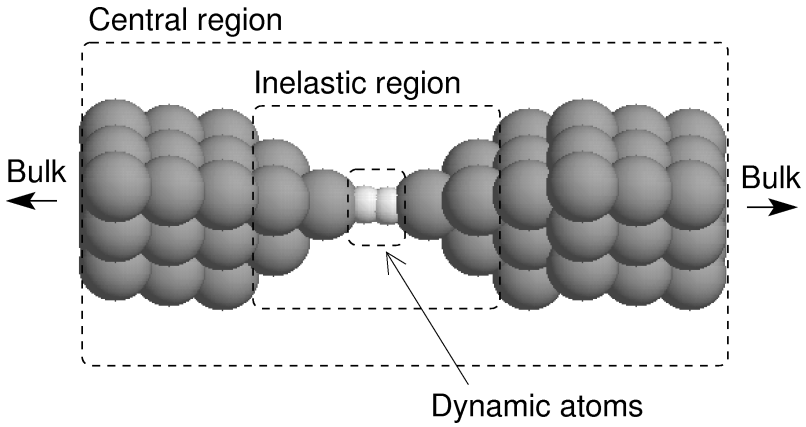

Figure 7.16: The supercell used to model the metal/hydrogen junction. Only the hydrogen atoms are allowed to vibrate (the "dynamic" atoms). This is a good approximation due to the large mass difference between the Au/Pt and H atoms. The effect of the potential generated by the vibrating hydrogen molecule is included inside the indicated inelastic region. The central region is coupled to bulk electrodes and periodic boundary conditions are imposed perpendicular to the contact axis. From Paper V.

In Fig. 7.17 we show the differential conductance calculated from (3.2) including scattering on different vibrational modes separately. To extract the features due to the inelastic scattering from those due to elastic scattering we have subtracted the elastic signal, i.e. we plot $G(V) = G_{\rm full}(V) - G_{\rm el}(V) + G_{\rm el}(V=0)$, see Ref. [70] for a discussion of this procedure. It is noted that the differences in the zero-bias conductances are due to the tails of the electron-phonon self-energies, which although centered around the vibrational frequencies also have weight at other energies.

The conductance curves of Fig. 7.17 present several interesting features: For both Pt and Au the longitudinal modes lead to a decrease in the conductance as expected from the one-channel model. It is noticed that the internal stretching mode has a much larger impact on the electrons than the CM mode. For Au, the transverse modes have no effect on the transport, while for Pt they lead to an *increase* in the conductance. Since the junction has one fully open channel this seems to conflict with the one-channel model which would predict an increase only for junctions with conductance $< 0.5G_0$. It is noted that, we have obtained similar quantitative features in the dI/dV curves by using method 2 (see Sec. 4.3.2) and LOE for including the electron-phonon interaction. Moreover, Magnus Paulsson, by using their inelastic transport code (described in detail in Ref. [70]), likewise

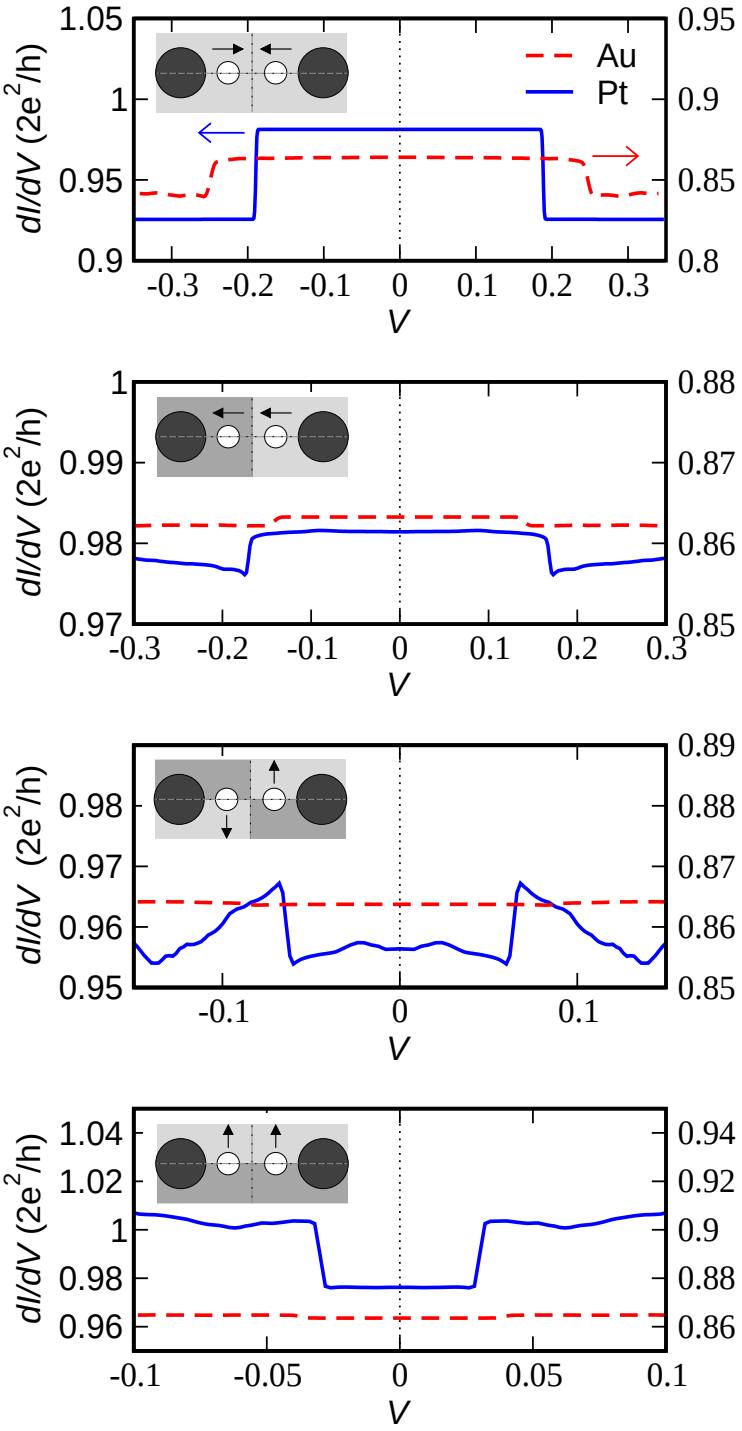

Figure 7.17: Differential conductance of a hydrogen molecule bridging platinum (full) and gold (dashed) electrodes when scattering on a single vibrational mode is included. The vibrational modes together with the symmetry of the corresponding displacement potential $W^{\lambda}(\mathbf{r})$ is shown in the inset. Frequencies (in meV) of the captured hydrogen molecule for Pt: $\omega_{M1} = 190$, $\omega_{M2} = 171$, $\omega_{M3} = 64$, $\omega_{M4} = 30$ and for Au: $\omega_{M1} = 249$, $\omega_{M2} = 141$, $\omega_{M3} = 84$, $\omega_{M4} = 37$. From Paper V.

found that the transverse modes lead to increases in the dI/dV curves. This indicates that the observed trends are rather insensitive to the basis set.

We point out that our dI/dV curves of the Pt-H_2-Pt contact are not in contradiction with the ones reported by the group of Sanvito in Refs. [87, 96] as they only consider the longitudenal modes. Chen in Ref. [177] find that the transverse modes have insignificant inelastic effects, we speculate if this could be due to the jellium model used for the Pt electrodes. For the Au-H_2-Au junction Frederiksen *et al.* in Ref. [175] conclude in compliance with our results that due to the symmetry of the states around the Fermi energy only the longitudinal modes contributes significantly to the inelastic signal.

In order to gain more insight into the nature of the observed steps in the dI/dV curves we make use of the simplified description of the scattering process presented in Sec. 3.3.2. From Eq. (3.20) it follows that the change in conductance due to the inelastic scattering with some mode λ involves all pairs of channels for which the matrix element $\langle\psi_{Lp}|W^{\lambda}(\mathbf{r})|\psi_{Rq}\rangle$ is non-zero. Since $W^{\lambda}(\mathbf{r})$ extends to the metal atoms binding to H_2, any scattering state at the Fermi level – transmitting or not – with weight on these atoms will contribute in Eq. (3.20).

In the case of Pt, we find at the Fermi level two types of eigenchannels with sufficient weight on hydrogen atoms and the contacting Pt atoms so that the coupling matrix element will be significant. One eigenchannel is the almost fully open s-channel (see inset of Fig. 7.18(a)) and the others have d-character and very low transmission around ε_F. Since the Au d-states have almost no weight at the Fermi level (see Fig. 7.18(b)) only the s-channel makes a contribution in Eq. (3.20).

For the longitudinal modes (M1 and M2) the symmetry of W^{λ} implies that s-s transitions are possible, but not s-d transitions (d-d transitions are not excluded by symmetry, but because of the vanishing overlap between ψ_{Ld} and ψ_{Rd}). Since $\mathcal{R}_s - \mathcal{T}_s \approx -1$ we should expect a drop in conductance in agreement with the NEGF-DFT calculations. At the hydrogen molecule, the s channel has mainly the character of the H_2 anti-bonding orbital (see the insets in Fig. 7.18). This implies that the product $\psi_{Ls}(r)^*\psi_{Rs}(\mathbf{r})$ is unchanged upon reflection in the plane cutting through the H-H bond perpendicular to the molecular axis. On the other hand the potential $W^{M2}(\mathbf{r})$ changes sign upon this reflection, and this explains the weak signal observed for M2 as compared to M1.

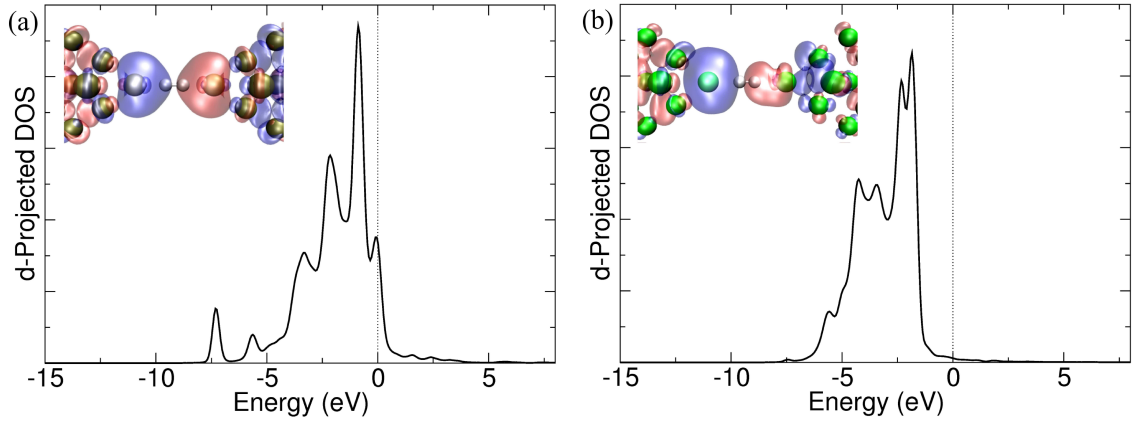

Figure 7.18: (a) The density of states projected onto the five d-orbitals for one of the platinum tip atoms. The almost fully conducting scattering channel is shown in the inset. (b) The d-DOS for one of the gold tip atoms. In the inset we show the s-symmetric scattering channel which carries almost 100% of the current.

The spatial shape of the d-states implies that coupling to the s-channel is possible only via the transverse modes M3 and M4 (see the symmetry of W^{λ} in the insets of Fig.

7.17). Limiting the sums in Eq. (3.20) to these two relevant states we see that ΔG becomes proportional to $\mathcal{R}_d - \mathcal{T}_s$. The increase in conductance found for the transverse modes in the Pt contact can thus be explained by a higher reflection probability of the low-transmitting d-channel as compared to the transmission probability of the high-transmitting s-channel. We stress that small changes in the transmission probabilities for the s- or d-channels could change the sign of ΔG. The symmetry of the displacement potential (W^λ) for the transverse modes prevents coupling between two states with s-symmetry, which explains why the transverse modes do not affect the conductance of the Au junction.

We notice that the calculated increase in conductance due to the transverse modes is not in agreement with the experimental data from inelastic point contact spectroscopy for Pt-H_2-Pt junctions which show a conductance decrease. Some of the possible explanations for this disagreement are:

(i) According to Eq. (3.20), the size (and the sign) of ΔG is determined by the relative magnitude of the s- and d-channel transmissions which are sensitive to the electronic density of states. Even very small changes here, e.g. from hydrogen atoms strongly bound to the platinum electrodes, could easily change the sign of ΔG. In this sense, the fact that we obtain an increase in the conductance while experimentally a decrease is observed, should be viewed as a quantitative rather than qualitative difference.

(ii) In principle the 1BA applies in the limit of weak electron-phonon interactions while we obtain electron-phonon matrix elements (3.11) on the order of electron volts. On the other hand the inelastic features in the dI/dV are a few percentage of G_0 indicating that only a few percentage out of a hundred electrons are scattered. Moreover, previous studies applying the 1BA to gold chains agrees nicely with experiments [27], indicating that the 1BA provides an accurate description of electron-phonon interactions in strongly coupled metal-molecule-metal junctions.

(iii) The highly symmetric geometry of the metal-H_2-metal junction used in this study is an idealized but oversimplified model of the real structure. However, we have considered other less symmetric configurations none of which gave rise to a conductance decrease for the transverse modes.

(iv) Inclusion of a finite phonon temperature could affect the calculated properties. However, as can be seen from Eq. (14) of Ref. [178] to lowest order in the electron-phonon strength the sign of ΔG cannot change by including heating.

Despite of the differences between the experimental and theoretical findings for the phonon-induced features in the dI/dV, we hesitate to conclude that the linear bridge configuration is not the structure observed in the experiments. The reason is the strong evidence mentioned in the previous sections which favors the linear bridge combined with the small size and high sensitivity of the inelastic features. We speculate if atomic hydrogen adsorbed at the platinum electrodes, although not expected to change the elastic behavior substantially, could change the inelastic signal from an increase to the experimentally observed decrease.

7.3.1 Summary

For both metals, the longitudinal vibrations of the H_2 leads to a decrease of the conductance at bias voltage corresponding to the frequency of the vibration, $eV = \hbar\omega$. In the case

of Pt electrodes, the transverse vibrations induce an increase in conductance. This might seem surprising since the hydrogen junction supports a single almost fully open transport channel and thus, according to the one-channel model, inelastic scattering should always lower the conductance. On the basis of scattering theory we showed that the increase is a result of non-transmitting d-channels which couple to the transmitting s-channel via the transverse modes. This is consistent with the finding that transverse modes do not affect the conductance in the case of Au electrodes.

Bibliography

[1] B. Hammer, L. B. Hansen, and J. K. Nørskov. Improved adsorption energetics within density-functional theory using revised perdew-burke-ernzerhof functionals. *Phys. Rev. B*, 59(11):7413, 1999.

[2] S.R. Bahn and K.W. Jacobsen. An object-oriented scripting interface to a legacy electronicstructure code. *Comput. Sci. Eng.*, 4(3):56, 2002.

[3] K.S. Thygesen, L.B. Hansen, and K.W. Jacobsen. Partly Occupied Wannier Functions. *Phys. Rev. Lett.*, 94(2):26405, 2005.

[4] J.M. Soler, E. Artacho, J.D. Gale, AI Garcia, J. Junquera, P. Ordejon, and D. Sánchez-Portal. The SIESTA method for ab initio order-N materials simulation. *J. Phys.: Condens. Matter*, 14(11):2745, 2002.

[5] E. Artacho, D. Sánchez-Portal, P. Ordejón, A. García, and J.M. Soler. *Phys. Status Solidi B*, 215:809, 1999.

[6] S.Y. Quek, L. Venkataraman, H.J. Choi, S.G. Louie, M.S. Hybertsen, and J.B. Neaton. Amine-gold linked single-molecule junctions: Experiment and theory. *Nano Lett.*, 7(11):3477, 2007.

[7] R.H.M. Smit, Y. Noat, C. Untiedt, N.D. Lang, M. van Hemert, and J.M. van Ruitenbeek. Measurement of the conductance of a hydrogen molecule. *Nature*, 419:906, 2002.

[8] D. Djukic, K. S. Thygesen, C. Untiedt, R. H. M. Smit, K. W. Jacobsen, and J. M. van Ruitenbeek. Stretching dependence of the vibration modes of a single-molecule pt-h_2-pt bridge. *Phys. Rev. B*, 71(16):161402, 2005.

[9] D. Djukic and J.M. van Ruitenbeek. Shot noise measurements on a single molecule. *Nano Lett.*, 6(4):789, 2006.

[10] K.S. Thygesen and K.W. Jacobsen. Conduction mechanism in a molecular hydrogen contact. *Phys. Rev. Lett.*, 94(3):036807, 2005.

[11] G.E. Moore. Cramming more components onto integrated circuits. *Electronics*, 38(8), 1965.

[12] C. Joachim, J.K. Gimzewski, and A. Aviram. Electronics using hybrid-molecular and mono-molecular devices. *Nature*, 408(6812):541, 2000.

[13] A. Aviram and M.A. Ratner. Molecular rectifiers. *Chem. Phys. Lett.*, 29(2):277, 1974.

[14] N. Agraït, A.L. Yeyati, and J.M. van Ruitenbeek. Quantum properties of atomic-sized conductors. *Phys. Rep*, 377:81, 2003.

[15] B. Xu and N.J. Tao. Measurement of single-molecule resistance by repeated formation of molecular junctions. *Science*, 301(5637):1221, 2003.

[16] D.M. Eigler, C.P. Lutz, and W.E. Rudge. An atomic switch realized with the scanning tunnelling microscope. *Nature*, 352(6336):600, 1991.

[17] M.A. Reed, C. Zhou, C.J. Muller, T.P. Burgin, and J.M. Tour. Conductance of a molecular junction. *Science*, 278(5336):252, 1997.

[18] J. Reichert, R. Ochs, D. Beckmann, H.B. Weber, M. Mayor, and H. Löhneysen. Driving current through single organic molecules. *Phys. Rev. Lett.*, 88(17):176804, 2002.

[19] K.S. Thygesen and K.W. Jacobsen. Molecular transport calculations with Wannier functions. *Chem. Phys.*, 319(1-3):111, 2005.

[20] M. Brandbyge, J.L. Mozos, P. Ordejon, J. Taylor, and K. Stokbro. Density-functional method for nonequilibrium electron transport. *Phys. Rev. B*, 65(16):165401, 2002.

[21] Y. Xue, S. Datta, and M.A. Ratner. First-principles based matrix Green's function approach to molecular electronic devices: general formalism. *Chem. Phys.*, 281(2-3):151, 2002.

[22] J.J. Palacios, A.J. Perez-Jimenez, E. Louis, E. SanFabian, and J.A. Verges. First-principles approach to electrical transport in atomic-scale nanostructures. *Phys. Rev. B*, 66(3):35322, 2002.

[23] F. Evers, F. Weigend, and M. Koentopp. Conductance of molecular wires and transport calculations based on density-functional theory. *Phys. Rev. B*, 69(23):235411, 2004.

[24] F. Evers and K. Burke. Pride, prejudice, and penury of ab initio transport calculations for single molecules. In *CRC Handbook on Molecular and Nanoelectronics, ed. S. Lyshevski*. CRC Press, 2007.

[25] M. Koentopp, C. Chang, K. Burke, and R. Car. Density functional calculations of nanoscale conductance. *J. Phys.: Condens. Matter*, 20(8):83203, 2008.

[26] V. M. García-Suárez, A. R. Rocha, S. W. Bailey, C. J. Lambert, S. Sanvito, and J. Ferrer. Conductance oscillations in zigzag platinum chains. *Phys. Rev. Lett.*, 95(25):256804, 2005.

[27] T. Frederiksen, M. Brandbyge, N. Lorente, and A.P. Jauho. Inelastic scattering and local heating in atomic gold wires. *Phys. Rev. Lett.*, 93(25):256601, 2004.

[28] M. Strange, K.S. Thygesen, J.P. Sethna, and K.W. Jacobsen. Anomalous Conductance Oscillations and Half-Metallicity in Atomic Ag-O Chains. *Phys. Rev. Lett.*, 101(9):96804, 2008.

[29] K. Stokbro, J. Taylor, M. Brandbyge, J.L. Mozos, and P. Ordejon. Theoretical study of the nonlinear conductance of Di-thiol benzene coupled to Au (111) surfaces via thiol and thiolate bonds. *Comput. Mater. Sci.*, 27(1-2):151, 2003.

[30] M. Di Ventra, S.T. Pantelides, and N.D. Lang. First-principles calculation of transport properties of a molecular device. *Phys. Rev. Lett.*, 84(5):979, 2000.

[31] J.C. Cuevas, J. Heurich, F. Pauly, W. Wenzel, and G. Schon. Theoretical description of the electrical conduction in atomic and molecular junctions. *Nanotechnology*, 14(8):29, 2003.

[32] Y. García, J. J. Palacios, E. SanFabián, J. A. Vergés, A. J. Pérez-Jiménez, and E. Louis. Electronic transport and vibrational modes in a small molecular bridge: H_2 in pt nanocontacts. *Phys. Rev. B*, 69(4):041402, 2004.

[33] M.L. Born and R. Oppenheimer. Zur Quantentheorie der Moleküln. *Ann. Phys.*, 84:457, 1927.

[34] W. Koch and M.C. Holthausen. *A Chemist's Guide to Density Functional Theory.* Wiley-Vch Weinheim, 2000.

[35] R.M. Dreizler and E.K.U. Gross. *Density functional theory: an approach to the quantum many-body problem.* Springer-Verlag Berlin, 1990.

[36] R.G. Parr and W. Yang. *Density-Functional Theory of Atoms and Molecules.* Oxford University Press, 1989.

[37] P. Hohenberg and W. Kohn. Inhomogeneous electron gas. *Phys. Rev*, 136(3B):B864, 1964.

[38] M. Levy. Electron densities in search of Hamiltonians. *Phys. Rev. A*, 26(3):1200, 1982.

[39] E.H. Lieb. Density functionals for Coulomb systems. *Int. J. Quantum Chem.*, 24:243, 1983.

[40] W. Kohn and L.J. Sham. Self-consistent equations including exchange and correlation effects. *Phys. Rev.*, 140(4A):A1133, 1965.

[41] W. Pauli. Über den Zusammenhang des Abschlusses der Elektronengruppen im Atom mit der Komplexstruktur der Spektren. *Z. Physik*, 31(1):765, 1925.

[42] J.P. Perdew, S. Kurth, A. Zupan, and P. Blaha. Accurate density functional with correct formal properties: A step beyond the generalized gradient approximation. *Phys. Rev. Lett.*, 82(12):2544, 1999.

[43] J.P. Perdew and K. Burke. Comparison shopping for a gradient-corrected density functional. *Int. J. Quant. Chem.*, 57(3):309, 1996.

[44] P.A.M. Dirac. Note on exchange phenomena in the Thomas atom. *Proc. Cambridge Phil. Soc.*, 26:376, 1930.

[45] S.H. Vosko, L. Wilk, and M. Nusair. Accurate spin-dependent electron liquid correlation energies for local spin density calculations: a critical analysis. *Can. J. Phys.*, 58(8):1200, 1980.

[46] J.P. Perdew and A. Zunger. Self-interaction correction to density-functional approximations for many-electron systems. *Phys. Rev. B*, 23(10):5048, 1981.

[47] J.P. Perdew and Y. Wang. Accurate and simple analytic representation of the electron-gas correlation energy. *Phys. Rev. B*, 45(23):13244, 1992.

[48] D.M. Ceperley and B.J. Alder. Ground state of the electron gas by a stochastic method. *Phys. Rev. Lett.*, 45(7):566, 1980.

[49] J.P. Perdew, J.A. Chevary, S.H. Vosko, K.A. Jackson, M.R. Pederson, D.J. Singh, and C. Fiolhais. Atoms, molecules, solids, and surfaces: Applications of the generalized gradient approximation for exchange and correlation. *Phys. Rev. B*, 46(11):6671, 1992.

[50] J.P. Perdew, K. Burke, and M. Ernzerhof. Generalized gradient approximation made simple. *Phys. Rev. Lett.*, 77(18):3865, 1996.

[51] Y. Zhang and W. Yang. Comment on Generalized gradient approximation made simple. *Phys. Rev. Lett.*, 80(4):890, 1998.

[52] J.P. Perdew. Unified theory of exchange and correlation beyond the local density approximation. In Esching H. Ziesche P, editor, *Electronic Structure of Solids' 91*. Berlin: Akademic Verlag, 1991.

[53] D. Vanderbilt. Soft self-consistent pseudopotentials in a generalized eigenvalue formalism. *Phys. Rev. B*, 41(11):7892, 1990.

[54] N. Troullier and J.L. Martins. A straightforward method for generating soft transferable pseudopotentials. *Solid State Commun.*, 74:613, 1990.

[55] M.C. Payne, M.P. Teter, D.C. Allan, T.A. Arias, and J.D. Joannopoulos. Iterative minimization techniques for ab initio total-energy calculations: molecular dynamics and conjugate gradients. *Rev. Mod. Phys.*, 64(4):1045, 1992.

[56] G. Kresse and J. Furthmuller. Efficiency of ab-initio total energy calculations for metals and semiconductors using a plane-wave basis set. *Comp. Mat. Sci.*, 6(1):15, 1996.

[57] N.W. Ashcroft and N.D. Mermin. Solid State Physics. 1976. *Saunders College, Philadelphia*, 1976.

[58] H.J. Monkhorst and J.D. Pack. Special points for Brillouin-zone integrations. *Phys. Rev. B*, 13(12):5188, 1976.

[59] D.J. Chadi and M.L. Cohen. Special points in the Brillouin zone. *Phys. Rev. B*, 8(12):5747, 1973.

[60] K.S. Thygesen, L.B. Hansen, and K.W. Jacobsen. Partly occupied Wannier functions: Construction and applications. *Phys. Rev. B*, 72(12):125119, 2005.

[61] N. Marzari and D. Vanderbilt. Maximally localized generalized Wannier functions for composite energy bands. *Phys. Rev. B*, 56(20):12847, 1997.

[62] O.F. Sankey and D.J. Niklewski. Ab initio multicenter tight-binding model for molecular-dynamics simulations and other applications in covalent systems. *Phys. Rev. B*, 40(6):3979, 1989.

[63] H. Jonsson, G. Mills, and K.W. Jacobsen. Nudged elastic band method for finding minimum energy paths of transitions. In *Classical and Quantum Dynamics in Condensed Phase Systems*. World Scientific, 1998.

[64] G. Henkelman and H. Jónsson. Improved tangent estimate in the nudged elastic band method for finding minimum energy paths and saddle points. *J. Chem. Phys.*, 113:9978, 2000.

[65] G. Henkelman, B.P. Uberuaga, and H. Jónsson. A climbing image nudged elastic band method for finding saddle points and minimum energy paths. *J. Chem. Phys.*, 113:9901, 2000.

[66] M. Di Ventra and N.D. Lang. Transport in nanoscale conductors from first principles. *Phys. Rev. B*, 65(4):45402, 2001.

[67] E.G. Emberly and G. Kirczenow. Theoretical study of electrical conduction through a molecule connected to metallic nanocontacts. *Phys. Rev. B*, 58(16):10911, 1998.

[68] E.G. Emberly and G. Kirczenow. Landauer theory, inelastic scattering, and electron transport in molecular wires. *Phys. Rev. B*, 61(8):5740, 2000.

[69] J. Bonča and SA Trugman. Effect of inelastic processes on tunneling. *Phys. Rev. Lett.*, 75(13):2566, 1995.

[70] Thomas Frederiksen, Magnus Paulsson, Mads Brandbyge, and Antti-Pekka Jauho. Inelastic transport theory from first principles: Methodology and application to nanoscale devices. *Phys. Rev. B*, 75(20):205413, 2007.

[71] A. Pecchia, A. Di Carlo, A. Gagliardi, S. Sanna, T. Frauenheim, and R. Gutierrez. Incoherent electron-phonon scattering in octanethiols. *Nano Lett.*, 4(11):2109, 2004.

[72] M. Galperin, M.A. Ratner, and A. Nitzan. Molecular transport junctions: vibrational effects. *J. Phys.: Condens. Matter*, 19(10):103201, 2007.

[73] Magnus Paulsson and Mads Brandbyge. Transmission eigenchannels from nonequilibrium green's functions. *Phys. Rev. B*, 76(11):115117, 2007.

[74] Yigal Meir and Ned S. Wingreen. Landauer formula for the current through an interacting electron region. *Phys. Rev. Lett.*, 68(16):2512, 1992.

[75] D.C. Langreth. *Linear and Nonlinear Electron Transport in Solids*. Plenum Press, New York, 1976.

[76] H. Haug and A.P. Jauho. *Quantum kinetics in transport and optics of semiconductors*. Springer-Verlag, 1998.

[77] M. Büttiker, Y. Imry, R. Landauer, and S. Pinhas. Generalized many-channel conductance formula with application to small rings. *Phys. Rev. B*, 31(10):6207, 1985.

[78] D.S. Fisher and P.A. Lee. Relation between conductivity and transmission matrix. *Phys. Rev. B*, 23(12):6851, 1981.

[79] M. Büttiker. Coherent and sequential tunneling in series barriers. *IBM J. Res. Dev.*, 32(1):63, 1988.

[80] M. Brandbyge, M.R. Sorensen, and K.W. Jacobsen. Conductance eigenchannels in nanocontacts. *Phys. rev. B*, 56(23):14956, 1997.

[81] J. M. C. Rauba, M. Strange, and K. S. Thygesen. Quantum conductance of 4,4-bipyridine molecular junctions: Role of electrode work function and local d band. *Phys. Rev. B*, 78(16):165116, 2008.

[82] D.M. Newns. Self-consistent model of hydrogen chemisorption. *Phys. Rev.*, 178(3):1123, 1969.

[83] G.D. Mahan. *Many-particle physics*. Plenum Publishing Corporation, 1990.

[84] H. Bruus and K. Flensberg. *Many-body quantum theory in condensed matter physics: An introduction*. Oxford University Press, 2004.

[85] G. Rickayzen. *Green's functions and condensed matter*. Academic Press London, 1980.

[86] M. Paulsson, T. Frederiksen, and M. Brandbyge. Modeling inelastic phonon scattering in atomic-and molecular-wire junctions. *Phys. Rev. B*, 72(20):201101, 2005.

[87] W. Lee, N. Jean, and S. Sanvito. Exploring the limits of the self-consistent Born approximation for inelastic electronic transport. *Phys. Rev. B*, 79(8):85120, 2009.

[88] A. Gagliardi, G.C. Solomon, A. Pecchia, T. Frauenheim, A. Di Carlo, N.S. Hush, and J.R. Reimers. A priori method for propensity rules for inelastic electron tunneling spectroscopy of single-molecule conduction. *Phys. Rev. B*, 75(17):174306, 2007.

[89] P. Hyldgaard, S. Hershfield, J.H. Davies, and J.W. Wilkins. Resonant tunneling with an electron-phonon interaction. *Ann. Phys.*, 236(1):1, 1994.

[90] T. Frederiksen. Inelastic electron transport in nanosystems. Master's thesis, Department of Micro and Nanotechnology, Technical University of Denmark, 2004.

[91] I. Kristensen. Electrontransport i vibrerende nanostrukturer. Master's thesis, Center for Atomic-scale Materials Physics, Technical University of Denmark, 2005.

[92] L. de La Vega, A. Martin-Rodero, N. Agrait, and A.L. Yeyati. Universal features of electron-phonon interactions in atomic wires. *Phys. Rev. B*, 73(7):75428, 2006.

[93] J.K. Viljas, J.C. Cuevas, F. Pauly, and M. Häfner. Electron-vibration interaction in transport through atomic gold wires. *Phys. Rev. B*, 72(24):245415, 2005.

[94] J.R. Taylor. *Scattering theory: The quantum theory of nonrelativistic collisions*. Dover Publications, Inc., 2006.

[95] E. Leslie. *Ballentine, Quantum mechanics: A modern development*. World Scientific, 1998.

[96] N. Jean and S. Sanvito. Inelastic transport in molecular spin valves: Calculations using the tight-binding Su-Schrieffer-Heeger model. *Phys. Rev. B*, 73(9):94433, 2006.

[97] Y. Imry, O. Entin-Wohlman, and A. Aharony. Landauer transport with inelastic scattering. *Europhys. Lett.*, 72(2):263, 2005.

[98] O. Tal, M. Krieger, B. Leerink, and J.M. van Ruitenbeek. Electron-Vibration Interaction in Single-Molecule Junctions: From Contact to Tunneling Regimes. *Phys. Rev. Lett.*, 100(19):196804, 2008.

[99] T. Frederiksen. *Inelastic transport theory for nanoscale systems*. PhD thesis, Department of Micro and Nanotechnology, Technical University of Denmark, 2007.

[100] R. Egger and A.O. Gogolin. Vibration-induced correction to the current through a single molecule. *Phys. Rev. B*, 77(11):113405, 2008.

[101] M. Strange, K.S. Thygesen, and K. W. Jacobsen. Electron transport in a pt-co-pt nanocontact: Density functional theory calculations. *Phys. Rev. B*, 73(12):125424, 2006.

[102] P. Delaney and J.C. Greer. Correlated electron transport in molecular electronics. *Phys. Rev. Lett.*, 93(3):36805, 2004.

[103] P. Darancet, A. Ferretti, D. Mayou, and V. Olevano. Ab initio GW electron-electron interaction effects in quantum transport. *Phys. Rev. B*, 75(7):75102, 2007.

[104] K.S. Thygesen and A. Rubio. Nonequilibrium GW approach to quantum transport in nano-scale contacts. *J. Chem. Phys.*, 126:091101, 2007.

[105] S. Kurth, G. Stefanucci, C.O. Almbladh, A. Rubio, and E.K.U. Gross. Time-dependent quantum transport: A practical scheme using density functional theory. *Phys. Rev. B*, 72(3):35308, 2005.

[106] P. Bokes and R.W. Godby. Conductance and polarization in quantum junctions. *Phys. Rev. B*, 69(24):245420, 2004.

[107] F. Guinea, C. Tejedor, F. Flores, and E. Louis. Effective two-dimensional Hamiltonian at surfaces. *Phys. Rev. B*, 28(8):4397, 1983.

[108] M. Brandbyge, N. Kobayashi, and M. Tsukada. Conduction channels at finite bias in single-atom gold contacts. *Phys. Rev. B*, 60(24):17064, 1999.

[109] M. Head-Gordon and J.C. Tully. Vibrational relaxation on metal surfaces: Molecular-orbital theory and application to CO/Cu (100). *J. Chem. Phys.*, 96:3939, 1992.

[110] K.S. Thygesen. Electron transport through an interacting region: The case of a nonorthogonal basis set. *Phys. Rev. B*, 73(3):35309, 2006.

[111] K.S. Thygesen and K.W. Jacobsen. Interference and k-point sampling in the supercell approach to phase-coherent transport. *Phys. Rev. B*, 72(3):33401, 2005.

[112] A. Nitzan and M.A. Ratner. Electron transport in molecular wire junctions. *Science*, 300(5624):1384, 2003.

[113] K. Varga and S.T. Pantelides. Quantum Transport in Molecules and Nanotube Devices. *Phys. Rev. Lett.*, 98(7):76804, 2007.

[114] D.Q. Andrews, R. Cohen, R.P. Van Duyne, and M.A. Ratner. Single molecule electron transport junctions: Charging and geometric effects on conductance. *J. Chem. Phys.*, 125:174718, 2006.

[115] S.V. Faleev, F. Léonard, D.A. Stewart, and M. van Schilfgaarde. Ab initio tight-binding LMTO method for nonequilibrium electron transport in nanosystems. *Phys. Rev. B*, 71(19):195422, 2005.

[116] J. Tomfohr and O.F. Sankey. Theoretical analysis of electron transport through organic molecules. *J. Chem. Phys.*, 120:1542, 2004.

[117] M. Strange. *Structure and transport properties of atomic chains and molecules*. PhD thesis, Center for Atomic-scale Materials Design, Technical University of Denmark, 2008.

[118] V.M. García-Suárez, A.R. Rocha, S.W. Bailey, C.J. Lambert, S. Sanvito, and J. Ferrer. Single-channel conductance of H_2 molecules attached to platinum or palladium electrodes. *Phys. Rev. B*, 72(4):45437, 2005.

[119] J. Fernández-Rossier, D. Jacob, C. Untiedt, and J.J. Palacios. Transport in magnetically ordered Pt nanocontacts. *Phys. Rev. B*, 72(22):224418, 2005.

[120] M. Tsutsui, Y. Teramae, S. Kurokawa, and A. Sakai. High-conductance states of single benzenedithiol molecules. *Appl. Phys. Lett.*, 89:163111, 2006.

[121] X. Xiao, B. Xu, and N.J. Tao. Measurement of single molecule conductance: Benzenedithiol and benzenedimethanethiol. *Nano Lett.*, 4(2):267, 2004.

[122] J. Ulrich, D. Esrail, W. Pontius, L. Venkataraman, D. Millar, and L.H. Doerrers. Variability of conductance in molecular junctions. *J. Phys. Chem. B*, 110(6):2462, 2006.

[123] S. Ghosh, H. Halimun, A.K. Mahapatro, J. Choi, S. Lodha, and D. Janes. Device structure for electronic transport through individual molecules using nanoelectrodes. *Appl. Phys. Lett.*, 87:233509, 2005.

[124] H. Kondo, H. Kino, J. Nara, T. Ozaki, and T. Ohno. Contact-structure dependence of transport properties of a single organic molecule between Au electrodes. *Phys. Rev. B*, 73(23):235323, 2006.

[125] E.G. Emberly and G. Kirczenow. The smallest molecular switch. *Phys. Rev. Lett.*, 91(18):188301, 2003.

[126] Y. Xue, S. Datta, and M.A. Ratner. Charge transfer and band lineup in molecular electronic devices: a chemical and numerical interpretation. *J. Chem. Phys.*, 115:4292, 2001.

[127] S.H. Ke, H.U. Baranger, and W. Yang. Electron transport through single conjugated organic molecules: Basis set effects in ab initio calculations. *J. Chem. Phys.*, 127:144107, 2007.

[128] R. Stadler, K.S. Thygesen, and K.W. Jacobsen. Forces and conductances in a single-molecule bipyridine junction. *Phys. Rev. B*, 72(24):241401, 2005.

[129] I.S. Kristensen, D.J. Mowbray, K.S. Thygesen, and K.W. Jacobsen. Comparative study of anchoring groups for molecular electronics: structure and conductance of Au-S-Au and Au-NH_2-Au junctions. *J. Phys.: Condens. Matter*, 20(37):374101, 2008.

[130] R. Stadler and K.W. Jacobsen. Fermi level alignment in molecular nanojunctions and its relation to charge transfer. *Phys. Rev. B*, 74(16):161405, 2006.

[131] S. Hou, J. Ning, Z. Shen, X. Zhao, and Z. Xue. Influences of the molecule-electrode interface structure on the conducting characteristics of the gold-4, 4 bipyridine-gold molecular junction. *Chem. Phys.*, 327(1):1, 2006.

[132] X. Wu, Q. Li, J. Huang, and J. Yang. Nonequilibrium electronic transport of 4, 4-bipyridine molecular junction. *J. Chem. Phys.*, 123:184712, 2005.

[133] Q. Li, X. Wu, J. Huang, and J. Yang. Electronic transport property of 4,-bipyridine molecular junction. *Ultramicroscopy*, 105(1-4):293, 2005.

[134] T. Tada, M. Kondo, and K. Yoshizawa. Greens function formalism coupled with Gaussian broadening of discrete states for quantum transport: Application to atomic and molecular wires. *J. Chem. Phys.*, 121:8050, 2004.

[135] S. Hou, J. Zhang, R. Li, J. Ning, R. Han, Z. Shen, X. Zhao, Z. Xue, and Q. Wu. First-principles calculation of the conductance of a single 4, 4 bipyridine molecule. *Nanotechnology*, 16(2):239, 2005.

[136] R. Li, S. Hou, J. Zhang, Z. Qian, Z. Shen, and X. Zhao. Analysis on the contribution of molecular orbitals to the conductance of molecular electronic devices. *J. Chem. Phys.*, 125:194113, 2006.

[137] A.J. Perez-Jimenez. Uncovering Transport Properties of 4, 4-Bipyridine/Gold Molecular Nanobridges. *J. Phys. Chem. B*, 109(20):10052, 2005.

[138] J. Ulrich, D. Esrail, W. Pontius, L. Venkataraman, D. Millar, and L.H. Doerrers. Variability of conductance in molecular junctions. *J. Phys. Chem. B*, 110(6):2462, 2006.

[139] X. Li, J. He, J. Hihath, B. Xu, S.M. Lindsay, and N. Tao. Conductance of single alkanedithiols: Conduction mechanism and effect of molecule-electrode contacts. *J. Am. Chem. Soc.*, 128:2135, 2006.

[140] E. Anglada, J.A. Torres, F. Yndurain, and J.M. Soler. Formation of Gold Nanowires with Impurities: A First-Principles Molecular Dynamics Simulation. *Phys. Rev. Lett.*, 98(9):96102, 2007.

[141] L. Venkataraman, J.E. Klare, I.W. Tam, C. Nuckolls, M.S. Hybertsen, and M.L. Steigerwald. Single-Molecule Circuits with Well-Defined Molecular Conductance. *Nano Lett.*, 6(3):458, 2006.

[142] L. Venkataraman, J.E. Klare, C. Nuckolls, M.S. Hybertsen, and M.L. Steigerwald. Dependence of single-molecule junction conductance on molecular conformation. *Nature*, 442(7105):904, 2006.

[143] S. Kubatkin, A. Danilov, M. Hjort, J. Cornil, J.L. Brédas, N. Stuhr-Hansen, P. Hedegård, and T. Bjørnholm. Single-electron transistor of a single organic molecule with access to several redox states. *Nature*, 425(6959):698, 2003.

[144] G. Cuniberti, G. Fagas, and K. Richter. *Introducing Molecular Electronics*. Springer, 2005.

[145] N. Lorente, M. Persson, L.J. Lauhon, and W. Ho. Symmetry selection rules for vibrationally inelastic tunneling. *Phys. Rev. Lett.*, 86(12):2593, 2001.

[146] B.C. Stipe, M.A. Rezaei, and W. Ho. Localization of inelastic tunneling and the determination of atomic-scale structure with chemical specificity. *Phys. Rev. Lett.*, 82(8):1724–1727, 1999.

[147] S. Csonka, A. Halbritter, G. Mihaly, E. Jurdik, O.I. Shklyarevskii, S. Speller, and H. Van Kempen. Fractional conductance in hydrogen-embedded gold nanowires. *Phys. Rev. Lett.*, 90(11):116803, 2003.

[148] W.H.A. Thijssen. *Molecule-assisted atomic chain formation: mechanisms and properties of new one-dimensional conductors*. PhD thesis, Department of Atomic and Molecular Conductors, Leiden Institute of Physics, Faculty of Science, Leiden University, 2007.

[149] S. Csonka, A. Halbritter, G. Mihaly, O.I. Shklyarevskii, S. Speller, and H. van Kempen. Conductance of Pd-H nanojunctions. *Phys. Rev. Lett.*, 93(1):16802, 2004.

[150] P. Makk, S. Csonka, and A. Halbritter. Effect of hydrogen molecules on the electronic transport through atomic-sized metallic junctions in the superconducting state. *Phys. Rev. B*, 78(4):45414, 2008.

[151] J. Moreland and J.W. Ekin. Electron tunneling experiments using Nb-Sn breakjunctions. *J. Appl. Phys.*, 58:3888, 1985.

[152] C.J. Muller, J.M. Van Ruitenbeek, and L.J. De Jongh. Experimental observation of the transition from weak link to tunnel junction. *Physica C*, 191:485, 1992.

[153] S. K. Nielsen, Y. Noat, M. Brandbyge, R. H. M. Smit, K. Hansen, L. Y. Chen, A. I. Yanson, F. Besenbacher, and J. M. van Ruitenbeek. Conductance of single-atom platinum contacts: Voltage dependence of the conductance histogram. *Phys. Rev. B*, 67(24):245411, 2003.

[154] M. Kiguchi, R. Stadler, I.S. Kristensen, D. Djukic, and J.M. Van Ruitenbeek. Evidence for a single hydrogen molecule connected by an atomic chain. *Phys. Rev. Lett.*, 98(14):146802, 2007.

[155] B. Ludoph, M. H. Devoret, D. Esteve, C. Urbina, and J. M. van Ruitenbeek. Evidence for saturation of channel transmission from conductance fluctuations in atomic-size point contacts. *Phys. Rev. Lett.*, 82(7):1530, 1999.

[156] B. Ludoph and J. M van Ruitenbeek. Conductance fluctuations as a tool for investigating the quantum modes in atomic-size metallic contacts. *Phys. Rev. B*, 61(3):2273, 2000.

[157] M. Reznikov, M. Heiblum, H. Shtrikman, and D. Mahalu. Temporal correlation of electrons: suppression of shot noise in a ballistic quantum point contact. *Phys. Rev. Lett.*, 75(18):3340, 1995.

[158] H.E. Van den Brom and J.M. Van Ruitenbeek. Quantum suppression of shot noise in atom-size metallic contacts. *Phys. Rev. Lett.*, 82(7):1526, 1999.

[159] E. Scheer, N. Agraït, J.C. Cuevas, A.L. Yeyati, B. Ludoph, A. Martin-Rodero, G.R. Bollinger, J.M. van Ruitenbeek, and C. Urbina. The signature of chemical valence in the electrical conduction through a single-atom contact. *Nature*, 394(6689):154, 1998.

[160] W. H. A. Thijssen, D. Djukic, A. F. Otte, R. H. Bremmer, and J. M. van Ruitenbeek. Vibrationally induced two-level systems in single-molecule junctions. *Phys. Rev. Lett.*, 97(22):226806, 2006.

[161] A.V. Khotkevich and I.K. Yanson. *Atlas of Point Contact Spectra of Electron-Phonon Interaction in Metals*. Kluwer Academic, Dordrect, 1995.

[162] K.S. Thygesen. *Structure and transport in nano-scale contacts*. PhD thesis, Center for Atomic-scale Materials Physics, Technical University of Denmark, 2005.

[163] B. Hammer and J. K. Nørskov. Electronic factors determining the reactivity of metal surfaces. *Surface Science*, 343(3):211, 1995.

[164] Pavel Jelínek, Rubén Pérez, José Ortega, and Fernando Flores. Hydrogen dissociation over au nanowires and the fractional conductance quantum. *Phys. Rev. Lett.*, 96(4):046803, 2006.

[165] Pavel Jelínek, Rubén Pérez, José Ortega, and Fernando Flores. Ab initio study of evolution of mechanical and transport properties of clean and contaminated au nanowires along the deformation path. *Phys. Rev. B*, 77(11):115447, 2008.

[166] A. T. Gee, B. E. Hayden, C. Mormiche, and T. S. Nunney. The role of steps in the dynamics of hydrogen dissociation on pt(533). *J. Chem. Phys.*, 112(17):7660, 2000.

[167] R. A. Olsen, D. A. McCormack, M. Luppi, and E. J. Baerends. Six-dimensional quantum dynamics of h_2 dissociative adsorption on the pt(211) stepped surface. *J. Chem. Phys.*, 128(19):194715, 2008.

[168] I. M. N. Groot, K. J. P. Schouten, A. W. Kleyn, and L. B. F. Juurlink. Dynamics of hydrogen dissociation on stepped platinum. *J. Chem. Phys.*, 129(22):224707, 2008.

[169] H. Falsig, B. Hvolbæk, I.S. Kristensen, T. Jiang, T. Bligaard, C.H. Christensen, and J.K. Nørskov. Trends in the Catalytic CO Oxidation Activity of Nanoparticles. *Angew. Chem. Intl. Edit.*, 47:4835, 2008.

[170] R.N. Barnett, H. Hakkinen, A.G. Scherbakov, and U. Landman. Hydrogen Welding and Hydrogen Switches in a Monoatomic Gold Nanowire. *Nano Lett.*, 4:1845, 2004.

[171] G. Rubio-Bollinger, S. R. Bahn, N. Agraït, K. W. Jacobsen, and S. Vieira. Mechanical properties and formation mechanisms of a wire of single gold atoms. *Phys. Rev. Lett.*, 87(2):026101, 2001.

[172] R. H. M. Smit, C. Untiedt, A. I. Yanson, and J. M. van Ruitenbeek. Common origin for surface reconstruction and the formation of chains of metal atoms. *Phys. Rev. Lett.*, 87(26):266102, 2001.

[173] R. H. M. Smit, C. Untiedt, G. Rubio-Bollinger, R. C. Segers, and J. M. van Ruitenbeek. Observation of a parity oscillation in the conductance of atomic wires. *Phys. Rev. Lett.*, 91(7):076805, 2003.

[174] N. Agrait, J.G. Rodrigo, and S. Vieira. Conductance steps and quantization in atomic-size contacts. *Phys. Rev. B*, 47(18):12345–12348, 1993.

[175] T. Frederiksen, M. Paulsson, and M. Brandbyge. Inelastic fingerprints of hydrogen contamination in atomic gold wire systems. *J. Phys.: Conf. Ser.*, 61:312, 2007.

[176] P.C. Rusu and G. Brocks. Work functions of self-assembled monolayers on metal surfaces by first-principles calculations. *Physical Review B*, 74(7):73414, 2006.

[177] Y.C. Chen. Effects of isotope substitution on local heating and inelastic current in hydrogen molecular junctions. *Phys. Rev. B*, 78(23):233310, 2008.

[178] M. Paulsson, T. Frederiksen, and M. Brandbyge. Phonon scattering in nanoscale systems: Lowest order expansion of the current and power expressions. *J. Phys.: Conf. Ser.*, 35:247, 2006.

[179] L.V. Keldysh. Diagram Technique for Nonequilibrium Processes. *Soviet Physics JETP-USSR*, 20(4):1018, 1965.

[180] J. Rammer and H. Smith. Quantum field-theoretical methods in transport theory of metals. *Rev. Mod. Phys.*, 58(2):323, 1986.

Appendix A

Non-Equilibrium Green Functions

In this appendix a short introduction to the Non-Equilibrium Green Functions (NEGF) formalism [179] is provided. NEGF is a technique which proves very powerful in describing non-equilibrium phenomena perturbatively. By introducing the contour-ordered Green's function (GF), which is the non-equilibrium analog to the casual GF in equilibrium theory, a perturbation expansion based on Wicks theorem can be deduced. The physical relevant real-time Green's functions, which is contained within the contour-ordered GF, can then be subtracted. From the real-time GFs properties of the many-particle system, such as the particle current in quantum transport, can be evaluated. A comprehensive review of the theory can be found in Refs. [76, 83, 180].

The non-equillibrium Hamiltonian is in its most general form given as,

$$H(t) = H^0 + H^i + H'(t),$$

where H^0 is the non-interacting (quadratic) Hamiltonian, H^i contains possible particle interactions and $H'(t)$ represents a disturbance to the system which vanishes at $t < t_0$. In quantum transport $H'(t)$ describes the coupling between subsystems having different chemical potentials and the electron-phonon interactions are contained within H^i in the special case of inelastic transport.

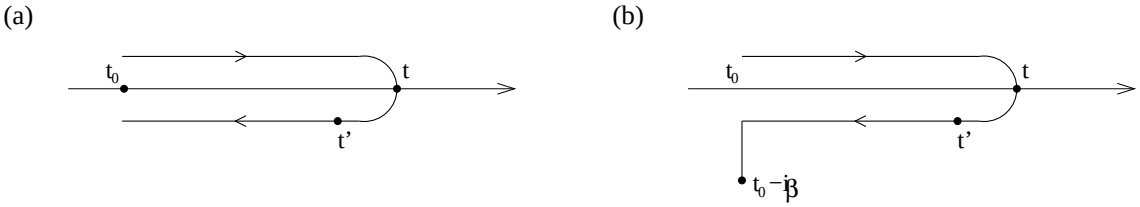

Figure A.1: (a) The contour C runs along the real axis and consist of an upper, C_1, and lower branch, C_2. (b) The contour C_v. C_v coincides with C in the steady state limit which is considered throughout this work.

The contour-ordered single-particle Green's function is defined as

$$G_{ij}(\tau, \tau') = -i\langle T_C[c_i(\tau)c_j^\dagger(\tau')]\rangle, \tag{A.1}$$

where T_C is the contour-ordering operator for the contour C depicted in Fig. A.1 and c_i, $c_j^\dagger$ are field operators in the Heisenberg picture. The expectation value is taken with respect to the equilibrium state operator describing the system for times $t < t_0$

$$\rho_{\text{eq}} = \frac{e^{-\beta(H_0+H_i-\mu N)}}{\text{Tr}[e^{-\beta(H_0+H_i-\mu N)}]},$$

where N is the number operator, μ is the chemical potential and $\beta = k_B T^{-1}$. This choice of state operator builds on the assumption that the thermodynamic degrees of freedom in the equilibrium system do not follow instantaneously the rapid variations contained in the time-dependent disturbance [76].

In quantum transport theory (see chapter 3) the state operator of the uncoupled system is a product of the respective equilibrium state operators of the three subsystems each characterized by their chemical potential

$$\rho_{\text{eq}} = \frac{1}{Z_0} e^{-\beta(H_L - \mu_L N_L)} e^{-\beta(H_R - \mu_R N_R)} e^{-\beta(H_C - \mu_C N_C)} \otimes \hat{W}_{ext}$$

where $\hat{W}_{ext}$ denotes the state of possible external degrees of freedom such as phonons and Z_0 is the partition function.

In the interaction picture with respect to H_0 the contour-ordered Green's function in Eq. (A.1) takes the form

$$G_{i,j}(\tau, \tau') = -i \frac{\langle T_C \big[\mathbf{S}'_C \mathbf{S}^i_{C_v} \hat{\psi}_i(\tau) \hat{\psi}^\dagger_j(\tau') \big] \rangle_0}{\langle T_C \big[\mathbf{S}'_C \mathbf{S}^i_{C_v} \big] \rangle_0}, \tag{A.2}$$

where

$$\mathbf{S}'_C = \exp\big[-i \int_C \mathrm{d}\tau \hat{H}'(\tau) \big]. \tag{A.3}$$

$$\mathbf{S}^i_{C_v} = \exp\big[-i \int_{C_v} \mathrm{d}\tau \hat{H}_i(\tau) \big]. \tag{A.4}$$

In these expressions "hat" refers to time-evolution with respect to the quadratic part of the Hamiltonian and $\langle \cdots \rangle_0$ to the fact that the expectation value is to be evaluated with respect to the non-interacting state operator. If particle interactions are turned on adiabatically the contours C and C_v (shown in Fig. A.1) will coincide when the system reaches steady state.

The contour-ordered Green's function contains four different real time GFs as special cases. For evaluation of physical quantities it is convenient to work with the lesser/greater and retarded/advanced GFs

$$\begin{aligned}
G^>_{i,j}(t,t') &= -i\langle \psi_i(t) \psi^\dagger_j(t') \rangle, \\
G^<_{i,j}(t,t') &= \pm i\langle \psi^\dagger_j(t') \psi_i(t) \rangle, \\
G^r_{i,j}(t,t') &= -i\theta(t-t')\langle \Big[\psi_i(t), \psi^\dagger_j(t') \Big]_\pm \rangle, \\
G^a_{i,j}(t,t') &= i\theta(t'-t)\langle \Big[\psi_i(t), \psi^\dagger_j(t') \Big]_\pm \rangle,
\end{aligned}$$

where the upper (lower) sign applies to fermions (bosons) and $[\cdots]_\pm$ denotes a anti-commutator (commutator). From the universal relation $G^r - G^a = G^> - G^<$ it follows that the four real time GFs are not independent. In steady state situations yet another relation between the GFs exists, $G^r = [G^a]^\dagger$. Consequently, in steady state one only need to consider two linearly independent Green's functions.

From Eq. (A.2) we notice that the only difference between equilibrium and non-equilibrium GF theory is the replacement of real-time integrals by contour integrals. As a consequence the contour-ordered Green's function obeys the same Dyson equation as the equilibrium counterpart

$$G_{i,j}(\tau, \tau') = G^0_{i,j}(\tau, \tau') + \sum_{k,l} \int G^0_{i,k}(\tau, \tau_1) \Sigma_{k,l}(\tau_1, \tau_2) G_{l,j}(\tau_2, \tau') d\tau_1 d\tau_2, \tag{A.5}$$

where G^0 denotes the unperturbed Green's function and the irreducible self-energy Σ contains diagrams due to both $\hat{H}_i(t)$ and $\hat{H}'(t)$.

Once the contour-ordered Green's functions are defined, e.g. using diagrammatic techniques, the real-time versions can be found using the conversion rules formulated by Langreth [75, 76]. By applying the Langreth rules to the contour-ordered Dyson equation and making some rearrangements we obtain the real time Dyson and Keldysh equations

$$G^r_{i,j}(\varepsilon) = G^{0,r}_{i,j}(\varepsilon) + \sum_{k,l} G^{0,r}_{i,k}(\varepsilon)\Sigma^r_{k,l}G^r_{k,j}(\varepsilon) \tag{A.6}$$

$$G^{\lessgtr}_{i,j}(\varepsilon) = \sum_{k,l} G^r_{i,k}(\varepsilon)\Sigma^{\lessgtr}_{k,l}G^a_{l,j}(\varepsilon). \tag{A.7}$$

Paper I

Evidence for a Single Hydrogen Molecule Connected by an Atomic Chain

M. Kiguchi,[1,*] R. Stadler,[2] I. S. Kristensen,[2] D. Djukic,[1] and J. M. van Ruitenbeek[1,†]

[1]*Kamerlingh Onnes Laboratorium, Universiteit Leiden, P.O. Box 9504, NL-2300 RA Leiden, The Netherlands*

[2]*Center for Atomic-scale Materials Physics, Department of Physics, NanoDTU, Technical University of Denmark, DK-2800 Kgs. Lyngby, Denmark*

(Received 28 December 2006; published 4 April 2007)

Stable, single-molecule conducting-bridge configurations are typically identified from peak structures in a conductance histogram. In previous work on Pt with H_2 at cryogenic temperatures it has been shown that a peak near $1G_0$ identifies a single-molecule Pt-H_2-Pt bridge. The histogram shows an additional structure with lower conductance that has not been identified. Here, we show that it is likely due to a hydrogen decorated Pt chain in contact with the H_2 molecular bridge.

DOI: 10.1103/PhysRevLett.98.146802 PACS numbers: 73.63.Rt, 63.22.+m, 73.23.−b, 85.65.+h

The interest in chains of single metal atoms bridging between two electrodes is largely due to their unique properties as ideal one-dimensional systems [1]. For clean metals, only Au, Pt, and Ir form atomic chains [2,3]. However, atomic or molecular adsorption on metal surfaces can widen this scope. Recently, 2 nm long Ag atomic chains have been created in the presence of oxygen at ultralow temperature, while clean Ag only forms short chains [4]. Atomic chains have been imaged by transmission electron microscope for the noble metals Cu, Ag, and Au [5–8].

In the first experiments contacting molecules by Pt atomic leads it was shown that a single hydrogen molecule H_2 can be contacted and there appeared to be no indication for atomic chain formation [9,10]. By use of point contact spectroscopy and shot noise measurements, the system was characterized in detail and close agreement with atomistic model calculations was obtained [9,10]. The Pt-H_2-Pt junction was first identified by its conductance. It shows up as a recurring plateau in the conductance when controllably breaking a contact, and in a histogram of conductance values collected for many such breakings it gives rise to a sharp peak near $1G_0$, where $1G_0 = 2e^2/h$ is the conductance quantum. This main peak at $1G_0$ for the Pt/H_2 system is therefore well understood. However, there is more structure in the conductance histogram for the Pt/H_2 junctions, which has not been explained. In particular, a strong peak is found at about 0.1–$0.2G_0$, suggesting that other configurations of hydrogen between Pt leads may be formed. In the present study we focus on those structures, having a conductance below $1G_0$, and we present evidence that they can be attributed to the formation of a hydrogen decorated Pt atomic chain that forms one of the leads contacting a hydrogen molecule.

The measurements have been performed using the mechanically controllable break junction technique (see Ref. [11] for a detailed description). Once under vacuum and cooled to 4.2 K a fine Pt wire was broken. Atomic-sized contacts between the wire ends can be formed using a piezoelement for fine adjustment. H_2 was admitted via a capillary. dc two-point voltage-biased conductance measurements were performed by applying a voltage in the range from 10 to 150 mV. Every statistical data set was built from a large number (over 3000) of individual digitized conductance traces. ac voltage bias conductance measurements were performed using a standard lock-in technique. The conductance was recorded for fixed contact configuration using an ac modulation of 1 mV amplitude and a frequency of 7.777 kHz, while slowly ramping the dc bias between −100 and +100 mV.

Figures 1(a) and 1(b) show typical conductance traces for clean Pt and for Pt after admitting H_2. After admitting H_2, plateau near $1G_0$ are frequently observed and the corresponding histogram [Fig. 1(c)] shows a sharp feature near $1G_0$. The plateau near $1G_0$ and the corresponding peak in the histogram originate from single-molecule Pt-H_2-Pt contacts, as shown by previous studies [9,10]. In addition to the $1G_0$ feature, the histogram shows a peak near $0.2G_0$ on top of a low-conductance tail. Looking at the individual traces, the conductance decreases by small steps after the appearance of a plateau near $1G_0$ (0.8–$1.2G_0$) for 92% of the traces, and the conductance decreases below

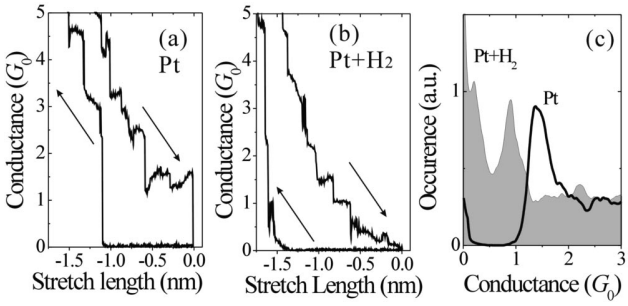

FIG. 1. Breaking and return traces for clean Pt (a), and for Pt in a H_2 atmosphere (b). Many of such curves are collected into conductance histograms as shown in (c) for clean Pt (black curve) and Pt in H_2 (filled graph).

$1G_0$ without appearance of a plateau near $1G_0$ for 8% of the traces. The sudden drop of the conductance from $1G_0$ to $0G_0$ is a rare event (below 1%). This suggests that a structure having a conductance below $1G_0$ is formed by further stretching the original single-molecule Pt-H_2-Pt contact with a conductance of $1G_0$. The conductance trace in Fig. 1(b) shows that the structure can be stretched to quite long lengths [>0.5 nm in Fig. 1(b)], which suggests the formation of an atomic chain.

In order to investigate the chain formation, we measure the length histogram of the last plateau and the return length distribution. Figure 2(a) shows the length histogram for the final conductance plateau for the Pt/H_2 contacts (filled gray distribution), and this is compared to a length histogram for clean Pt. The length for Pt/H_2 is taken here as the distance between the points at which the conductance drops below 1.3 and $0.1G_0$, respectively, while for clean Pt the boundaries are 2.5 and $1.0G_0$. The former boundaries are set such as to capture the length of the $1G_0$ plateau plus the subsequent structures that give rise to the peak around $0.2G_0$ in the conductance histogram. It is striking that the Pt/H_2 contact can be stretched as long as 0.8 nm. A sequence of peaks is observed in the Pt/H_2 length histogram of Fig. 2(a), indicating the repeated occurrence of certain stable chain configurations that we identify as (A), (B), and (C). The distance between the peaks is 0.27 ± 0.01 nm, which is slightly larger than the Pt-Pt distance of a clean Pt atomic chain (0.23 nm) [3].

The inset of Fig. 2(a) shows the average return lengths as a function of chain length. This is the distance over which the two electrodes need to be moved back after the junction breaks in order to reestablish contact, averaged over many break cycles. Apart from an offset of 0.3 nm due to the elastic response of the banks [3], the relation is approximately proportional, suggesting that a fragile structure is formed with a length corresponding to that of the last plateau, which is unable to support itself when it breaks and collapses onto the banks on either side.

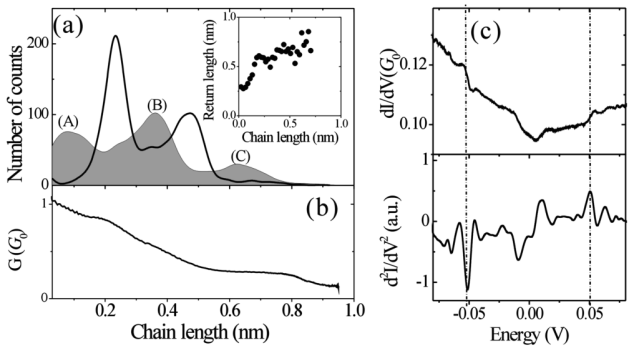

FIG. 2. (a) Length histogram for clean Pt (black curve) and Pt in H_2 (filled graph). The start and stop values between which the lengths were measured were taken as (2.5, 1.0) for Pt and (1.3, 0.1) for Pt/H_2, in units of G_0. Inset: Average return lengths as a function of chain length. (b) Average conductance as a function of chain length for Pt/H_2. (c) Differential conductance (top) and its derivative (bottom) for a Pt/H_2 contact taken at a conductance of $0.1G_0$.

We further test this interpretation by analyzing the stretch length dependence of the conductance and by point contact spectroscopy. Figure 2(b) shows the average conductance for Pt/H_2 junctions as a function of the chain length. The curve is obtained by adding all measured conductance traces from the start value ($1.3G_0$) onward, and dividing at each length by the number of traces included at that point. The mean conductance decreases rapidly as the chain becomes longer. Although the conductance for a pure Pt chain also decreases with length [12], its conductance stays well above $1G_0$. This fact, combined with the larger peak distance in the length histogram, indicates that the structure with lower conductance is probably not a clean Pt atomic chain, and may be due to a hydrogen decorated atomic chain. The average conductances of structures (A), (B), and (C) are 0.96, 0.56, and $0.28G_0$, respectively. Since the conductance of structure (A) is close to $1G_0$, we identify it with the single-molecule Pt-H_2-Pt contacts that have been studied previously [9,10]. We discuss the new structures (B) and (C) that arise by further stretching of the Pt-H_2-Pt junction in the following. Note that a stable level near $0.2–0.3G_0$ is observed at 0.6–0.8 nm in length in Fig. 2(b). The slow length dependence gives rise to a high number of counts in a conductance histogram, which explains the peak at $0.2G_0$ in Fig. 1(c). Apart from this stable structure that we have labeled (C) the length histogram points at an intermediate structure (B), for which the conductance varies more strongly with stretching.

Figure 2(c) shows an example of the differential conductance and its derivative for a Pt/H_2 contact taken at a conductance of $0.1G_0$. Clear symmetric peaks are observed at 51 meV in the second derivative, d^2I/dV^2. The peaks are commonly observed near $\sim 57 \pm 4$ meV for contacts having conductances in the range $0.6–0.1G_0$. The energy of 57 meV agrees with the energy of the transverse translation mode of the molecule in the Pt-H-H-Pt configuration [10]. This close agreement suggests that a hydrogen molecule is still bridging the junction after stretching it beyond the $1G_0$ plateau. Note that, in most measurements peaks are observed in the first derivative instead of the second derivative, where the analysis outlined in Ref. [13] was used to identify characteristic frequencies.

Based on the experiments presented above we arrive at the following chain formation model for Pt atomic contacts with H_2. First, a single hydrogen molecule is adsorbed between Pt electrodes [structure (A)]. Further stretching induces the incorporation of the first Pt atom from the stem part of the electrode into the chain [structure (B)]. Then, the second Pt-atom is incorporated into the chain [structure (C)], and the atomic chain is formed with a single hydrogen molecule bridging. The larger distances in the length histogram and the low conductance should then be attributed to additional hydrogen decorating the Pt atomic chain. Further support for this chain formation process is

obtained from density functional theory (DFT) calculations.

Electronic structure calculations were performed using a plane wave implementation of DFT [14] with an energy cutoff of 340 eV, where we used ultrasoft pseudopotentials [15], and a PW91 parametrization for the exchange and correlation functional [16]. The transmission functions of the molecular junctions were calculated using a general nonequilibrium Green function formalism for phase-coherent electron transport [17], where both the Green function of the scattering region and the self-energies describing the coupling to the semi-infinite electrodes were evaluated in terms of a basis consisting of maximally localized Wannier functions [18]. In our calculations the supercells for the scattering region are defined by 3×3 atoms in the surface plane and contain three to four surface layers on each side of the molecule. We used a 4×4 grid for the k-point integration in order to obtain well converged results for the conductance [19].

Based upon the distances and conductances found in the experiment presented above, we came to consider the model structures for (B) and (C) illustrated by the insets in Fig. 3. The figure shows calculated transmission functions for structures (B) and (C) as a function of energy. The transmission function for structure (A), a hydrogen bridge with no additional hydrogen having a conductance of $1G_0$ [20], is lowered when going from (A) to (C). The conductances are found as 0.46 and $0.15G_0$ for structures (B) and (C), respectively, which is in reasonable agreement with the experimental values of ~ 0.6 and $\sim 0.3G_0$. The theoretical values have been obtained after optimizing the distance between the contacts by total energy minimization and the optimal length of a Pt wire segment decorated with additional hydrogen was found to be 0.272 nm which agrees with the experimental results.

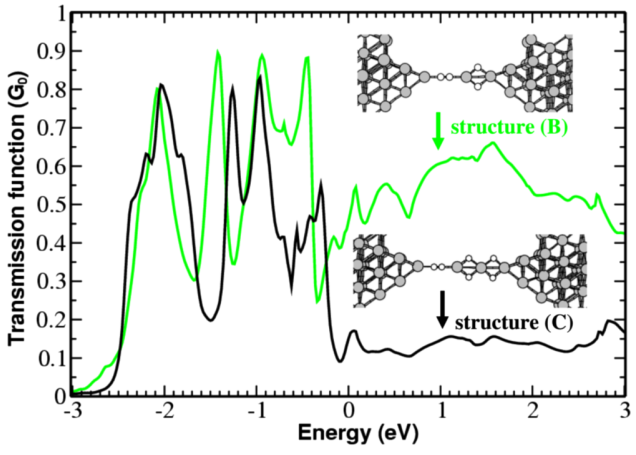

FIG. 3 (color online). Transmission functions for the proposed structures (B) solid gray (green) lines and (C) black lines, respectively, as calculated from DFT for a setup with bulk electrodes and a (111) surface with a pyramid of Pt atoms on top. The zero point of the x axis is the Fermi energy. The explicit geometries of the structures are shown as insets.

Our analysis shows that this reduction is due to the additional hydrogen atoms saturating the s orbital and part of the d orbitals between the Pt atoms they are attached to, thereby making them unavailable for electron transport. This is illustrated in Fig. 4(a) that shows the results of calculations for the H_2 bridge structure without additional hydrogen. We have simulated the effect hydrogen addition might have by cutting out Pt Wannier functions from the scattering Hamiltonian. The removal of the Pt s orbital for one and two subsequent wire atoms [shown only for the first case in Fig. 4(a)] accounts for the successive reduction of the transmission at around 1 eV and higher above the Fermi level. For the reduction of the transmission directly at E_F, and therefore the conductance, also a blocking of some of the d orbitals is needed, which is also shown in Fig. 4(a). Although a cutting of the d-Wannier functions of the first Pt atom alone does not have a large effect on the conductance and seems to even enhance it, the conduc-

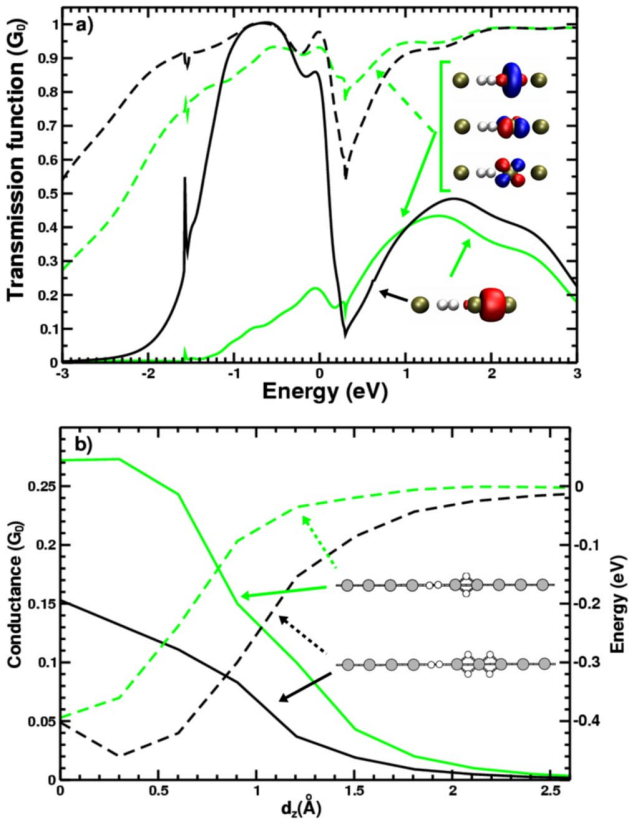

FIG. 4 (color online). (a) Transmission functions obtained from calculations of a single H_2 bridge between wires of Pt atoms with the s orbital (solid black line), the d orbitals [dashed gray (green) line], both the s and d orbitals [solid gray (green) line], and no atomic orbitals (dashed black line) removed from the Hamiltonian. The removed orbitals are also shown superimposed with the atomic positions in the insets. (b) Conductance (solid curves) and binding energy (dashed curves) for the molecule inside the junction for structures similar to (B) [gray (green)] and (C) (black) assumed to have linear atomic wire arrangements as shown in the insets.

tance is drastically reduced if both the *s* and *d* orbitals of the same Pt atom are blocked. We point out that our explanation of the conductance reduction is not in contradiction with the one given by Barnett *et al.* [21] for the Au-H_2-Au system [22] but just offers a different perspective. For structure (B) we also compared the transmission functions of the atomic wire system with that of the more realistic surface calculation in Fig. 3. Qualitatively, the results are similar in terms of the main peak structure illustrating that the analysis is robust with respect to details of the atomic arrangement. In a quantitative comparison, however, the conductance from the surface calculation is higher than for the wire system by approximately a factor of 2.0.

In Fig. 4(b) we show the dependence of the conductance with increasing the distance between the wire electrodes. In these calculations the positions of all hydrogen atoms and four Pt atoms on each side have been fully relaxed. The corresponding binding energy of the H_2 bridge molecule to the wires is also shown for comparison. Although there is a short plateau in the conductance for structure (B) when stretched beyond the optimal bonding distance, for structure (C) the overall decrease with the length seems to be slower up to a stretching length of 0.1 nm. This trend was also found in the experimental histogram. The shift in optimal distance between (B) and (C) just reflects the increase of the total cell length due to the expansion of a second wire segment.

Let us comment on the path that may lead to the structures discussed above. Since the bridging H_2 molecule is very weakly bound to the Pt electrodes, ''wire pulling'' seems to be unlikely. Structures (B) and (C) can only be formed by a concerted process. Such a process may involve the displacement of Pt atoms at the surface due to phonons and the formation of intermediate structures with the additional hydrogen adsorbed on the electrodes. The configuration space for covering all possibilities for atomic movements in such a process is too large to be explored by our calculations in detail.

In conclusion, the experimental evidence shows that a Pt-H_2-Pt single-molecule junction can be stretched further into forming an atomic wire. We propose a likely structure for this wire in terms of a Pt atomic chain decorated with hydrogen. This interpretation is supported by DFT calculations. While the pathway that brings new atoms into the atomic chain structure remains problematic, we obtain fair agreement in the numbers for the bond distances and the conductances.

We are grateful to K. W. Jacobsen for his support. We acknowledge support from FOM (NOW), Danish National Research Foundation, the Nano-Science Center at the University of Copenhagen, and the DCSC.

*Present address: Division of Chemistry, Graduate School of Science, Hokkaido University, Sapporo 060-0810, Japan.

†Electronic address: ruitenbeek@physics.leidenuniv.nl

[1] R. E. Peierls, *Quantum Theory of Solids* (Clarendon, Oxford, 1964).
[2] S. R. Bahn and K. W. Jacobsen, Phys. Rev. Lett. **87**, 266101 (2001).
[3] R. H. M. Smit, C. Untiedt, A. I. Yanson, and J. M. van Ruitenbeek, Phys. Rev. Lett. **87**, 266102 (2001); A. I. Yanson, G. R. Bollinger, H. E. van den Brom, N. Agrait, and J. M. van Ruitenbeek, Nature (London) **395**, 783 (1998).
[4] W. H. A. Thijssen, D. Marjenburgh, R. H. Bremmer, and J. M. van Ruitenbeek, Phys. Rev. Lett. **96**, 026806 (2006).
[5] H. Ohnishi, Y. Kondo, and K. Takayanagi, Nature (London) **395**, 780 (1998).
[6] V. Rodrigues and D. Ugarte, Phys. Rev. B **63**, 073405 (2001).
[7] V. Rodrigues, J. Bettini, A. R. Rocha, L. G. C. Rego, and D. Ugarte, Phys. Rev. B **65**, 153402 (2002).
[8] J. C. Gonzalez, V. Rodrigues, J. Bettini, L. G. C. Rego, A. R. Rocha, P. Z. Coura, S. O. Dantas, F. Sato, D. S. Galvao, and D. Ugarte, Phys. Rev. Lett. **93**, 126103 (2004).
[9] R. H. M. Smit, Y. Noat, C. Untiedt, N. D. Lang, M. C. van Hemert, and J. M. van Ruitenbeek, Nature (London) **419**, 906 (2002).
[10] D. Djukic, K. S. Thygesen, C. Untiedt, R. H. M. Smit, K. W. Jacobsen, and J. M. van Ruitenbeek, Phys. Rev. B **71**, 161402(R) (2005); D. Djukic and J. M. van Ruitenbeek, Nano Lett. **6**, 789 (2006).
[11] N. Agrait, A. Levy Yeyati, and J. M. van Ruitenbeek, Phys. Rep. **377**, 81 (2003).
[12] R. H. M. Smit, C. Untiedt, G. Rubio-Bollinger, R. C. Segers, and J. M. van Ruitenbeek, Phys. Rev. Lett. **91**, 076805 (2003).
[13] W. H. A. Thijssen, D. Djukic, A. F. Otte, R. H. Bremmer, and J. M. van Ruitenbeek, Phys. Rev. Lett. **97**, 226806 (2006).
[14] B. Hammer, L. B. Hansen, and J. K. Nørskov, Phys. Rev. B **59**, 7413 (1999); S. R. Bahn and K. W. Jacobsen, Comput. Sci. Eng. **4**, 56 (2002); The DACAPO code can be downloaded at http://www.fysik.dtu.dk/campos.
[15] D. Vanderbilt, Phys. Rev. B **41**, R7892 (1990).
[16] J. P. Perdew *et al.*, Phys. Rev. B **46**, 6671 (1992).
[17] Y. Meir and N. S. Wingreen, Phys. Rev. Lett. **68**, 2512 (1992).
[18] K. S. Thygesen and K. W. Jacobsen, Chem. Phys. **319**, 111 (2005).
[19] K. S. Thygesen and K. W. Jacobsen, Phys. Rev. B **72**, 033401 (2005).
[20] K. S. Thygesen and K. W. Jacobsen, Phys. Rev. Lett. **94**, 036807 (2005).
[21] R. N. Barnett, H. Haekkinen, A. G. Scherbakov, and U. Landman, Nano Lett. **4**, 1845 (2004).
[22] S. Csonka, A. Halbritter, and G. Mihaly, Phys. Rev. B **73**, 075405 (2006).

Paper II

Benchmark density functional theory calculations for nanoscale conductance

M. Strange,[a] I. S. Kristensen, K. S. Thygesen, and K. W. Jacobsen
Center for Atomic-scale Materials Design, Department of Physics, Technical University of Denmark, DK-2800 Kgs. Lyngby, Denmark

(Received 26 September 2007; accepted 8 January 2008; published online 20 March 2008)

We present a set of benchmark calculations for the Kohn-Sham elastic transmission function of five representative single-molecule junctions. The transmission functions are calculated using two different density functional theory methods, namely an ultrasoft pseudopotential plane-wave code in combination with maximally localized Wannier functions and the norm-conserving pseudopotential code SIESTA which applies an atomic orbital basis set. All calculations have been converged with respect to the supercell size and the number of $\mathbf{k}_{\parallel}$ points in the surface plane. For all systems we find that the SIESTA transmission functions converge toward the plane-wave result as the SIESTA basis is enlarged. Overall, we find that an atomic basis with double zeta and polarization is sufficient (and in some cases, even necessary) to ensure quantitative agreement with the plane-wave calculation. We observe a systematic downshift of the SIESTA transmission functions relative to the plane-wave results. The effect diminishes as the atomic orbital basis is enlarged; however, the convergence can be rather slow. © *2008 American Institute of Physics*. [DOI: 10.1063/1.2839275]

I. INTRODUCTION

First-principles calculations of electrical conductance in nanoscale contacts represent a main challenge in computational nanophysics. The interest for this type of calculations began in the mid-1990s, where advances in experimental techniques made it possible to contact individual molecules, thereby making it possible to study the transport of electrons through true nanoscale structures.[1,2] Apart from the scientific interest, the development of reliable simulation tools for nanoscale quantum transport is relevant not only in relation to the continued miniaturization of conventional semiconductor electronics but also for the introduction of a new generation of molecule based electronics.

It has by now become standard to calculate conductance in nanoscale contacts by employing a combination of nonequilibrium Green's function theory (NEGF) and ground state density functional theory (DFT). The resulting NEGF-DFT formalism provides a numerically efficient way of evaluating the Landauer-Büttiker conductance due to electrons moving in the effective Kohn-Sham (KS) potential without having to calculate the scattering states explicitly. It has been applied extensively to a number of different systems ranging from pure metallic contacts, over organic molecules, to carbon nanotubes suspended between metallic electrodes. Overall, the approach has been successful in describing qualitative features and trends;[3,4] however, quantitative agreement with experiments has mainly been obtained for strongly coupled systems such as metallic point contacts, monatomic chains, as well as junctions containing small chemisorbed molecules.[5–7]

It is generally accepted that the NEGF-DFT method only provides an approximation to the true conductance—even if the exact exchange-correlation (xc-)functional could be used, and the quality of the result is expected to be strongly system dependent. Moreover, it is not easy to estimate the effect of using approximate xc functionals such as the local-density approximation (LDA) or generalized gradient approximation (GGA). We mention here that more sophisticated methods for quantum transport based on configuration interaction, the GW method, time-dependent DFT, and the Kubo formula have recently been proposed.[8–12] However, these schemes are considerably more demanding than the NEGF-DFT and at present, they cannot replace NEGF-DFT in practical applications.

Irrespective of the validity of the NEGF-DFT approach and the role played by the approximate functionals, it remains important to establish a general consensus concerning the exact result of a NEGF-DFT calculation for a given xc functional and specified system geometry, i.e., a benchmark. Although this might seem trivial, the present situation is rather unsatisfactory as different results have been published by different groups for the same or very similar systems (several examples will be given in the text). Perhaps, the best example is provided by benzene dithiolate between gold contacts where the calculated conductance varies with up to two orders of magnitude for similar geometries.[3,13–18]

The relatively large variation of the results indicates that the conductance, or more generally, the elastic transmission function, is a highly sensitive quantity. Indeed, the implementation of the open boundary conditions defining the scattering problem represents some numerical challenges. Small errors in the description of the coupling between the finite scattering region and the infinite leads as well as improper *k*-point samplings in supercell approaches can introduce significant errors in the resulting transmission function.

[a]Electronic mail: strange@fysik.dtu.dk.

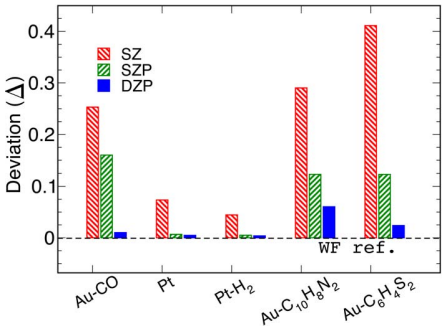

FIG. 1. (Color online) Deviation between the WF and SIESTA transmission functions for the five reference systems studied. The dashed line indicates zero deviation from the WF transmission. Notice that the SIESTA results converge toward the WF result as the PAO basis is enlarged.

In this paper, we take a first step toward establishing a common reference for NEGF-DFT calculations by performing benchmark calculations for a set of five representative nanoscale contacts. The benchmarking is achieved by comparing the transmission function obtained using two different and independent, albeit similar, NEGF-DFT methods: In one case, the Hamiltonian is obtained from the SIESTA DFT program which uses a basis of localized pseudoatomic orbitals (PAOs) together with norm-conserving pseudopotentials. The second method applies a basis of maximally localized Wannier functions (WFs) obtained from the DACAPO DFT code which uses plane waves and ultrasoft pseudopotentials. In both cases, we use periodic boundary conditions in the directions perpendicular to the transport direction and we apply the PBE xc functional.[19]

The five reference systems we have chosen for our benchmark study are (i) a monoatomic gold chain with a single CO molecule adsorbed, (ii) a three-atom Pt chain suspended between Pt electrodes, (iii) an H_2 molecule bridging two Pt electrodes, (iv) benzene-dithiolate (BDT) between Au electrodes, and (v) bipyridine between Au electrodes. The systems have been chosen according to the criterion that both experimental data as well as previous NEGF-DFT calculations are available in the literature. Furthermore, they are representative in the sense that they cover a broad class of systems: Homogeneous and heterogeneous, computationally simple (one dimensional) and more complex, and strongly as well as weakly coupled.

A main result of our work is summarized in Fig. 1 where we show the overall deviation,

$$\Delta = \frac{1}{E_0 - E_1} \int_{\varepsilon_F + E_1}^{\varepsilon_F + E_0} |T_{\mathrm{WF}}(\varepsilon) - T_{\mathrm{PAO}}(\varepsilon)| \mathrm{d}\varepsilon, \tag{1}$$

between the transmission functions calculated using the WF and PAO basis sets, respectively. The energy E_1 is taken as the lowest lying band edge in the lead, while the cutoff energy E_0 is taken to be the energy above which the WFs are no longer able to reproduce the exact KS eigenstates of the system which is typically ~3 eV above the Fermi level. For all the systems, we find that the deviation Δ decreases as the SIESTA basis is enlarged, meaning that the SIESTA transmission functions converge toward the WF result. We take this as evidence for the correctness of the WF results and the justification for the use of the term *benchmark* calculation.

In general, we find that the double-zeta polarized (DZP) basis provides very good agreement with the WF basis, whereas the single-ZP (SZP) and, in particular, the SZ basis can produce substantially incorrect features in the transmission function.

The paper is organized as follows. In Sec. II, we briefly review the NEGF-DFT formalism and introduce the two specific implementations used in the present study. In Secs. III–VI, we present the benchmark calculations for the five reference systems, and in Sec. VIII, we give our conclusions.

II. METHOD

In this section, we first outline the NEGF-DFT method which has become standard for nanoscale conductance calculations. The two specific NEGF-DFT implementations applied in the present work are then introduced and their key parameters are discussed. We then consider the important issue, common to both methods, of how to treat periodic boundary conditions in the plane perpendicular to the transport direction. We end the section with a discussion of the advantages and disadvantages of the two methods.

A. NEGF-DFT

The zero temperature, linear response conductance due to noninteracting electrons scattering off a central region (C) connected to thermal reservoirs via two ballistic leads (L and R) can be written as

$$G = G_0 T(\varepsilon_F), \tag{2}$$

where $T(\varepsilon)$ is the elastic transmission function and $G_0 = 2e^2/h$ is the quantum unit of conductance. Using the NEGF formalism, Meir and Wingreen have derived a very useful formula which expresses the transmission function in terms of the Green's function of the central region,[20]

$$T(\varepsilon) = \mathrm{Tr}[G^r(\varepsilon)\Gamma_L(\varepsilon)G^a(\varepsilon)\Gamma_R(\varepsilon)]. \tag{3}$$

In this expression, the trace runs over the central region basis functions and $\Gamma_{L/R}$ is obtained from the lead self-energies [defined in Eq. (5) below] as $\Gamma_{L/R} = i(\Sigma_{L/R} - \Sigma_{L/R}^\dagger)$.

In the NEGF DFT method, both the leads and central region are modeled by the effective KS Hamiltonian, $\hat{h}_{\mathrm{KS}} = \frac{1}{2}\nabla^2 + v_{\mathrm{eff}}(\mathbf{r})$. The self-consistent effective potential consists of the well-known parts $v_{\mathrm{eff}} = v_{\mathrm{ext}} + v_H + v_{\mathrm{xc}}$. Introducing a basis of localized orbitals, $\{\phi_i\}$, we define the Hamiltonian and overlap matrices by $H_{ij} = \langle \phi_i | \hat{h}_{\mathrm{KS}} | \phi_j \rangle$ and $S_{ij} = \langle \phi_i | \phi_j \rangle$, respectively. In the original derivation by Meir and Wingreen, the basis was assumed to be orthogonal, but the generalization to nonorthogonal basis sets shows that Eq. (3) still holds when the Green's function is defined as[21]

$$G(z) = [zS_C - H_C - \Sigma_L(z) - \Sigma_R(z)]^{-1}. \tag{4}$$

Here, the matrices H_C and S_C are the blocks of H and S corresponding to the central region basis functions. The retarded Green's function $G^r(\varepsilon)$ is obtained for $z = \varepsilon + i0^+$, and the advanced Green's function is obtained for $z = \varepsilon - i0^+$ or $G^a = (G^r)^\dagger$.

The self-energy of lead α is given by

$$\Sigma_\alpha(z) = (zS_{C\alpha} - H_{C\alpha})g^0_\alpha(z)(zS_{\alpha C} - H_{\alpha C}), \quad (5)$$

where $H_{C\alpha}$ and $S_{C\alpha}$ are the coupling and overlap matrices between basis functions in the central region and lead α, respectively. g^0_α is the surface Green's function describing the isolated semi-infinite lead, $g^0_\alpha(z)=[zS_\alpha - H_\alpha]^{-1}$, which can be calculated recursively using the decimation technique.[22] We have used a finite value for the positive infinitesimal 0^+ in the leads and in the central region of 10^{-1} and 10^{-3} eV, respectively. By using a relatively large infinitesimal in the lead, we obtain a considerably speedup due to faster convergence of the recursive calculation of the surface Green's function. We checked that a smaller value does not change our results.

B. Method 1: Wannier functions from plane-wave DFT

In method 1, the Kohn-Sham Hamiltonian is obtained from an accurate plane-wave pseudopotential DFT code.[23] The ion cores are replaced by ultrasoft pseudopotentials,[24] and we use an energy cutoff of 25 Ry for the plane-wave expansion. The Kohn-Sham eigenstates are transformed into partly occupied WFs,[25] which are used to obtain a tight-binding-like representation of the Hamiltonian. The WFs are constructed such that any eigenstate below a selected energy E_0 can be exactly represented by a linear combination of WFs. In the applications, we have chosen E_0 in the range of 2–4 eV above the Fermi level. In this way, the accuracy of the plane-wave calculation is carried over to the WF basis for all energies relevant for transport.

By performing separate DFT calculations for the (periodic) leads and C, we obtain a set of WFs for each region. Note that C always contains a few buffer layers of the lead material on both sides of the nanocontact to ensure that the KS potential at the end planes of C has converged to its value in the leads. Since the WFs in the lead, in general, will differ from those in the outermost lead unit cells of the central region, care must be taken to evaluate the coupling and overlap matrices $H_{C\alpha}$ and $S_{C\alpha}$. Notice also that although the WFs by construction are orthogonal within each region, WFs belonging to different regions will, in general, be nonorthogonal. For more details on the construction of the WFs and the calculations of the Hamiltonian matrix for the combined L-C-R system, we refer to Ref. 26. We shall refer to the results obtained from method 1 as the WF results.

C. Method 2: PAO SIESTA basis

Method 2, is based on the DFT code SIESTA,[27] which uses finite range PAOs (Ref. 28) as basis functions and Troullier-Martins norm-conserving pseudopotentials.[29] As in method 1, the Hamiltonians for the leads and the central region are obtained from separate calculations. Because the KS potentials to the left and right of C, by definition have converged to the value in the leads, we can take the coupling between central region and lead α, $H_{C\alpha}$, from the pure lead calculation. Note that this is in contrast to method 1, where the different shapes of the WFs in the periodic lead and the lead part of the central region make it essential to evaluate the coupling matrix directly. Note also that this approximation, i.e. the use of the intralead coupling matrix elements ($H_{\alpha\alpha}$) in $H_{C\alpha}$, can be controlled by including a larger portion of the lead in C. In practice, we find that three to four atomic layers must be included in C on both sides of the junction to obtain converged conductances.

In the present study, we restrict ourself to the standard PAOs for SIESTA: SZ, SZP, and DZP. For the confinement energy, determining the range of PAOs, we use 0.01 Ry, and for the mesh cutoff, we use 200 Ry.

D. Common ingredients

In both methods 1 and 2, we treat exchange and correlation effects with the PBE energy functional.[19] Furthermore, we impose periodic boundary conditions in the surface plane directions. This means that we are, in fact, considering the conductance of a periodic array of junctions instead of just a single junction. Instead of the localized basis function $\phi_n(\mathbf{r})$ (this could be a WF or a PAO), we thus consider the Bloch function

$$\chi_{n\mathbf{k}_\parallel} = \sum_{\mathbf{R}_\parallel} e^{i\mathbf{k}_\parallel \cdot \mathbf{R}_\parallel} \phi_n(\mathbf{r} - \mathbf{R}_\parallel), \quad (6)$$

where $\mathbf{R}_\parallel$ runs over supercells in the surface plane and $\mathbf{k}_\parallel$ is a wave vector in the corresponding two-dimensional Brillouin zone (BZ). Since $\mathbf{k}_\parallel$ is a good quantum number, we can construct the Hamiltonian, $H(\mathbf{k}_\parallel)$, for each $\mathbf{k}$ point separately. This, in turn, implies that the conductance *per* junction is given by the average

$$G = \sum_{\mathbf{k}_\parallel} w(\mathbf{k}_\parallel) G(\mathbf{k}_\parallel), \quad (7)$$

where $w(\mathbf{k}_\parallel)$ are symmetry determined weight factors. Unless stated otherwise, we have used a 4×4 Monkhorst-Pack $\mathbf{k}_\parallel$-point sampling of the surface BZ, which for all the systems studied yields conductances converged to within a few percent.[26,30] We take the Fermi level of the bulk lead as the common Fermi level of the combined system by shifting the levels in the central region by a constant. This is done by adding to H_C the matrix δS_c, where $\delta=[H_L]_{0,0}-[H_C]_{0,0}$ and the (0,0) element corresponds to the on-site energy of a basis function located near the interface between L and C.

The main advantages of method 1 are the following: (i) The accuracy of the plane-wave calculation carries over to the WF basis set. (ii) The WF basis set is truly minimal and often results in even fewer basis functions than a SZ basis. The WF basis, thus, combines high accuracy with high efficiency. The price that one has to pay is that the actual construction of well localized WFs is not always straightforward and requires some user interaction, in particular, for metallic systems. Also, the lack of finite support of the WFs is unwanted in the context of transport; although in practice, it is not a serious problem since the WFs are well localized. Finally, as already explained above, the risk of obtaining different WFs for two similar but nonidentical systems renders it less straightforward to patch the parts together using the Hamiltonians obtained for the separate calculations.

Most of the disadvantages of the WF basis are resolved by the PAO basis set: By construction, they have finite sup-

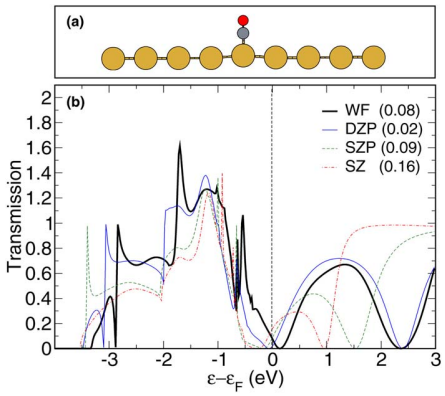

FIG. 2. (Color online) (a) Central region used to describe a single CO molecule adsorbed on a monatomic Au wire. (b) Transmission functions for the Au wire CO system calculated using method 1 (WF) and method 2 for three different PAO basis sets. The transmission function at the Fermi level is indicated in the parentheses following the legends.

port and are identical as long as the atomic species on which they are located are the same. This renders it straightforward to patch together Hamiltonians for separate subsystems as long as the KS potential can be smoothly matched at the interfaces. On the other hand, to obtain an accuracy matching the WFs, one needs to use a significantly larger number of orbitals and, thus, longer computation times as compared to the WF method.

III. GOLD CHAIN WITH CO

In this section, we calculate the conductance of an infinite gold chain with a single CO molecule adsorbed. Scanning tunneling microscope (STM) experiments suggest that CO strongly depresses the transport of electrons through gold wires.[31] This has been supported by NEGF-DFT calculations[32] which show that the transmission function indeed drops to zero at the Fermi level. The use of infinite gold chains as leads is clearly an oversimplification of the real situation; however, the model seems to capture the essential physics, i.e., the suppression of the conductance, and furthermore, is well suited as a benchmark system due to its simplicity.

The geometry of the system is shown in Fig. 2(a). We use a supercell with transverse dimensions of 12×12 Å^2 and take all bond lengths from Ref. 32: $d_{\mathrm{Au-Au}}=2.9$ Å, $d_{\mathrm{Au-C}}=1.96$ Å, and $d_{\mathrm{C-O}}=1.15$ Å. The Au atom holding the CO is shifted toward CO by 0.2 Å. In method 1, we obtain six WFs per Au atom and seven WFs for the CO molecular states. Due to the elongated bond length of the Au wire, we found it necessary in method 2 to increase the range of the Au PAOs in order to converge the band structure of the Au wire. The confinement energy was, therefore, in this case set to 10^{-4} Ry.

In Fig. 2(b), we show the calculated transmission function using three different PAO basis sets and the WF basis set. Overall, the PAO result approaches the WF result as the basis set is enlarged. For the largest PAO basis (DZP), the agreement is, in fact, very satisfactory given the differences in the underlying DFT methods, e.g., ultrasoft versus norm-conserving pseudopotentials. The remaining difference can be further reduced by a rigid shift of the DZP transmission by about 0.15 eV.

All transmission functions feature an antiresonance near the Fermi level. However, upon enlarging the PAO basis, the position of the antiresonance shifts as follows: −0.27 (SZ), −0.16 (SZP), −0.06 (DZP), and 0.12 eV (WF). Note that the position of the antiresonance obtained with the WFs is approached as the PAO basis set is increased. Also, the curvature of the antiresonance is improved as the PAO basis set is enlarged. The improvements in these features are, however, not directly reflected in the conductances indicated in the parentheses following the legends in Fig. 2(b). The reason for this apparent disagreement is the rigid shift between the PAO and WF transmission functions.

We observe that our results differ from the calculation in Ref. 32: While the latter finds two peaks in the energy range of 0–2 eV, our converged transmission function shows a single broad peak. In general, both our PAO and WF based transmission functions present less structure than the transmission function reported in Ref. 32. We suspect that these differences are related to the way the coupling $H_{\alpha C}$ is calculated in Ref. 32.

IV. Pt CONTACT

Atomic point contacts formed from late transition metals such as Au, Pt, and Pd show very stable and reproducible features in conductance measurements.[1] This, together with the simplicity implied by their homogeneity, makes them ideal as benchmark systems for transport calculations. Here, we consider the conductance of a pure Pt contact for which both experimental conductance data[33–36] as well as theoretical calculations[5,7,37] are available.

Conductance histograms obtained from mechanically controlled break junction experiments on pure Pt samples show a peak near $1.5G_0$, indicating that as a Pt contact is pulled, structures with a conductance at around $1.5G_0$ are frequently formed. NEGF-DFT calculations have shown that (zigzag) monatomic Pt chains indeed have a conductance close to this value.[5,7,36] Moreover, the calculations predict an increasing conductance as the Pt chain is stretched and evolves from a zigzag to a linear configuration. This effect has also been observed experimentally.[35]

In Fig. 3(a), we show the supercell used to model the scattering region of the Pt contact. The Pt contact is modeled by two four-atom pyramids attached to (111) surfaces containing 3×3 atoms in the surface plane. In order to ensure that the effective KS potential has converged to its bulk value at the end planes of the supercell, we include three to four atomic layers (*ABC-CABC* stacking) on either side of the pyramids. The chain is formed by inserting a single Pt atom between the apex atoms of the two pyramids. We have relaxed the contact region (pyramids+chain) while keeping the rest of the structure fixed in the bulk configuration with lattice constant of 3.93 Å and a distance of 14.60 Å between the (111) surfaces. The cutoff energy used in the construction of WFs was set to $\varepsilon_F+4.0$ eV ensuring that the KS eigenstates below this value are exactly reproducible in terms of

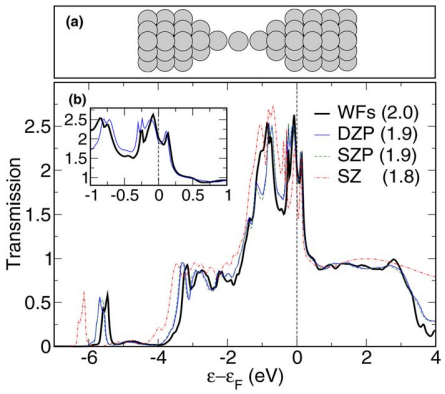

FIG. 3. (Color online) (a) Supercell used for the DFT calculation of a short linear Pt chain between Pt(111) surfaces. (b) The calculated transmission function using methods 1 and 2. The transmission at the Fermi level is indicated in the parentheses following the legends. In the inset, we show the transmission function in the important region near the Fermi level for the DZP basis set and the WF basis set.

the WFs. The transmission function was converged by a 4×4 $\mathbf{k}_{\parallel}$-point sampling as stated in Sec. II D.

In Fig. 3(b), we show the calculated transmission functions using methods 1 and 2. The qualitative agreement between the two methods is striking; however, only the SZP and DZP basis sets provide quantitative agreement with the WF result. The SZ basis set results in a downshift of the peak at −6 eV and an incorrect description of the features in the important region near the Fermi level. Here, the converged transmission function shows two peaks positioned at ε_F −0.8 eV and just below the Fermi level, respectively. The main peak astride the Fermi level, in fact, consists of three smaller peaks, as seen more clearly in the inset for the DZP and WF basis sets. These particular features in the transmission function were also observed in Ref. 37 for a similar Pt contact, employing a method based on quantum chemistry software and a description of the bulk electrodes by a semiempirical tight-binding Hamiltonian on a Bethe lattice.[38] Also, the calculated conductance of $2.3G_0$ is in agreement with our results, considering the structural differences.

In Fig. 4, we show the calculated conductance of the Pt contact for three electrode displacements. The three configurations correspond to an unstrained Pt chain, the chain just before it snaps, and the broken chain, respectively. The surface-surface distances are 13.62, 14.60, and 14.75 Å in the three cases.

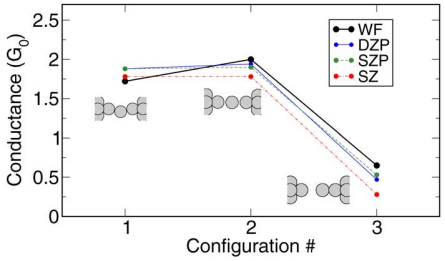

FIG. 4. (Color online) Conductance for three different configurations during the stretching of a small Pt chain. Configurations 1, 2, and 3 correspond to the unstrained chain, maximally strained chain, and a broken chain, respectively. The contact atoms are shown in the insets.

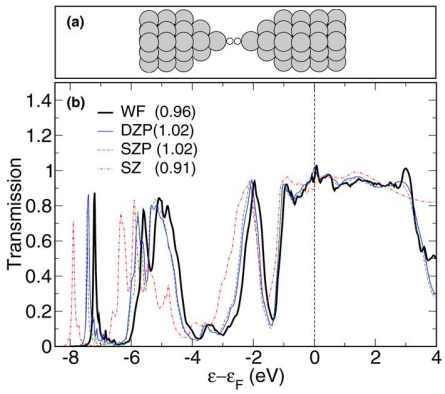

FIG. 5. (Color online) (a) Supercell used to model the central region of the Pt−H_2−Pt junction. (b) Transmission function for the Pt-hydrogen bridge. The transmission function at the Fermi level is indicated in the parentheses following the legends.

All basis sets, except for the SZ, are able to reproduce the trend of increasing conductance prior to rupture. The SZ basis set underestimates the absolute conductance by nearly $0.5G_0$ in the strained and broken configurations as compared to the WF result. The conductance calculated with the SZP and DZP basis sets is almost identical and shows results more consistent with the WF basis for all three configurations.

V. Pt−H_2−Pt CONTACT

In this section, we consider the simplest possible molecular junctions, namely, a single hydrogen molecule between metallic Pt contacts. Similar to the metallic point contacts, the Pt−H_2−Pt junction shows stable and reproducible behavior in conductance measurements. In particular, a very pronounced peak close to $1G_0$ appears in the conductance histogram obtained when a Pt contact is broken in a hydrogen atmosphere.[33] Although reported conductance calculations show significant variation (see below), there have been given substantial evidence that the structure responsible for the peak consists of a single hydrogen molecule bridging the Pt contacts.[33,39]

Several groups have published NEGF-DFT calculations for the transmission function of the Pt−H_2−Pt system. Most find a conductance of $(0.9-1.0)G_0$,[4,6,33,41] but also much lower values of $(0.2-0.5)G_0$ have been reported in Ref. 40.

For the benchmark calculations, we use the same setup as in Sec. IV with the central Pt atom replaced by a hydrogen molecule [see Fig. 5(a)]. The relevant bond lengths determining the structure after relaxation of the Pt pyramids and the hydrogen atoms are $d_{\mathrm{Pt-H}}=1.7$ Å and $d_{\mathrm{H-H}}=1.0$ Å.

In Fig. 5(b), we show the calculated transmission functions. Similar to the case of the Pt contact, the agreement between the different calculations is striking, especially in the important region around the Fermi level. The SZ basis set reproduces the qualitative features of the larger basis sets but introduces a considerable downshift of the low-lying peaks.

The very good agreement between the two methods indicates that the transmission function for this system is rather insensitive to the basis set. We stress, however, that a proper $\mathbf{k}_{\parallel}$-point sampling of the transmission function is crucial to

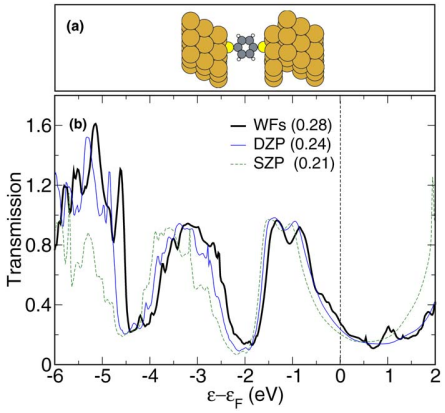

FIG. 6. (Color online) (a) Supercell used to model the central region of the Au(111)–BDT–Au(111) system with S at the fcc hollow site. (b) The calculated transmission functions. Note, that the SZ transmission function has been omitted for clarity. The transmission function at the Fermi level is indicated in the parentheses following the legends.

obtain meaningful results independently of the quality of the basis set. Restricting the calculation to the Γ point yields a transmission function with a (unphysical) peak at the Fermi level.[6] We note in passing that such a peak is present in the transmission function reported in Ref. 4. Such unphysical features resulting from an insufficient $\mathbf{k}_{\|}$-point sampling are not properties of the molecular junction but are rather due to van Hove singularities in the quasi-one-dimensional leads.[30] The results reported in Ref. 41 are based on SIESTA DFT code and show good agreement with our results. The conductance obtained in one of the early theoretical calculations[40] on the hydrogen molecular bridge is considerably lower than our and most other results. The calculational method applied in Ref. 40 is, however, the same as applied in the study of pure Pt contacts,[37] which agrees well with our results as discussed in Sec. IV. We speculate if this could be related to the smaller size of the Pt cluster used to model the electrodes in Ref. 40 as compared to the one used in Ref. 37. Another possibility for the discrepancies is the use of the B3LYP energy functional in Ref. 40 instead of a LDA/GGA functional used in most other works.

VI. BENZENE-1,4-DITHIOL BETWEEN Au(111) SURFACES

The BDT molecule suspended between gold electrodes was among the first single-molecule junctions to be studied and has become the standard reference for calculations of nanoscale conductance. Depending on the experimental setup, measured conductances vary between $10^{-4}G_0$ and $10^{-1}G_0$,[42–46] while the calculated values typically lie in the range of $(0.05-0.4)G_0$.[3,13,16–18,47–49] In general, it has been found that the transmission function is strongly dependent on the bonding site of the S atom,[18,48] while variations in the Au–S bond length only affects the transmission function weakly.[47]

As our objective is to establish a computational benchmark for the Au-BDT system, we choose the simple junction geometry, shown in Fig. 6(a). The S atoms are placed at the minimum energy positions in the fcc hollow sites of the Au(111) surface and the molecule has been relaxed while keeping the Au atoms fixed in the bulk crystal structure. We use a Au lattice constant of 4.18 Å and a distance between the Au(111) surfaces of 9.68 Å. With these constrains the relevant bond lengths are $d_{\mathrm{Au-S}}=2.45$ Å, $d_{\mathrm{S-C}}=1.73$ Å, and $d_{\mathrm{C-H}}=1.09$ Å.

In Fig. 6(b), we show the calculated transmission functions (the SZ result has been omitted for clarity). Notice that we plot the transmission function only up to 2 eV above the Fermi level. This is because the WF transmission at larger energies is sensitive to the parameters used in the construction of the WFs, in particular, the cutoff energy E_0, and thus, we cannot be sure about the WF result above 2 eV$+\varepsilon_F$.

The three transmission functions agree very well in the energy range from 2 eV below the Fermi level to 1 eV above the Fermi level, while only the DZP result agrees quantitatively with the WF result in the entire energy range. We again notice the downshift of the PAO transmission functions relative to the WF result.

The presence of a broad transmission peak positioned at ~1 eV below the Fermi level is in qualitative agreement with previous results.[3,16,47,48,50,51] For more stretched configurations, i.e., for larger values of the S–C bond length, than the one used in the present study, the broad peak splits into two more narrow peaks.[26]

The transmission function presented in Ref. 3 was obtained using a method very similar to our method 2; however, the reported conductance of $0.4G_0$ is almost twice as high as our DZP results of $0.24G_0$. The large conductance arises because the transmission peak closest to the Fermi level is considerably broader than what we find. If, however, we restrict the $\mathbf{k}_{\|}$ to the Γ point, we find the same broadening as in Ref. 3 and a very similar conductance of $0.37G_0$. Another feature of the Γ-point only transmission function is that the second peak positioned at ~3 eV below the Fermi level separates into a number of more narrow peaks.

In Ref. 16, the transmission function is calculated from the linear combination of muffin-tin orbitals–atomic sphere approximation method and averaged over 36 irreducible $\mathbf{k}_{\|}$ points. Both the width and the position of the two peaks in the transmission function at 1 and 3 eV below the Fermi level are in good agreement with our results. The height of the former peak is, however, lower than in our calculation and this reduces the conductance to a value of $0.07G_0$. We suspect that this difference could be due to differences in the adopted contact geometries.

When comparing a supercell approach to quantum transport with a cluster based calculation as the one in Ref. 47, it is essential that (i) the cluster size is converged and (ii) the number of $\mathbf{k}_{\|}$ points and supercell size are converged. In the supercell approach, a $N\times N$ Monkhorst-Pack sampling of the surface Brillouin zone corresponds to a Γ-point calculation for a supercell consisting of the original supercell repeated $N\times N$ in the surface plane.[25]

Extrapolating our converged calculations for 3×3 atoms within the surface plane of the supercell and 4×4 $\mathbf{k}_{\|}$ point to a Γ-point calculation gives a supercell consisting of ~1000 atoms. We speculate that clusters of similar sizes are needed to reach the same level of convergence. However, the re-

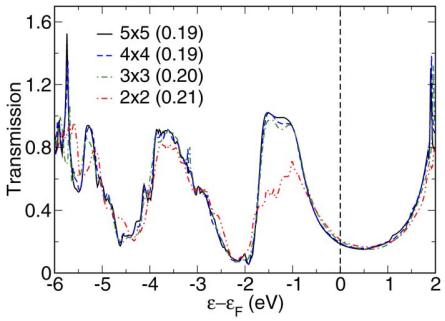

FIG. 7. (Color online) The transmission function of Au(111)–BDT–Au(111) for supercells containing a single BDT molecule and with the number of Au(111) surface atoms varying from 2×2 to 5×5 atoms, as indicated in the legends. All the calculations apply the SZP basis set and have been converged with respect to the number of $\mathbf{k}_\parallel$ points. The transmission function at the Fermi level is indicated in the parentheses following the legends.

peated supercell introduces a periodic array of molecules on the surface, which could give rise to interference effects blurring the comparison to single-molecule cluster calculations. To quantify this intermolecule interference effect, we show in Fig. 7 the SZP transmission function for the Au(111)–BDT–Au(111) system, where the number of Au atoms in the surface plane is varied from 2×2 to 5×5 atoms. Each calculation has been converged with respect to the number of $\mathbf{k}_\parallel$ points by a 4×4 Monkhorst-Pack sampling for all the supercells, except the smallest supercell for which 8×8 $\mathbf{k}_\parallel$ points was needed.

It is evident that the transmission function is well converged with 3×3 atoms in the surface plane. This shows that our calculations should be directly comparable to fully converged single-molecule cluster calculations.

VII. BIPYRIDINE BETWEEN Au(111) SURFACES

As the last reference system, we consider a bipyridine molecule attached between two gold electrodes. STM experiments on bipyridine molecules in a toluene solution[52] show that the conductance of Au-bipyridine junctions is quantized in multiples of $0.01G_0$ which was interpreted as the formation of stable contacts containing one or more molecules. The conductance is expected to be sensitive to the details of the contact geometry;[53] however, for the benchmark calculation, we use a flat Au(111) surface with bipyridine binding at an on-top site which is the minimum energy configuration, as shown in Fig. 8(a). The Au electrodes are the same as used for the BDT molecule in Sec. VI. The Au(111)–N distance is 2.180 Å, while the distance between the Au(111) surfaces is 11.53 Å.

The transmission functions calculated using either PAOs or WFs are shown in Fig. 8(b). At first, it is noted that the overall structures of the transmission functions are similar. We have used a logarithmic scale to make the differences in the low transmission regime more visible. In the SIESTA calculations, the position of the narrow lowest unoccupied molecular orbital (LUMO) peak which governs the transport is underestimated but converges toward the WF result as the PAO basis set is enlarged [see the inset of Fig. 8(b)]. The alignment of the LUMO energy level with respect to the

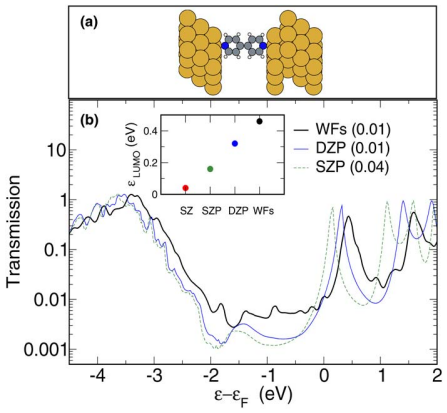

FIG. 8. (Color online) (a) Supercell used to describe the central region of the bipyridine-Au(111) junction. (b) Calculated transmission functions (the SZ result has been omitted for clarity). The inset shows the dependence of the LUMO position on the basis sets. The transmission function at the Fermi level is indicated in the parentheses following the legends.

Fermi level and its relation to charge transfer were studied in Ref. 54. The LUMO peak is close to the Fermi level and in this regime, it is expected that small changes in the position of the LUMO peak should change the conductance considerably. However, this is not the case when comparing the DZP basis set to the WF basis set since the conductance is, in fact, unchanged even though the position of the LUMO peak differs. The reason is that the WF transmission function has a different tail in the high barrier tunneling regime. The origin of this difference can be twofold: (i) The density of states of the Au(111) surface which influence the LUMO's density of states could be different in the two cases. (ii) Although the WFs have rapidly decaying tails, they do not vanish and, therefore, they must be truncated. This truncation could introduce artificial features in the transmission function in the low tunneling regime.

Several groups have investigated the transport properties of bipyridine-gold junctions, and there is general agreement that the low bias conductance depends crucially on the details of the contact geometry. As different groups have chosen different geometries and models for the gold electrodes, a direct comparison of the reported transmission functions is difficult.

To the best of our knowledge, the first theoretical paper on the bipyridine system is by Tada *et al.*[55] In their calculations, bipyridine is adsorbed on top of a Au atom of a rather small Au cluster, and the coupling to the infinite electrodes is modeled by a broadening parameter fitted to experimental data. The zero-voltage transmission function contains some of the same peak structures as we observe. Hou *et al.*[56] have published several papers on the gold-bipyridine junction. Similar to Tada *et al.*, they include only a few gold atoms in the *ab initio* calculation and treat the coupling to electrodes through a model self-energy term. The peak structure of the transmission function is quite different from ours. This could be due to the small size of the gold clusters used to mimic the electrodes. While most other groups observe tunneling through the LUMO tail,[53,54,57] Hou *et al.* argue that the transport is mainly taking place via the highest occupied MO–2 state. Calculations by Wu and co-workers[58,59] obtained using

a SIESTA-based transport code,[60] for bipyridine attached to the on-top site of a gold surface show overall good agreement with our results [see Fig. 7(a) in Ref. 58]. The minor differences are probably related to the fact that only the Γ point has been used in the latter paper.

VIII. CONCLUSIONS

We have established a set of benchmark calculations for the Kohn-Sham (PBE) elastic transmission function of five representative single-molecule junctions using two different methods based on independent DFT codes: (i) A plane-wave DFT code in combination with maximally localized Wannier functions. (ii) The SIESTA program which applies finite range pseudoatomic orbitals.

For all five systems, we find that the SIESTA result converges toward the WF result as the SIESTA basis is enlarged from SZ to DZP with the latter yielding very good quantitative agreement with the WF transmission. In the SIESTA calculations, the transmission peaks relative to the peaks obtained with the plane-wave calculation are systematically shifted toward lower energies. The problem can be overcome by enlarging the SIESTA basis; however, the convergence can be rather slow.

ACKNOWLEDGMENTS

The authors acknowledge support from the Danish Center for Scientific Computing through Grant No. HDW-1103-06. The Center for Atomic-Scale Materials Design is sponsored by the Lundbeck Foundation.

[1] N. Agrait, A. L. Yeyati, and J. M. van Ruitenbeek, Phys. Rep. **377**, 81 (2003), and references therein.
[2] A. Nitzan and M. A. Ratner, Science **300**, 1384 (2003).
[3] K. Stokbro, J. Taylor, M. Brandbyge, J.-L. Mozos, and P. Ordejón, Comput. Mater. Sci. **27**, 151 (2003).
[4] J. C. Cuevas, J. Heurich, F. Pauly, W. Wenzel, and G. Schön, Nanotechnology **14**, R29 (2003).
[5] V. M. García-Suárez, A. R. Rocha, S. W. Bailey, C. J. Lambert, S. Sanvito, and J. Ferrer, Phys. Rev. Lett. **95**, 256804 (2005).
[6] K. S. Thygesen and K. W. Jacobsen, Phys. Rev. Lett. **94**, 036807 (2005).
[7] M. Strange, K. S. Thygesen, and K. W. Jacobsen, Phys. Rev. B **73**, 125424 (2006).
[8] P. Delaney and J. C. Greer, Phys. Rev. Lett. **93**, 036805 (2004).
[9] K. S. Thygesen and A. Rubio, J. Chem. Phys. **126**, 091101 (2007).
[10] P. Darancet, A. Ferretti, D. Mayou, and V. Olevano, Phys. Rev. B **75**, 075102 (2007).
[11] S. Kurth, G. Stefanucci, C.-O. Almbladh, A. Rubio, and E. K. Gross, Phys. Rev. B **72**, 035308 (2005).
[12] P. Bokes and R. W. Godby, Phys. Rev. B **69**, 245420 (2004).
[13] M. Di Ventra, S. T. Pantelides, and N. D. Lang, Phys. Rev. Lett. **84**, 979 (2000).
[14] D. Q. Andrews, R. Cohen, R. P. Van Duyne, and M. A. Ratner, J. Chem. Phys. **125**, 174718 (2006).
[15] C. Toher and S. Sanvito, Phys. Rev. Lett. **98**, 056801 (2007).
[16] S. V. Faleev, F. Léonard, D. A. Stewart, and M. van Schilfgaarde, Phys. Rev. B **71**, 195422 (2005).
[17] K. Varga and S. T. Pantelides, Phys. Rev. Lett. **98**, 076804 (2007).
[18] J. Tomfohr and O. F. Sankey, J. Chem. Phys. **120**, 1542 (2004).
[19] P. Perdew, K. Burke, and M. Ernzerhof, Phys. Rev. Lett. **77**, 3865 (1996).
[20] Y. Meir and N. S. Wingreen, Phys. Rev. Lett. **65**, 2512 (1992).
[21] K. S. Thygesen, Phys. Rev. B **73**, 035309 (2006).
[22] F. Guinea, C. Tejedor, F. Flores, and E. Louis, Phys. Rev. B **28**, 4397 (1983).
[23] B. Hammer, L. B. Hansen, and J. K. Nørskov, Phys. Rev. B **59**, 7413 (1999); S. R. Bahn and K. W. Jacobsen, Rep. Sci. Res. Inst. **4**, 56 (2002); The DACAPO code can be downloaded at http://www.camp.dtu.dk/software.
[24] D. Vanderbilt, Phys. Rev. B **41**, 7892 (1990).
[25] K. S. Thygesen, L. B. Hansen, and K. W. Jacobsen, Phys. Rev. Lett. **94**, 026405 (2005); Phys. Rev. B **72**, 125119 (2005).
[26] K. S. Thygesen and K. W. Jacobsen, Chem. Phys. **319**, 111 (2005).
[27] J. M. Soler, E. Artacho, J. D. Gale, A. García, J. Junquera, P. Ordejón, and D. Sanchez-Portal, J. Phys.: Condens. Matter **14**, 2745 (2002).
[28] E. Artacho, D. Sánchez-Portal, P. Ordejón, A. García, and J. M. Soler, Phys. Status Solidi B **215**, 809 (1999).
[29] N. Troullier and J. L. Martins, Solid State Commun. **74**, 613 (1990).
[30] K. S. Thygesen and K. W. Jacobsen, Phys. Rev. B **72**, 033401 (2005).
[31] N. Nilius, T. M. Wallis, and W. Ho, Phys. Rev. Lett. **90**, 186102 (2003).
[32] A. Calzolari, C. Cavazzoni, and M. B. Nardelli, Phys. Rev. Lett. **93**, 096404 (2004).
[33] R. H. M. Smit, Y. Noat, C. Untiedt, N. D. Lang, M. C. van Hemert, and J. M. van Ruitenbeek, Nature (London) **419**, 906 (2002).
[34] C. Untiedt, D. M. Dekker, D. Djukic, and J. M. van Ruitenbeek, Phys. Rev. B **69**, 081401 (2004).
[35] J. M. Krans, C. J. Muller, I. K. Yanson, Th. C. M. Govaert, R. Hesper, and J. M. van Ruitenbeek, Phys. Rev. B **48**, 14721 (1993).
[36] S. K. Nielsen, Y. Noat, M. Brandbyge, R. H. M. Smit, K. Hansen, L. Y. Chen, A. I. Yanson, F. Besenbacher, and J. M. van Ruitenbeek, Phys. Rev. B **67**, 245411 (2003).
[37] J. Fernández-Rossier, D. Jacob, C. Untiedt, and J. J. Palacios, Phys. Rev. B **72**, 224418 (2005).
[38] J. J. Palacios, A. J. Pérez-Jiménez, E. Louis, and J. A. Vergés, Phys. Rev. B **64**, 115411 (2001).
[39] D. Djukic, K. S. Thygesen, C. Untiedt, R. H. M. Smit, K. W. Jacobsen, and J. M. van Ruitenbeek, Phys. Rev. B **71**, R161402 (2005).
[40] V. M. García-Suárez, A. R. Rocha, S. W. Bailey, C. J. Lambert, S. Sanvito, and J. Ferrer, Phys. Rev. B **72**, 045437 (2005).
[41] Y. García, J. J. Palacios, E. SanFabián, J. A. Vergés, A. J. Pérez-Jiménez, and E. Louis, Phys. Rev. B **69**, R041402 (2004).
[42] M. A. Reed, C. Zhou, C. J. Muller, T. P. Burgin, and J. M. Tour, Science **278**, 252 (1997).
[43] M. Tsutsui, Y. Teramae, S. Kurokawa, and A. Sakai, Appl. Phys. Lett. **89**, 163111 (2006).
[44] X. Xiao, B. Xu, and N. J. Tao, Nano Lett. **4**, 267 (2004).
[45] J. Ulrich, D. Esrail, W. Pontius, L. Venkataraman, D. Millar, and L. H. Doerrer, J. Phys. Chem. B **110**, 2462 (2006).
[46] S. Ghosh, H. Halimun, A. K. Mahapatro, J. Choi, S. Lodha, and D. Janes, Appl. Phys. Lett. **87**, 233509 (2005).
[47] F. Evers, F. Weigend, and M. Koentopp, Phys. Rev. B **69**, 235411 (2004).
[48] H. Kondo, H. Kino, J. Nara, T. Ozaki, and T. Ohno, Phys. Rev. B **73**, 235323 (2006).
[49] E. G. Emberly and G. Kirczenow, Phys. Rev. Lett. **91**, 188301 (2003).
[50] S.-H. Ke, H. U. Baranger, and W. Yang, J. Chem. Phys. **127**, 144107 (2007).
[51] Y. Xue, S. Datta, and M. A. Ratner, J. Chem. Phys. **115**, 4292 (2001).
[52] B. Xu and N. J. Tao, Science **301**, 1221 (2003).
[53] R. Stadler, K. S. Thygesen, and K. W. Jacobsen, Phys. Rev. B **72**, R241401 (2005).
[54] R. Stadler and K. W. Jacobsen, Phys. Rev. B **74**, 161405 (2006).
[55] T. Tada, M. Kondo, and K. Yoshizawa, J. Chem. Phys. **121**, 8050 (2004).
[56] S. Hou, J. Zhang, R. Li, J. Ning, R. Han, Z. Shen, X. Zhao, Z. Xue, and Q. Wu, Nanotechnology **16**, 239 (2005); S. Hou, J. Ning, Z. Shen, X. Zhao, and Z. Xue, Chem. Phys. **327**, 1 (2006); R. Li, S. Hou, J. Zhang, Z. Qian, Z. Shen, and X. Zhao, J. Chem. Phys. **125**, 194113 (2006).
[57] A. J. Perez–Jimenez, J. Phys. Chem. B **109**, 10052 (2005).
[58] X. Wu, Q. Li, J. Huang, and J. Yang, J. Chem. Phys. **123**, 184712 (2005).
[59] Q. Li, X. Wu, J. Huang, and J. Yang, Ultramicroscopy **105**, 293 (2005).
[60] M. Brandbyge, J. L. Mozos, P. Ordejón, and K. Stokbro, Phys. Rev. B **65**, 165401 (2002).

Paper III

VIP Gold Catalysis

DOI: 10.1002/ange.200801479

Trends in the Catalytic CO Oxidation Activity of Nanoparticles**

*Hanne Falsig, Britt Hvolbæk, Iben S. Kristensen, Tao Jiang, Thomas Bligaard, Claus H. Christensen, and Jens K. Nørskov**

Although extended gold surfaces are generally considered chemically inert[1,2] nanosized (< 5 nm) gold particles can be very effective catalysts for a number of oxidation reactions.[3–17] There are reports of similar size effects for silver catalysts.[18,19] The origin of the nanoeffects in the catalytic properties of these metals is widely debated,[15] and no consensus has been reached. Based on a set of density functional theory calculations of the full reaction pathway for CO oxidation over extended surfaces as well as over small nanoparticles of a number of metals, we show that although platinum and palladium are the most active catalysts for extended surfaces at high temperatures, gold is the most active for very small particles at low temperature. The calculations capture the special catalytic properties of nanosized particles observed experimentally, which allows the origin of the effect to be analyzed.

Herein, we focus on intrinsic metal effects; that is, we do not include additional possible effects that involve the support. It is not that such effects may not be important,[5,20,21] but it is useful to first establish the intrinsic metal effects,[15] in particular as it has been shown experimentally that nanostructured gold with no support is also catalytically active.[22,23] The key feature of our analysis is that we compare catalytic activities of different transition and noble metals for one specific reaction, the CO oxidation.

The CO oxidation reaction on close-packed fcc(111) surfaces was considered initially, which will give a dominant contribution to the total catalytic rate over large metal particles. We consider the following elementary reactions:

$$CO + * \rightleftharpoons CO* \quad \text{(R1)}$$

$$O_2 + * \rightleftharpoons O_2* \quad \text{(R2)}$$

$$O_2* + * \rightleftharpoons 2\,O* \quad \text{(R3)}$$

$$O* + CO* \rightleftharpoons CO_2 + 2* \quad \text{(R4)}$$

For the metals we consider herein, Reactions (R1) and (R2) are unactivated and fast, and we assume that these two reactions are in equilibrium. This means that we are limited to temperatures high enough that desorption is also fast. The possible formation of an oxide layer on the more reactive metals is neglected.

The forward and reverse rate constants of the Reactions (R3) and (R4) are given by $k_i = \nu_i \exp[-\Delta G_{ai}/kT] = \nu_i \exp[-(E_{ai} - T\Delta S_{ai})/kT]$, where ν_i is a prefactor, E_{ai} is the activation energy, k is the Boltzmann constant, and T is the absolute temperature. The activation energies are $E_a = \max(E_{TS} - E_{IS}, 0)$ where E_{IS} is the initial state energy and E_{TS} is the transition-state energy. ΔS_{ai} is the entropy difference between the transition state and the initial state. The entropy of adsorbed species are assumed to be zero, and the gas-phase entropies are taken from Ref. [24]. The adsorption energies of the different species E_{CO}, E_{O_2}, and E_O and the transition state energies are given with respect to the gas-phase molecules.

Assuming the prefactors and adsorption entropies are independent of the metal, there are five metal-dependent parameters determining the kinetics: E_{CO}, E_{O_2}, E_O, E_{TS3}, and E_{TS4}. The transition-state energies are, however, found to scale linearly with the adsorption energies, as shown for E_{TS3} and E_{TS4} in Figure 1a and b. Such Brønsted–Evans–Polanyi (BEP) relations are found quite generally for surface reactions.[25] Furthermore, the O_2 adsorption energy scales with the O adsorption energy (Figure 1c). This means that the adsorption energies E_{CO} and E_O can be viewed, to a first approximation, as the only independent variables characterizing the metal in the microkinetic model. Owing to the low number of elementary reactions, it is possible to find an analytical solution for this microkinetic model. Herein, we use instead the more general method of a so-called Sabatier analysis to find an upper bound to the overall reaction rate.[26]

The Sabatier rate[26] is the rate the reaction will have if all coverages are optimum for each elementary reaction step. Such conditions may not be obtainable in reality, but the Sabatier rate still provides an exact upper bound to the steady-state rate under any reaction conditions. The Sabatier rate is also an upper bound on the rate when islanding is included, as that will decrease the number of possible reaction centers to the length of the boundary between different phases.[27] The Sabatier rate thus forms a good measure of the intrinsic ability of a given metal surface to catalyze the reaction in question. The metal with the highest Sabatier rate is taken herein as being the best catalyst.

[*] Dr. B. Hvolbæk, I. S. Kristensen, T. Jiang, Dr. T. Bligaard, Prof. J. K. Nørskov
Center for Atomic-scale Materials Design, Department of Physics, Technical University of Denmark, DK-2800 Lyngby (Denmark)
Fax: (+45)4593-2399
E-mail: norskov@fysik.dtu.dk
H. Falsig, Prof. C. H. Christensen
Center for Sustainable and Green Chemistry, Department of Chemistry, Technical University of Denmark
DK-2800 Lyngby (Denmark)

[**] The Center for Sustainable and Green Chemistry is supported by the Danish National Research Foundation, and the Center for Atomic-scale Materials Design is supported by the Lundbeck Foundation. In addition we thank the Danish Research Council for the Technical Sciences and the NABIIT program for financial support, and Danish Center for Scientific Computing for computer time.

Supporting information for this article is available on the WWW under http://dx.doi.org/10.1002/anie.200801479.

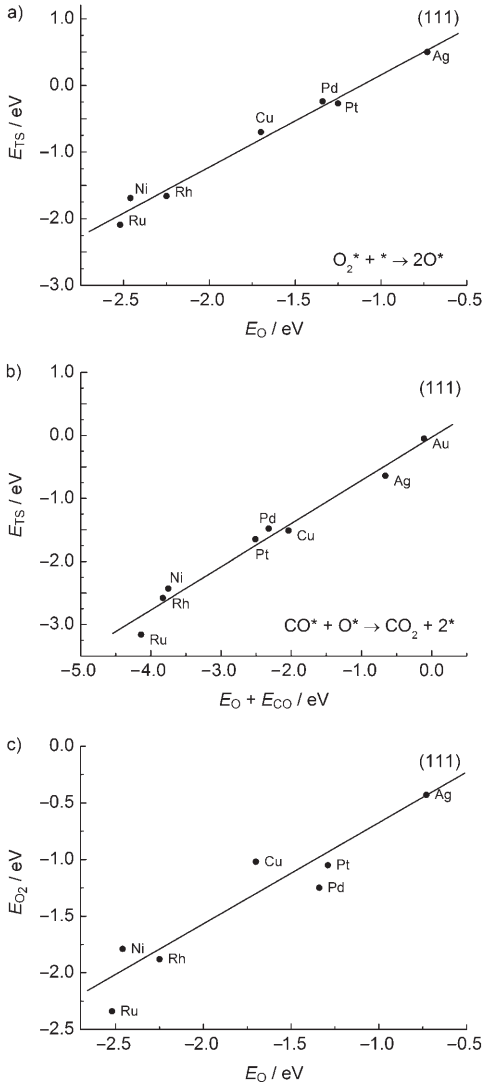

Figure 1. The BEP and scaling relations for different close-packed fcc(111)-surfaces. a) Calculated transition-state energies for O_2 dissociation (R3) as a function of oxygen adsorption energy. $E_{TS3} = 1.39\,E_O + 1.56$ eV. b) Calculated transition-state energies for adsorbed CO reacting with adsorbed O (R4) as a function of the sum of the O and CO adsorption energies. $E_{TS4} = 0.70(E_O + E_{CO}) + 0.02$ eV. c) The scaling of the O_2 adsorption energy with the oxygen adsorption energy $E_{O_2} = 0.89E_O + 0.17$ eV. For Pt(111,) the calculated reaction barrier $E_a = E_{TS} - (E_{CO} + E_O)$ for $CO^* + O^* \rightleftarrows CO_2 + 2^*$ is 0.85 eV, in good agreement with calculations.[28,29]

The rate of reaction for (R3) and (R4) are maximized if the reverse reactions are neglected. The Sabatier rate is therefore calculated from the forward rates:

$$r_3^+ = \theta_{O_2}\theta_* k_3^+ = \theta_{O_2}\theta_* \nu_3 \exp[-(E_{a3} - T\,\Delta S_{a3})/k\,T] \quad (1)$$

$$r_4^+ = \theta_O\theta_{CO}\, k_4^+ = \theta_O\theta_{CO}\, \nu_4 \exp[-(E_{a4} - T\,\Delta S_{a4})/k\,T] \quad (2)$$

where θ_{O_2} is the coverage of adsorbed oxygen molecules, θ_O is the coverage of adsorbed atomic oxygen, θ_{CO} is the coverage of adsorbed CO molecules, and θ_* is the coverage of free sites of the surface. The coverages will depend on the reaction conditions, temperature, reactant pressures, and conversion.

For the present case, the optimum coverages are found by first neglecting the coverage of atomic oxygen. Still assuming that (R1) and (R2) are in equilibrium, this gives:

$$\theta_*^{max} = \frac{1}{1 + K_1\,p(CO) + K_2\,p(O_2)} \quad (3)$$

where K_1 and K_2 are the equilibrium constants for (R1) and (R2), and $p(CO)$ and $p(O_2)$ are the partial pressures of CO and O_2. The optimum coverages of CO and O_2 have similar expressions, namely $\theta_{CO}^{max} = K_1 p(CO)\theta_*$ and $\theta_{O_2}^{max} = K_2 p(O_2)\theta_*$.

The Sabatier rates of each of the Reactions (R3) and (R4) are found by using the forward rates from (1) and (2) with the coverages of θ^{max}, θ_{CO}^{max} and $\theta_{O_2}^{max}$ from (3), and the coverage of θ_O^{max} set to one.

$$r_3^{S\,max} = k_3^+ \theta_{O_2}^{max} \theta_*^{max} \quad (4)$$

$$r_4^{S\,max} = k_4^+ \theta_{CO}^{max} \theta_O^{max} = k_4^+ \theta_{CO}^{max} \quad (5)$$

The Sabatier rate of forming CO_2 is determined by the lowest of the Sabatier rates of Reaction (R3) and (R4):

$$r_S = \min\{2\,r_3^{S\,max},\, r_4^{S\,max}\} \quad (6)$$

where the factor of 2 stems from the stoichiometric number for (R3).

Figure 2 shows a contour plot of the Sabatier activity over close-packed surfaces. The Sabatier rate is calculated at $T = 600$ K, $P_{O_2} = 0.33$ bar and $P_{CO} = 0.67$ bar, corresponding to high-temperature CO oxidation conditions. The two-dimensional volcano plots show that, of the elemental metals, platinum and palladium are closest to the top. This agrees well with experimental evidence.[30] Platinum and palladium are

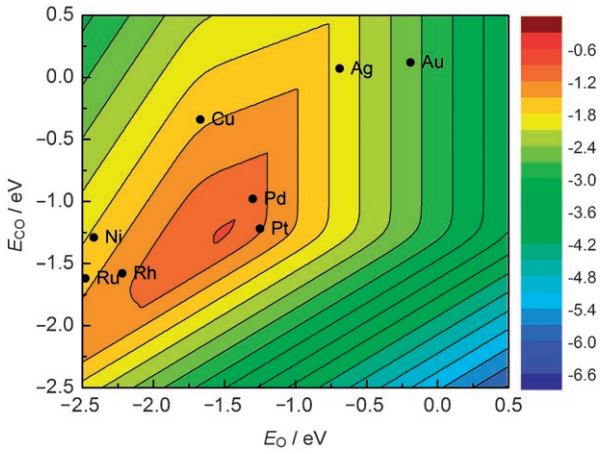

Figure 2. Contour plot of the Sabatier activity $A_S = k\,T \ln[r_S/\nu]$ over close-packed surfaces as a function of E_{CO} and E_O (ν is set to kT/h) under high-temperature conditions ($T = 600$ K, $P_{O_2} = 0.33$ bar, and $P_{CO} = 0.67$ bar). The values for different elemental metals can be taken from their indicated positions.

excellent CO oxidation catalysts, used for example in car exhaust after-treatment. This result is completely in line with DFT calculations and kinetic modeling by Grabow et al.[31] showing that at low temperatures, platinum without strain has a higher activity than either compressed (weaker bond energies) or expanded (stronger bond energies) platinum surfaces.

The reactivity of nanoparticles was then investigated. One important feature of nanoparticles is that the relative fraction of low-coordinate corner atoms to surface atoms is very large.[15,32] We concentrate herein on the reactivity of corner atoms, and model these by carrying out calculations for metal clusters containing twelve atoms, in the structure shown as inserts in Figure 3. All the twelve atoms in the cluster are held fixed with a lattice constant corresponding to the bulk value to mimic a geometrically constrained corner of a larger cluster, such as those in the range 2–5 nm studied experimentally. The calculations are thus more intended to model a general corner site on nanoparticles than specifically a twelve-atom cluster, as such small clusters will have much larger structural flexibility.[33]

It turns out that adsorption is considerably more exothermic on the twelve-atom clusters than on the close-packed surfaces. This makes it important to include another elementary reaction, as the coverage of molecular O_2 may be large enough such that an associative mechanism[34] may be important:

$$O_2{*} + CO{*} \rightleftharpoons CO_2 + O{*} + {*} \qquad \text{(R5)}$$

For the (111) surfaces, the weak bonding of O_2 combined with the reaction barrier for the process makes it unimportant for platinum[27] and less reactive metals.[35]

As for the fcc(111) surface, correlations between the transition state energies, E_{TS3}, E_{TS4}, and E_{TS5}, and the binding energies, E_O and E_{CO}, are found for the twelve-atom cluster. A scaling between E_{O_2} and E_O is also found. These relations are shown in Figure 3. The linear relations are similar to those of the close-packed surfaces (Figure 1), except that the adsorption energy axis has shifted. The adsorption energy of both CO and O are substantially more negative (exothermic adsorption) on the corner sites than on the close packed surfaces; compare for example, the adsorption energy of O on the (111) surfaces to those on the twelve-atom cluster: on the latter the bond is stronger by of the order 0.5 eV. The same trend is seen for molecular CO adsorption.

The expressions for the optimum coverages and the Sabatier rate for (R3) and (R4) are the same as for the fcc(111) surface. For (R5), the Sabatier rate is:

$$r_5^{S\max} = k_5^{+}\theta_{CO}^{\max}\theta_{O_2}^{\max} \qquad (7)$$

Both Reaction (R3) and (R5) dissociate O_2, and can be followed by Reaction (R4) creating CO_2. The Sabatier activity is therefore given by:

$$r_S = \max\{2\min\{r_5^{S\max}, r_4^{S\max}\}, \min\{2r_3^{S\max}, r_4^{S\max}\}\} \qquad (8)$$

Figure 4 shows the contour plot of the Sabatier activity,

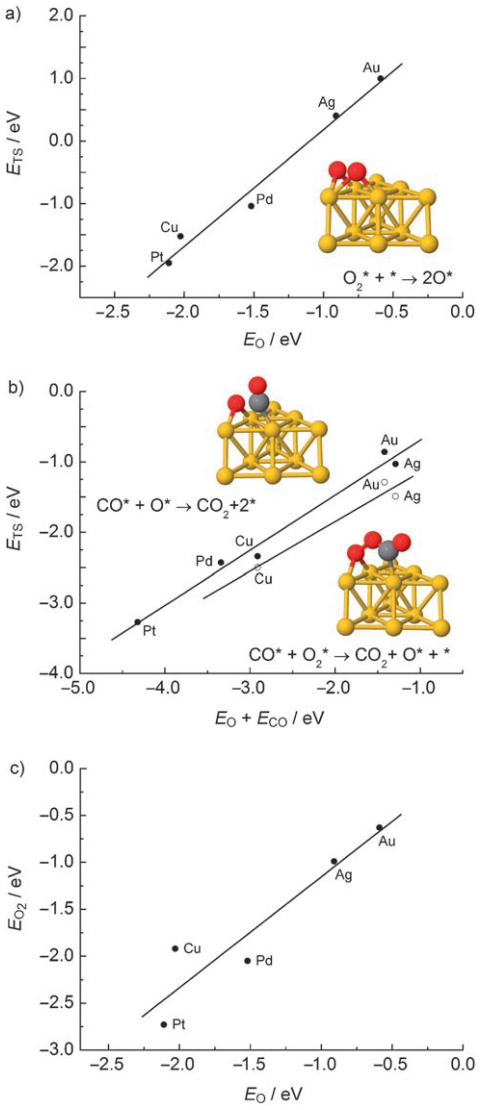

Figure 3. The BEP relations and scaling relation for different twelve-atom clusters. a) Calculated transition-state energies for O_2 dissociation (R3) as a function of oxygen adsorption energy. $E_{TS3} = 1.87\,E_O + 2.04$ eV. b) Calculated transition-state energies for adsorbed CO reacting with adsorbed O (R4) and O_2 (R5) as a function of the sum of the O and CO adsorption energies. $E_{TS4} = 0.78\text{-}(E_O + E_{CO}) + 0.09$ eV and $E_{T3S5} = 0.70(E_O + E_{CO}) - 0.44$ eV. c) The scaling of the O_2 adsorption energy with the O adsorption energy $E_{O_2} = 1.18\,E_O + 0.03$ eV. Transition states for the reactions on the Au_{12} cluster are shown as inserts.

$A_S = kT\ln[r_S/\nu]$. In this case, gold is closest to the top, followed by palladium and silver.

The results in Figure 2 and Figure 4 are in good agreement with available experimental observations.[3,32] It shows that the relative activities of different metals can be theoretically estimated, and it provides a clear picture of the catalyst properties determining the best catalysts in terms of the adsorption energies of the intermediates. The volcano plots of Figure 2 and Figure 4 can be viewed as an illustration of the Sabatier principle, with the important new feature that we know which adsorption energy that provides the optimum

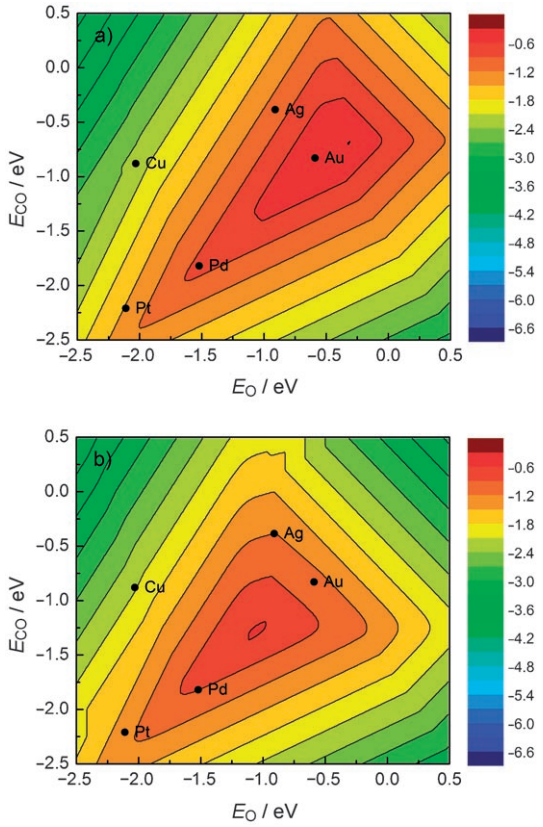

Figure 4. Contour plot of the Sabatier rate as a function of the CO and O adsorption energies on the twelve-atom clusters. The values for some elemental metals are shown. a) The activity under typical experimental conditions for CO oxidation by gold nanoparticles (T=273 K, P_{O_2}=0.21 bar, and P_{CO}=0.01) and b) the activity under high-temperature conditions (T=600 K, P_{O_2}=0.33 bar, and P_{CO}=0.67 bar).

catalyst. The position of the maximum in terms of adsorption energies depends slightly on the structure, which is related to the fact that the relationship between adsorption energy and activation energy is somewhat structure dependent. More importantly, it can be seen that the metals corresponding to a particular adsorption energy shift substantially depending on the coordination number of the metal atom. This is true for all the metals considered, and it is the dominant reason for gold becoming the best elemental catalyst for the low-coordinate sites. The shift is of the same order of magnitude as the difference between neighboring metals in the periodic table, explaining why it appears as if the top of the volcano has shifted by a little less than one place to the right in the periodic table from Figure 2 to Figure 4.

Comparing the volcanoes in Figure 2 and Figure 4, it is clear that for gold, the corner atoms will dominate over the close-packed surfaces for even quite large particles, as the value of r_S is many orders of magnitude larger in this case. For platinum, on the other hand, the difference is only about an order of magnitude. It should be noted that even for platinum, small particles could still be more active than larger ones, but only because the surface area per mass of catalyst is larger (scaling as d^{-1}).

The present analysis suggests that the more noble metals move to the maximum in the reactivity volcano when lower-coordinated metal atoms serve as active sites for the reaction. It suggests that similar results could be found for other reactions. For oxidation reactions, the best extended surface catalysts are already quite noble: platinum and palladium, and gold is the next, less reactive metal. For reactions involving less reactive molecules, such as N_2, we would expect that the best nanoparticle catalysts would not be gold but metals just to the right in the periodic table of the most active metals (ruthenium, iron) for this reaction, for example, cobalt or nickel. It is therefore possible that pronounced nanoeffects in catalysis is not restricted to gold.

In summary, we have modeled the special catalytic properties of nanosized particles observed experimentally, and analyzed the origin of the effect. The ability of the metal atoms to activate reactants change substantially as the coordination number of the active metal site is reduced at corners of metal particles. This model supports the hypothesis that part of the observed reactivity of gold nanoparticles is independent of the substrate.

Received: March 23, 2008
Published online: May 21, 2008

Keywords: carbon monoxide · density functional calculations · gold · heterogeneous catalysis · nanostructures

[1] D. T. Wickham, D. H. Parker, G. N. Kastanas, M. A. Lazaga, B. E. Koel, *Prepr. Am. Chem. Soc. Div. Pet. Chem.* **1992**, *37*, 1034.
[2] B. Hammer, J. K. Nørskov, *Nature* **1995**, *376*, 238–240.
[3] M. Haruta, T. Kobayashi, H. Sano, N. Yamada, *Chem. Lett.* **1987**, 405–408.
[4] M. Valden, X. Lai, D. W. Goodman, *Science* **1998**, *281*, 1647–1650.
[5] G. C. Bond, D. T. Thomson, *Catal. Rev. Sci. Eng.* **1999**, *41*, 319–388.
[6] M. A. P. Dekkers, M. J. Lippits, B. E. Nieuwenhuys, *Catal. Today* **1999**, *54*, 381.
[7] S. Carrettin, P. McMorn, P. Johnston, K. Griffin, G. J. Hutchings, *Chem. Commun.* **2002**, 696–697.
[8] S. Schimpf, M. Lucas, C. Mohr, U. Rodemerck, A. Brückner, J. Radnik, H. Hofmeister, P. Claus, *Catal. Today* **2002**, *72*, 63–78.
[9] S. Carrettin, P. McMorn, P. Johnston, K. Griffin, C. J. Kiely, G. A. Attard, G. J. Hutchings, *Top. Catal.* **2004**, *27*, 131–136.
[10] R. Meyer, C. Lemire, S. Shaikhutdinov, H. J. Freund, *Gold Bull.* **2004**, *37*, 72–133.
[11] A. Abad, P. Concepcion, A. Corma, H. Garcia, *Angew. Chem.* **2005**, *117*, 4134–4137; *Angew. Chem. Int. Ed.* **2005**, *44*, 4066–4069.
[12] A. C. Gluhoi, N. Bogdanchikova, B. E. Nieuwenhuys, *J. Catal.* **2005**, *229*, 154–162.
[13] M. D. Hughes et al., *Nature* **2005**, *437*, 1132–1135.
[14] T. A. Nijhuis, M. Makkee, J. A. Moulijn, B. M. Weckhuysen, *Ind. Eng. Chem. Res.* **2006**, *45*, 3447–3459.
[15] a) T. V. W. Janssens, B. S. Clausen, B. Hvolbæk, H. Falsig, C. H. Christensen, T. Bligaard, J. K. Nørskov, *Top. Catal.* **2007**, *44*, 15–26; b) N. Lopez, T. V. W. Janssens, B. S. Clausen, Y. Xu, M. Mavrikakis, T. Bligaard, J. K. Nørskov, *J. Catal.* **2004**, *223*, 232–235.
[16] C. H. Christensen, B. Jørgensen, J. Rass-Hansen, K. Egeblad, R. Madsen, S. K. Klitgaard, S. M. Hansen. M. R. Hansen, H. C.

Andersen, A. Riisager, *Angew. Chem.* **2006**, *118*, 4764 – 4767; *Angew. Chem. Int. Ed.* **2006**, *45*, 4648 – 4651.
[17] R. Burch, *Phys. Chem. Chem. Phys.* **2006**, *8*, 5483 – 5500.
[18] M. J. Lippits, A. C. Gluhoi, B. E. Nieuwenhuys, *Top. Catal.* **2007**, *44*, 159 – 165.
[19] L. Gang, B. G. Anderson, J. van Grondelle, R. A. van Santen, *Appl. Catal. B* **2003**, *40*, 101 – 110.
[20] M. Haruta, *Catal. Today* **1997**, *36*, 153 – 166.
[21] B. Hammer, *Top. Catal.* **2006**, *37*, 3 – 16.
[22] C. Xu, J. Su, X. Xu, P. Liu, H. Zhao, F. Tian, Y. Ding, *J. Am. Chem. Soc.* **2007**, *129*, 42 – 43.
[23] B. Jürgens, C. Kübel, C. Schultz, T. Nowitzki, V. Zielasek, J. Biener, M. M. Biener, A. V. Hamza, M. Bäumer, *Gold Bull.* **2007**, *40*, 142 – 148.
[24] P. Atkins, J. de Paula, *J. Physical Chemistry* , 8th ed. Oxford University Press, Oxford, **2006**.
[25] J. K. Nørskov et al., *J. Catal.* **2002**, *209*, 275 – 278.
[26] T. Bligaard, J. K. Nørskov, S. Dahl, J. Matthiesen, C. H. Christensen, J. Sehested, *J. Catal.* **2004**, *224*, 206 – 217.
[27] J. Wintterlin, S. Völkening, T. V. W. Janssens, T. Zambelli, G. Ertl, *Science* **1997**, *278*, 1931 – 1933.
[28] Z.-P. Liu, P. Hu, *Top. Catal.* **2004**, *28*, 71 – 78.
[29] A. Eichler, J. Hafner, *Surf. Sci.* **1999**, *433*, 58 – 62.
[30] B. E. Nieuwenhuys, *Surf. Rev. Lett.* **1996**, *3*, 1869 – 1888.
[31] L. Grabow, Y. Xu, M. Mavrikakis, *Phys. Chem. Chem. Phys.* **2006**, *8*, 3369 – 3374.
[32] A. Carlsson, A. Puig-Molina, T. V. W Janssens, *J. Phys. Chem. B* **2006**, *110*, 5286 – 5293.
[33] G. Mills, M. S. Gordon, H. Metiu, *J. Chem. Phys.* **2003**, *118*, 4198 – 4205.
[34] Z.-P. Liu, P. Hu, A. Alavi, *J. Am. Chem. Soc.* **2002**, *124*, 14770 – 14779.
[35] L. M. Molina, B. Hammer, *Phys. Rev. B* **2004**, *69*, 155424.

Paper IV

IOP PUBLISHING JOURNAL OF PHYSICS: CONDENSED MATTER

J. Phys.: Condens. Matter **20** (2008) 374101 (4pp) doi:10.1088/0953-8984/20/37/374101

Comparative study of anchoring groups for molecular electronics: structure and conductance of Au–S–Au and Au–NH_2–Au junctions

I S Kristensen, D J Mowbray, K S Thygesen and K W Jacobsen

Center for Atomic-scale Materials Design (CAMD), Department of Physics, Building 307, Technical University of Denmark, DK-2800 Kongens Lyngby, Denmark

Received 29 February 2008, in final form 4 June 2008
Published 26 August 2008
Online at stacks.iop.org/JPhysCM/20/374101

Abstract

The electrical properties of single-molecule junctions, consisting of an organic molecule coupled to metal electrodes, are sensitive to the detailed atomic structure of the molecule–metal contact. This, in turn, is determined by the anchoring group linking the molecule to the metal. With the aim of identifying and comparing the intrinsic properties of two commonly used anchoring groups, namely thiol and amine groups, we have calculated the atomic structure and conductance traces of different Au–S–Au and Au–NH_2–Au nanojunctions using density functional theory (DFT). Whereas NH_2 shows a strong structural selectivity towards atop-gold configurations, S shows large variability in its bonding geometries. As a result, the conductance of the Au–NH_2–Au junction is less sensitive to the structure of the gold contacts than the Au–S–Au junction. These findings support recent experiments which show that amine-bonded molecules exhibit more well-defined conductance properties than do thiol-bonded molecules.

(Some figures in this article are in colour only in the electronic version)

1. Introduction

A detailed, quantitative understanding of the electron transport properties of molecular junctions composed of a single molecule between two metallic electrodes is an essential step for the development of molecular electronics. Experiments on single-molecule junctions often suffer from a large variability in the measured conductance, probably originating from details beyond experimental control. In the case of molecules linked to metal electrodes via a sulfur atom, that is, through thiol linking groups, the conductance shows a strong junction to junction variation within the same experiment [1], as well as between different sets of experiments [2–5]. More recent experimental and theoretical works suggest that the use of amine (NH_2) anchoring groups yields junctions with a more well-defined conductance [6].

Knowledge about the atomistic contact geometry must be obtained through detailed comparisons between experimental and theoretical results. For certain types of systems, calculations based on density functional theory (DFT) agree well with experiments and yield valuable insights. Such systems include atomic wires [7, 8] and metal contacts with small chemisorbed molecules [9, 10]. Even though these types of systems are not directly relevant for molecular electronics, they are important for developing our understanding of electron transport at the nanoscale, and as such they can be considered as simple benchmark systems. For larger and more complex molecular junctions, such as benzene-dithiolate, rather large disagreements have been observed, both between individual experimental results and in comparison with theory [6, 11, 12].

In this paper, we compare the transport properties of the thiol and amine anchoring groups by performing DFT calculations for both structure and conductance of Au–S–Au and Au–NH_2–Au nanojunctions. In the case of sulfur we consider two different geometries: a top–top configuration where the sulfur atom is bonded to a single gold atom on each side, and a top–hollow configuration where sulfur is bonded to a single gold atom on one side and three gold atoms on the other side. We simulate a break junction experiment by calculating the conductance as the contact is pulled apart, and

we find a strong dependence on the local atomic structure. In contrast to sulfur, we find that the amine group always binds to a single Au atom on each side of the junction. We consider two junction geometries: a symmetric top–top configuration similar to the one found for S, and an asymmetric top–top configuration. The pronounced structural selectivity of the amine group leads to very similar conductance traces for the two configurations.

2. Method

The DFT calculations have been performed using the plane-wave-based pseudopotential code DACAPO [13][1]. The molecular contacts are described in a supercell containing the sulfur atom or amine group sandwiched between two four-atom Au pyramids attached to Au(111) surfaces. We include six Au atomic layers each containing 3×3 atoms in the surface plane. Periodic boundary conditions are imposed in all directions. We use a 4×4 Monkhorst–Pack grid to sample the Brillouin zone in the surface plane both for the total energy and the transport calculations. The structures are optimized by relaxing the position of the anchoring group and the pyramids while keeping the rest of the Au atoms fixed in the bulk positions. Before calculating the transmission function, the DFT eigenstates are transformed into a set of localized Wannier-like basis functions [14]. This transformation makes it possible to partition the system into a central region (containing the contact region of the junction) and a left and right lead (bulk gold). In this way, the Landauer–Bütikker conductance, G, can be calculated from the Green's function of the central region, G_C, according to the formula [15, 16]

$$G = G_0 \,\mathrm{Tr}[G_C \Gamma_L G_C^\dagger \Gamma_R]|_{\varepsilon=\varepsilon_F}, \qquad (1)$$

where the trace runs over all localized basis functions in the central region and $G_0 = 2e^2/h$ is the conductance quantum. The central region Green's function is calculated from

$$G_C(\varepsilon) = ((\varepsilon + i0^+)S_C - H_C^{KS} - \Sigma_L(\varepsilon) - \Sigma_R(\varepsilon))^{-1}, \qquad (2)$$

where S_C and H_C^{KS} are the overlap matrix and Kohn–Sham Hamiltonian matrix of the central region in the localized basis, and $\Sigma_{L/R}$ are lead self-energies. The coupling strengths are given by $\Gamma_{L/R} = i(\Sigma_{L/R} - \Sigma_{L/R}^\dagger)$. More details on the Wannier transport scheme may be found in [17].

3. Results

To gain insight into the possible structures of an Au–S/NH_2–Au contact, we have made successive relaxations of the system as the distances between the outermost surface layers is varied, thereby simulating the contact formation in a break junction experiment. When increasing the distance between the two Au(111) surfaces, all atomic distances between them have been proportionally increased and subsequently relaxed. In the following we concentrate on two different structures for the gold contacts: (i) two opposing pyramids and (ii) a pyramid opposing a pyramid with the tip atom removed, with geometries as shown schematically in figures 1 and 4, respectively. For contact (i) both S and NH_2 bind symmetrically to the tip atoms of the two pyramids. We refer to these as (symmetric) top–top configurations. For contact (ii), S adopts the site of the removed Au tip atom, thus forming a top–hollow configuration. However, NH_2 forms a bridge between the pyramid tip atom and one of the three gold atoms forming the pyramid base (the asymmetric top–top configuration). We note that the sulfur top–top and top–hollow configurations correspond to the configurations proposed in [18]. We also mention that molecular dynamics simulations of sulfur-contaminated gold contacts frequently result in Au–S–Au contacts similar to the ones studied here [19].

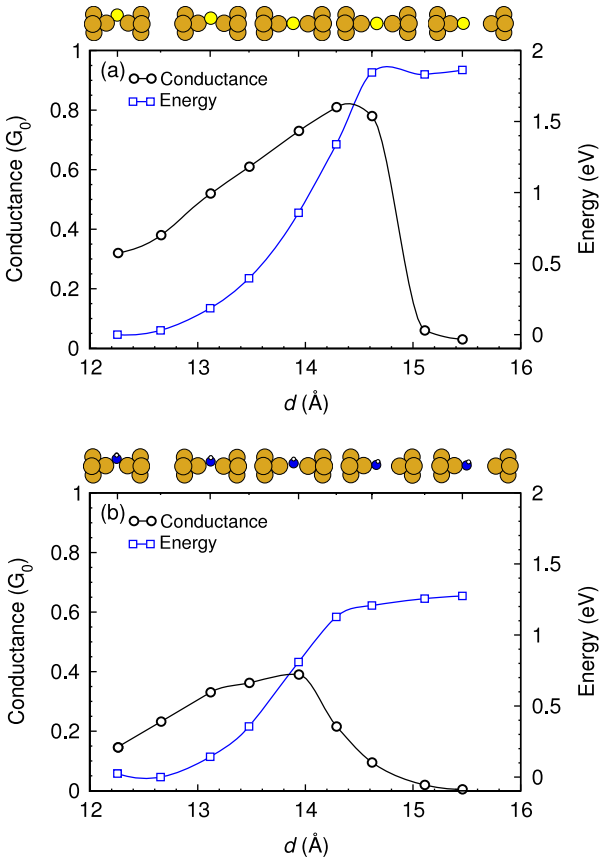

Figure 1. Conductance (circles) and total energy (squares) for (a) Au–S–Au and (b) Au–NH_2–Au nanojunctions in the symmetric top–top configuration as a function of distance between the outermost Au(111) surfaces. The breaking forces are approximately 1.8 and 1.0 eV Å^{-1}, respectively. The zero points of the energy have been chosen arbitrarily. Notice that for both systems the conductance increases as the contact is pulled apart due to the linearization of the contact geometry.

Consider first the sulfur top–top structure, shown in figure 1(a). For short distances between the Au(111) surfaces, the S atom is situated at the side of the contact bridging the two Au tip atoms. As the contact is pulled apart, the sulfur atom moves into the contact, resulting in a linear contact configuration. Interestingly, the conductance increases from

[1] The exchange and correlation part is treated using a PW91 energy functional [20]. The Kohn–Sham (KS) eigenstates are expanded in plane waves with a kinetic energy less than 25 Ryd.

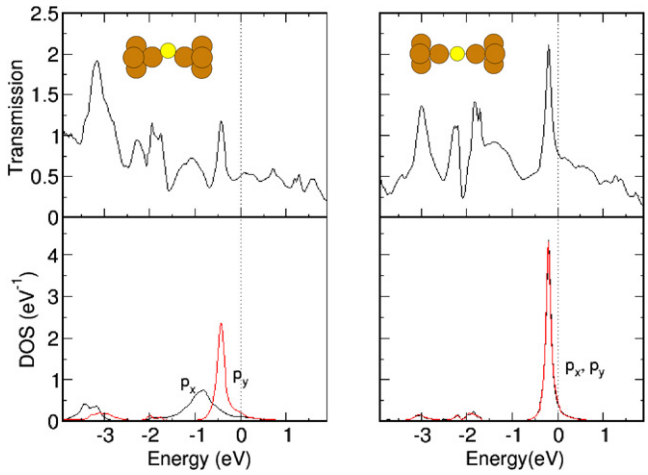

Figure 2. Total transmission (upper panels) and projected density of states (PDOS) for the p-orbitals perpendicular to the contact axis (lower panels) for a contracted (left) and stretched (right) Au–S–Au contact. The center of both the p-orbitals moves closer to the Fermi level as the contact is elongated. The p_x-orbital (pointing towards the sulfur atom) is completely quenched for the contracted contact due to the coupling to the gold s-band. Both effects result in the observed increase in the conductance as the contact is stretched.

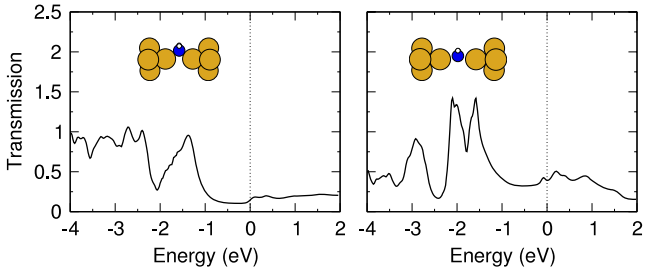

Figure 3. Total transmission for a contracted (left) and stretched (right) Au–NH_2–Au contact. Notice that the transmission function varies little around the Fermi level as compared to the transmission function of the Au–S–Au contact shown in figure 2.

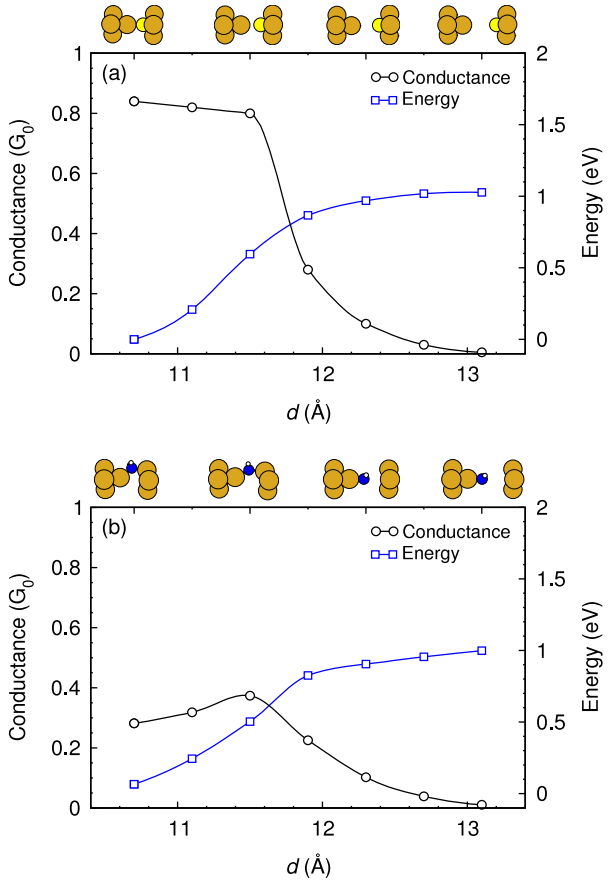

Figure 4. Conductance (circles) and total energy (squares) for (a) Au–S–Au and (b) Au–NH_2–Au nanojunctions in the top–hollow and asymmetric top–top configurations, respectively, as a function of distance between the outermost Au(111) surfaces. The breaking forces are approximately 1.0 and 0.9 eV Å^{-1}, respectively.

$0.3G_0$ to $0.8G_0$ as the contact is pulled apart, demonstrating how small changes in the local atomic structure of the contact can lead to significant changes in the conductance of the junction. In general, such behavior is characteristic of the phase-coherent transport regime and is a direct manifestation of the wave nature of the charge carriers.

The observed increase in conductance as the contact is stretched is mainly due to the sulfur p_x-orbital (the x axis is vertical on all plots of the structure). To show this, we compare in figure 2 the transmission function and the projected density of states (PDOS) for the p_x-and p_y-orbitals at two different elongations of the contact. The peak in the transmission function just below the Fermi level is clearly correlated to the PDOS of the p_x-and p_y-orbitals. As the contact is stretched, the peak grows in intensity by a factor of two and is shifted closer to E_F. The increase in intensity is due to the opening of the p_x channel. For the contracted configuration the PDOS of p_x is broadened and shifted downwards by the coupling to the gold s-band. In the linear configuration, this coupling is prohibited by symmetry and p_x and p_y are degenerate. Besides the contribution from the p_x- and p_y-orbitals, the total transmission also includes a background contribution from the p_z-orbital pointing in the transport direction. However, this background contribution stays almost constant when the system is elongated. More generally, the sharp peaks in the transmission function very close to E_F makes the conductance sensitive to changes in the surrounding potential.

Next, we consider the symmetric NH_2 top–top structure shown in figure 1(b). The structural change upon pulling is rather similar to the sulfur junction. However, the conductance is somewhat lower and increases from about $0.2G_0$ to $0.4G_0$. We note that the drop in conductance when the contact breaks is less abrupt than for the sulfur junction. This is due to the weakness of the Au–NH_2 bond as compared to the Au–S bond, which implies that the gold pyramids retract less when the NH_2 junction breaks. More generally, the continuous drop in conductance upon rupture is an artifact of the finite size of the supercell which prohibits a large retraction of the contact when it breaks. The transmission functions of the NH_2 junction for two different elongations are shown in figure 3. In comparison with the sulfur junction, the transmission functions of the amine junction show little variation around E_F. Thus small changes in the nearby electron potential due

to changes in the gold contacts should have little effect on the conductance.

In the Au–S–Au top–hollow configuration, the sulfur atom occupies the site of the removed tip atom of one of the two pyramids, as shown in the schematics of figure 4(a). When the junction is pulled, no major rearrangements of the atoms occur and the conductance stays rather constant around $0.8G_0$ until the contact breaks. We notice that the conductance trace of the top–hollow configuration is distinctly different from the trace of the top–top configuration in figure 1(a). In particular, the conductance does not increase upon pulling but stays almost constant until the breaking point.

The calculated conductance trace of the asymmetric NH_2 top–top configuration (the same Au contact geometry as for the sulfur top–hollow) is shown in figure 4(b). The conductance increases from $0.3G_0$ to $0.4G_0$ as the junction is pulled and is quite similar to the symmetric NH_2 top–top configuration of figure 1(b). The reason for the similarity with the symmetric top–top configuration is that in both cases NH_2 binds to a single gold atom on each side of the contact. This is due to the fact that the hydrogen atoms occupy two of the four available sp^3 hybrid sites, which leaves only two unoccupied orbitals for the gold bonds. Obviously this is in contrast to sulfur, which can form bonds to four gold atoms as in the top–hollow configuration of figure 4(a).

4. Summary

With the aim of identifying and comparing the intrinsic properties of thiol and amine anchoring groups in relation to molecular electronics, we have presented DFT calculations of the structure and conductance of Au–S–Au and Au–NH_2–Au nanojunctions. The main result is that the structural selectivity of the amine group leads to small junction to junction fluctuations in the conductance traces of the Au–NH_2–Au junctions, whereas the larger variability in sulphur–gold bonding geometries leads to significantly different Au–S–Au conductance traces depending on the atomic structure of the gold contacts. Thus, the intrinsic transport properties of the amine group are more well defined than those of the thiol. This supports the experimental finding that amine-bonded molecules are easier to characterize in terms of conductivity than thiol-bonded molecules. The similarity of the conductance traces of the Au–NH_2–Au junctions should lead to a peak around $0.4G_0$ in a conductance histogram. On the other hand, the structural sensitivity of Au–S–Au junctions may produce a histogram without clear features. However, it should be possible to identify the sulfur top–top structure from its characteristically rising conductance trace.

Acknowledgments

We thank N Agraït and C R Arroyo for stimulating discussions. The authors acknowledge support from the Danish Center for Scientific Computing through grant HDW-1103-06, and the Lundbeck Foundation which is sponsoring The Center for Atomic-scale Materials Design.

References

[1] Ulrich J, Esrail D, Pontius W, Venkataraman L, Millar D and Doerrer L H 2006 *J. Phys. Chem.* B **110** 2462
[2] Reed M A, Zhou C, Muller C J, Burgin T P and Tour J M 1997 *Science* **278** 252
[3] Xiao X, Xu B and Tao N J 2004 *Nano Lett.* **4** 267
[4] Tsutsui M, Teramae Y, Kurokawa S and Sakai A 2006 *Appl. Phys. Lett.* **89** 163111
[5] Ghosh S, Halimun H, Mahapatro A K, Choi J, Lodha S and Janes D 2005 *Appl. Phys. Lett.* **87** 233509
[6] Quek S Y, Venkataraman L, Choi H J, Louie S G, Hybertsen M S and Neaton J B 2007 *Nano Lett.* **7** 3477
[7] Yanson A I, Rubio Bollinger G, van der Brom H E, Agrait N and Ruitenbeek J M 1998 *Nature* **395** 783
[8] Rubio-Bollinger G, Bahn S R, Agraït N, Jacobsen K W and Vieira S 2001 *Phys. Rev. Lett.* **87** 026101
[9] Djukic D, Thygesen K S, Untiedt C, Smit R H M, Jacobsen K W and van Ruitenbeek J M 2005 *Phys. Rev.* B **71** 161402(R)
[10] Garca-Surez V M, Rocha A R, Bailey S W, Lambert C J, Sanvito S and Ferrer J 2005 *Phys. Rev.* B **72** 045437
[11] Ke S-H, Baranger H U and Yang W 2005 *J. Chem. Phys.* **122** 74704
[12] Mowbray D J, Jones G and Thygesen K S 2008 *J. Chem. Phys.* **128** 111103
[13] Bahn S R and Jacobsen K W 2002 *Comput. Sci. Eng.* **4** 56 (The Dacapo code can be downloaded at http://www.camd.dtu.dk/software)
[14] Thygesen K S, Hansen L B and Jacobsen K W 2005 *Phys. Rev. Lett.* **94** 026405
[15] Meir Y and Wingreen N S 1992 *Phys. Rev. Lett.* **68** 2512
[16] Thygesen K S 2006 *Phys. Rev.* B **73** 035309
[17] Thygesen K S and Jacobsen K W 2005 *Chem. Phys.* **319** 111
[18] Li X, He J, Hihath J, Xu B, Lindsay S M and Tao N 2006 *J. Am. Chem. Soc.* **128** 2135
[19] Anglada E, Torres J A, Yndurain F and Soler J M 2007 *Phys. Rev. Lett.* **98** 096102
[20] Perdew J P, Chevary J A, Vosko S H, Jackson K A, Pederson M R, Singh D J and Fiolhais C 1992 *Phys. Rev.* B **46** 6671

Paper V

Inelastic scattering in metal-H_2-metal junctions

I. S. Kristensen,[1] M. Paulsson,[2] K. S. Thygesen,[1] and K. W. Jacobsen[1]
[1]*Center for Atomic-scale Materials Design (CAMD), Department of Physics, Technical University of Denmark, DK-2800 Kgs. Lyngby, Denmark*
[2]*Division of Physics, Department of Natural Sciences, Kalmar University, 391 82 Kalmar, Sweden*
(Received 11 March 2009; revised manuscript received 19 May 2009; published 11 June 2009)

We present first-principles calculations of the dI/dV characteristics of an H_2 molecule sandwiched between Au and Pt electrodes in the presence of electron-phonon interactions. The conductance is found to decrease by a few percentages at threshold voltages corresponding to the excitation energy of longitudinal vibrations of the H_2 molecule. In the case of Pt electrodes, the transverse vibrations can mediate transport through otherwise nontransmitting Pt *d* channels leading to an *increase* in the differential conductance even though the hydrogen junction is characterized predominately by a single almost fully open transport channel. In the case of Au, the transverse modes do not affect the dI/dV because the Au *d* states are too far below the Fermi level. A simple explanation of the first-principles results is given using scattering theory. Finally, we compare and discuss our results in relation to experimental data.

DOI: 10.1103/PhysRevB.79.235411 PACS number(s): 73.63.Rt, 72.10.Fk, 85.65.+h

In recent years it has become possible to measure the electrical properties of single molecules captured between metallic electrodes.[1–3] Such experiments provide a unique opportunity to develop our understanding of basic quantum-mechanical phenomena at the nanometer length scale and at the same time constitute the first steps toward molecule-based electronics.[4]

Interactions between the conduction electrons and the molecule's vibrational degrees of freedom is of particular interest for the performance of molecular electronics devices as they determine the local temperature and stability of the device when subject to an external bias voltage.[5] Moreover, inelastic scattering can be used to identify the atomic structure of molecular junctions by exploiting the sensitiveness of the molecule's vibrational frequencies and the electron-phonon interaction to the junction geometry.[6–12]

Perhaps the simplest molecular junction consists of a single hydrogen molecule sandwiched between metal electrodes; see Fig. 1.[3,13] Shot noise measurements on Pt-D_2 contacts show that the conductance is carried predominantly by a single almost fully transparent channel,[14] and density-functional theory (DFT) calculations have shown that this is consistent with a linear bridge configuration.[3,15–17] An alternative configuration where the H_2 molecule is dissociated in the contact has also been proposed, however, this junction yields a conductance larger than $1G_0$ ($G_0=2e^2/h$ is the conductance quantum) with contributions from three channels.[18] Inelastic point-contact spectroscopy provides information about the hydrogen molecule's vibrational frequencies and their variation upon stretching. The data obtained from such measurements have also been found to be consistent with the linear bridge configuration.[7]

The fact that the hydrogen junction supports a single, almost fully open conductance eigenchannel suggests that the inelastic-scattering processes should be particularly simple to understand. Indeed, consider a junction supporting a single-scattering channel at the Fermi energy with a transmission probability of $\mathcal{T}=|t(\varepsilon_F)|^2$. At low temperatures the molecule sits in its vibrational ground state and the electron looses the energy $\hbar\Omega$ to the molecule during a scattering event. Assuming a bias voltage $eV=\mu_L-\mu_R>\hbar\Omega$ an electron incident on the molecule from the left with an energy just below μ_L, must end up in a left moving scattering state after interacting with the molecule. This follows from energy conservation and the Pauli principle. Upon inelastic scattering, the probability for the electron to enter the right electrode is thus changed from $\mathcal{T}$ to $\mathcal{R}=1-\mathcal{T}$. Consequently, the change in conductance due to the electron-phonon interaction should be proportional to $2\mathcal{T}-1$, i.e., an increase (decrease) in the conductance is expected for $\mathcal{T}<0.5$ ($\mathcal{T}>0.5$). The same conclusion has been reached using more rigorous arguments[19–21] and has recently been supported by measurements on Pt-H_2O junctions.[22]

In this paper we present DFT calculations for the dI/dV curves of Pt-H_2-Pt and Au-H_2-Au junctions in the presence of electron-phonon interactions. For both Pt and Au electrodes, scattering on the longitudinal modes lowers the conductance by a few percentage of G_0 in accordance with the simple one-channel model discussed above. In the case of Pt, the transverse modes can mediate tunneling through the oth-

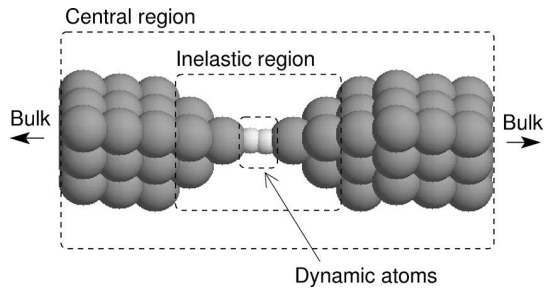

FIG. 1. The supercell use to model the metal-H_2-metal junction. Only the hydrogen atoms are allowed to vibrate (the "dynamic" atoms). This is a good approximation due to the large difference in mass between Au/Pt and H. The effect of the field generated by the vibrating H atoms is taken into account inside the indicated inelastic region. The central region, *C*, is coupled to semi-infinite bulk electrodes and periodic boundary conditions are imposed in the directions perpendicular to the contact axis.

erwise closed d-channels leading to an *increase* in the conductance of up to 5% of G_0, demonstrating that the metal-H_2-metal junction cannot be viewed as a simple one-channel system. For Au, the transverse modes have no effect on the conductance because only s states are present at the Fermi level and these do not couple via the transverse vibrations.

The Hamiltonian of the system is given by

$$\hat{H} = \hat{H}_{\mathrm{el}} + \hat{H}_{\mathrm{ph}} + \hat{H}_{\text{el-ph}}, \tag{1}$$

where $\hat{H}_{\mathrm{el}}$ is the Hamiltonian of electrons moving in the *static* equilibrium structure, $\hat{H}_{\mathrm{ph}}$ describes the vibrations of the H_2 molecule, and $\hat{H}_{\text{el-ph}}$ is the interaction between the electrons and the vibrating hydrogen atoms. For $\hat{H}_{\mathrm{el}}$ we use the Kohn-Sham Hamiltonian.

Within the harmonic approximation the molecular vibrations are described by the Hamiltonian $\hat{H}_{\mathrm{ph}}=\Sigma_\lambda \hbar\Omega_\lambda(b_\lambda^\dagger b_\lambda + \frac{1}{2})$ where $b_\lambda^\dagger$ (b_λ) creates (destroys) a phonon in mode λ. The electron-phonon interaction takes the form

$$\hat{H}_{\text{el-ph}} = \sum_{n,m\in C}\sum_{\lambda} M_{nm}^{\lambda} c_n^\dagger c_m (b_\lambda^\dagger + b_\lambda), \tag{2}$$

where the first sum runs over Wannier functions located in the inelastic region, see Fig. 1, and the second sum runs over vibrational modes. The electron-phonon coupling matrix, M^λ, is given by $M_{nm}^\lambda = \langle \phi_n(\mathbf{r}) | W^\lambda(\mathbf{r}) | \phi_m(\mathbf{r})\rangle$, where the displacement potential, $W^\lambda(\mathbf{r}) = \nabla v_s[\{\mathbf{R}_n\}](\mathbf{r})\cdot\mathbf{Q}_\lambda$, is the derivative of the effective KS potential in the direction defined by eigenmode λ. In practice W^λ is obtained as a finite difference between equilibrium Hamiltonians describing the electronic system when the hydrogen molecule has been moved in the positive and the negative normal direction.

The current flowing into the molecule (central region C) from lead $\alpha=L,R$ is calculated from the formula[23,24]

$$I_\alpha = \frac{e}{h}\int \mathrm{Tr}[\Sigma_\alpha^<(\varepsilon)G_C^>(\varepsilon) - \Sigma_\alpha^>(\varepsilon)G_C^<(\varepsilon)]d\varepsilon, \tag{3}$$

where $G_C^{<,>}$ is the lesser and greater Green's functions of the central region evaluated in the presence of coupling to leads and the phonons.[25]

The lesser and greater Green's functions are given by

$$G^{\lessgtr}(\varepsilon) = G^r(\varepsilon)[\Sigma_L^{\lessgtr}(\varepsilon) + \Sigma_R^{\lessgtr}(\varepsilon) + \Sigma_{\mathrm{ph}}^{\lessgtr}(\varepsilon)]G^a(\varepsilon), \tag{4}$$

where $G^r(\varepsilon)=[\varepsilon + i\eta - [H_{\mathrm{el}}]_C - \Sigma_L^r - \Sigma_R^r - \Sigma_{\mathrm{ph}}^r]^{-1}$ and $G^r(\varepsilon) = [G^a(\varepsilon)]^\dagger$.

The self-energy originating from the coupling to the leads are calculated using standard techniques.[26] For the self-energy due to the electron-phonon coupling from mode λ we use the first Born approximation,

$$\Sigma_{\mathrm{ph},\lambda}^{\lessgtr}(\varepsilon) = M^\lambda G_0^{\lessgtr}(\varepsilon \pm \hbar\Omega_\lambda)M^\lambda \tag{5}$$

$$\Sigma_{\mathrm{ph},\lambda}^r(\varepsilon) = \frac{1}{2}[\Sigma_{\mathrm{ph},\lambda}^>(\varepsilon) - \Sigma_{\mathrm{ph},\lambda}^<(\varepsilon)] - \frac{i}{2}\int \frac{\Sigma_{\mathrm{ph},\lambda}^>(\varepsilon') - \Sigma_{\mathrm{ph},\lambda}^<(\varepsilon')}{\varepsilon - \varepsilon'}d\varepsilon', \tag{6}$$

where the last equation follows from the general identity $G^r - G^a = G^> - G^<$ together with the Kramer's Kronig relation between Im Σ^r and Re Σ^r. We assume zero-phonon temperature corresponding to infinite cooling of the vibrations, and thus the number of phonons has been set to zero. Consequently electrons never interact with an excited molecule and therefore can only lose energy to the molecule during a scattering event.

As done often we have omitted the Hartree term in the electron-phonon self-energy.[27,28] The corresponding energy-independent contribution to the retarded self-energy can be understood as a static phonon-induced change in the mean-field electronic potential. It is expected that this small static potential would be, at least partially, screened if included in the DFT self-consistency loop.

The supercell geometry of the considered hydrogen contact is shown in Fig. 1. The distance between the two electrodes, or equivalently the length of the supercell, has for the case of Pt been chosen to make the calculated vibrational frequencies of the H_2 molecule match the experimental values as close as possible.[7] For the case of Au where less detailed experimental data is available, we have chosen the distance by minimizing the total energy. Using the plane-wave pseudopotential code Dacapo[29] we have relaxed the surface layers, the pyramids and the hydrogen molecule to obtain stable junction structures. We used an energy cutoff of 25 Ry for the plane-wave expansion, described the ion cores by ultrasoft pseudopotentials,[30] and used a $1\times4\times4$ Monckhorst pack grid for the k-point sampling. Exchange and correlation effects were described with the PW91 functional.[31] As a basis for the electronic states we use partially occupied maximally localized Wannier functions[32] which allows for an efficient and accurate calculation of transport properties as described in Ref. 26.

The vibrational eigenmodes, $\{\mathbf{Q}_\lambda\}$, and corresponding frequencies, $\{\Omega_\lambda\}$, of the H_2 molecule are obtained by diagonalizing the dynamical matrix of the system which in turn is calculated from the DFT total energies by finite differences. Thanks to the large difference in mass between the metal and hydrogen atoms, we can calculate the dynamical matrix for the two H atoms keeping all metal atoms fixed. Following this procedure we obtain a longitudinal stretching mode (M1), a longitudinal center-of-mass mode (M2), as well as two pairwise degenerate transverse modes which we refer to as hindered rotations (M3) and hindered transverse center of mass modes (M4). The modes are sketched in the insets of Fig. 2 and the corresponding frequencies are given in the caption.

In Fig. 2 we show the differential conductance calculated from Eq. (3) including scattering on the different vibrational modes separately. To extract the features due to the inelastic scattering from those due to elastic scattering we have subtracted the elastic signal, i.e., we plot $G(V)=G_{\mathrm{full}}(V)$

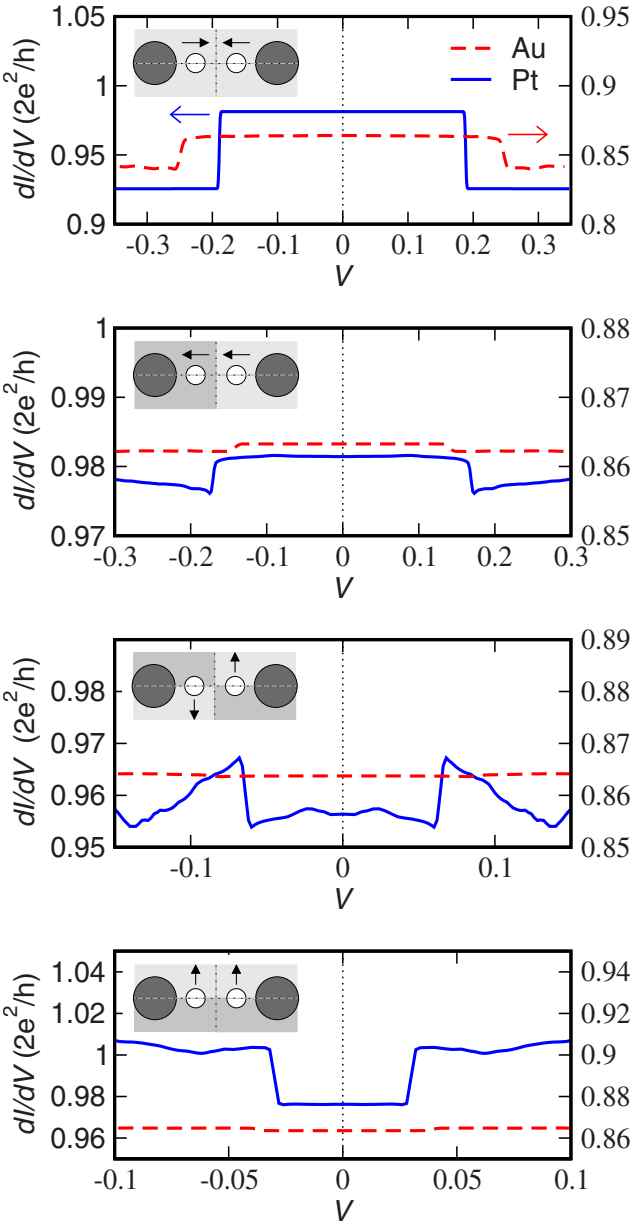

FIG. 2. (Color online) Differential conductance of the Pt-H_2-Pt (full) and Au-H_2-Au (dashed) junctions when scattering on a single vibrational mode is included. The insets illustrate the vibrational modes together with the symmetry of the corresponding displacement potential $W^{\lambda}(\mathbf{r})$. Frequencies of the H_2 vibrational modes (in meV) for Pt: $\hbar\Omega_{M1}=190$, $\hbar\Omega_{M2}=171$, $\hbar\Omega_{M3}=64$, and $\hbar\Omega_{M4}=30$ and for Au: $\hbar\Omega_{M1}=249$, $\hbar\Omega_{M2}=141$, $\hbar\Omega_{M3}=84$, and $\hbar\Omega_{M4}=37$.

$-G_{\mathrm{el}}(V)+G_{\mathrm{el}}(V=0)$, see Ref. 27 for a discussion of this procedure.

The conductance curves of Fig. 2 present several interesting features: for both Pt and Au the longitudinal modes lead to a decrease in the conductance as expected from the one-channel model. It is noticed that the internal stretching mode has a much larger impact on the electrons than the CM mode. For Au, the transverse modes have no effect on the transport, while for Pt they lead to an *increase* in the conductance. Since the junction has one fully open channel this seems to conflict with the one-channel model which would predict an increase only for junctions with conductance $<0.5G_0$. It is noted that the differences in the zero-bias conductances are due to the tails of the electron-phonon self-energy, which although centered around the vibrational frequencies also have weight at other energies. Before discussing the origin of the above mentioned features it is useful to consider a simplified description of the scattering process.

In the following we regard $\hat{H}_{\text{el-ph}}$ as a perturbation to $\hat{H}_0=\hat{H}_{\mathrm{el}}+\hat{H}_{\mathrm{ph}}$ and consider the scattering of a single electron off a molecule in its vibrational ground state. For simplicity we disregard the effect of all the other electrons (but we do take the Pauli principle into account). The scattering states of $\hat{H}_0$ are conveniently chosen as the eigenchannels incident on the molecule from the left, $\psi_{Lp}(\varepsilon)$, or right, $\psi_{Rq}(\varepsilon)$.[33,34] The probability that an electron of energy ε injected from the left lead in mode p, is transmitted (reflected) upon scattering *elastically* on the central region is denoted by $\mathcal{T}_{Lp}(\varepsilon)=|t_{Lp}(\varepsilon)|^2$ ($\mathcal{R}_{Lp}(\varepsilon)=|r_{Lp}(\varepsilon)|^2$). Due to the nonmixing property of the eigenchannels we have $\mathcal{T}_{\alpha p}+\mathcal{R}_{\alpha p}=1$ for all channels p and $\alpha=L,R$. In terms of the eigenchannels the Landauer formula for conductance takes the form $G_{\mathrm{el}}=G_0\Sigma_p\mathcal{T}_{Lp}(\varepsilon_F)=G_0\Sigma_q\mathcal{T}_{Rq}(\varepsilon_F)$. The state of the molecule is specified by the number of phonons in each mode, $|\mathbf{n}\rangle$. We use the symbol Ψ to denote a state of the combined electron-molecule system.

Assume that $eV=\mu_L-\mu_R>0$ and consider an electron incident on the junction from the left in the state $\psi^{\mathrm{in}}=\psi_{Lp}(\varepsilon)$ with $\mu_R<\varepsilon<\mu_L$ and the molecule in its vibrational ground state, $|\mathbf{0}\rangle$. According to scattering theory, the system ends up in the asymptotic out state, $\Psi^{\mathrm{out}}=\hat{S}|Lp;\mathbf{0}\rangle$, where $\hat{S}$ is the scattering operator incorporating the effect of $\hat{H}_{\text{el-ph}}$. In the first Born approximation we have the transition amplitudes

$$\langle\alpha q;\mathbf{n}|\hat{S}|Lp;\mathbf{0}\rangle\approx\langle\alpha q;\mathbf{n}|Lp;\mathbf{0}\rangle-2\pi i\delta(E_{\mathrm{in}}-E_{\mathrm{out}})\times\langle\alpha q;\mathbf{n}|\hat{H}_{\text{el-ph}}|Lp;\mathbf{0}\rangle, \tag{7}$$

where E_{in} and E_{out} are the total energies of the combined electron phonon system in the in- and out-going states. This allows us to express the out state as

$$\Psi^{\mathrm{out}}=C_p\left[\psi_{Lp}(\varepsilon)\otimes|\mathbf{0}\rangle+\sum_{q,\lambda}{}'c_{pq}^{\lambda}\psi_{Rq}(\varepsilon-\hbar\Omega_{\lambda})\otimes|1_{\lambda}\rangle\right], \tag{8}$$

where the prime in the sum means that only modes with $\hbar\Omega_{\lambda}<eV$ are included. The expansion coefficients are

$$c_{pq}^{\lambda}=D_{Rq}(\varepsilon-\hbar\Omega_{\lambda})\langle\psi_{Rq}(\varepsilon-\hbar\Omega_{\lambda})|W^{\lambda}(\mathbf{r})|\psi_{Lp}(\varepsilon)\rangle, \tag{9}$$

where $D_{Rq}(\varepsilon)$ is the electronic density of states for channel Rq. The normalization constant, $C_p=(1+\Sigma'_{q,\lambda}|c_{pq}^{\lambda}|^2)^{-1/2}$, has been introduced because the first Born approximation is not a unitary approximation to $\hat{S}$. The fact that only states coming from the right electrode are included in the sum of Eq. (8) is a simple consequence of the Pauli principle.

In the elastic case, an electronic wave-packet constructed from the states ψ_{Lp} in a narrow interval around the energy ε, initially located far from the molecule in the left lead, will make it to the right lead with probability $\mathcal{T}_{Lp}(\varepsilon)$. In contrast the scattered state (8) describes a situation where the initial wave packet makes it to the right electrode with probability

$$P_p = |C_p|^2 \left[\mathcal{T}_{Lp}(\varepsilon_F) + \sum_{q,\lambda}{}' |c_{pq}^{\lambda}|^2 \mathcal{R}_{Rq}(\varepsilon_F) \right], \tag{10}$$

where we have assumed that $\mathcal{T}$ and $\mathcal{R}$ varies little on the scale of $\hbar\Omega$. The total change in conductance due to the inelastic scattering can then be obtained from Landauer's formula

$$\Delta G = G_0 \sum_p |C_p|^2 \sum_{q,\lambda}{}' |c_{pq}^{\lambda}|^2 [\mathcal{R}_{Rq}(\varepsilon_F) - \mathcal{T}_{Lp}(\varepsilon_F)]. \tag{11}$$

Apart from the assumptions of instantaneous cooling of the phonons and weak electron-phonon interaction, which also underlie the first-principles results, Eq. (11) was derived in the absence of a Fermi sea. However, as we show below, Eq. (11) provides a simple and physically appealing explanation of the first-principles results of Fig. 2.

It follows from Eq. (11) that the change in conductance involves all pairs of channels for which the matrix element $\langle \psi_{Lp} | W^{\lambda}(\mathbf{r}) | \psi_{Rq} \rangle$ is nonzero for some mode λ. Since $W^{\lambda}(\mathbf{r})$ extends to the metal atoms binding to H_2, any scattering state—transmitting or not—with weight on these atoms will also contribute in Eq. (11).

In the case of Pt, we find at the Fermi level two types of eigenchannels with sufficient weight on the hydrogen atoms and the contacting Pt atoms that the coupling matrix element will be significant. One eigenchannel is the almost fully open *s* channel and the others have *d* character and very low transmission at ε_F. Since Au has no *d* states at the Fermi level, only the *s* channel makes a contribution in Eq. (11).

For the longitudinal modes, M1 and M2, the symmetry of W^{λ} implies that *s*-*s* transitions are possible, but not *s*-*d* transitions (*d*-*d* transitions are not excluded by symmetry, but because of the vanishing overlap between ψ_{Ld} and ψ_{Rd}). Since $\mathcal{R}_s - \mathcal{T}_s \approx -1$ we should expect a drop in conductance in agreement with the first-principles calculations. On the hydrogen molecule, the *s* channel has mainly character of the H_2 antibonding orbital. This implies that the product $\psi_{Ls}(\mathbf{r})^* \psi_{Rs}(\mathbf{r})$ is unchanged upon reflection in the plane cutting through the H-H bond perpendicular to the molecular axis. On the other hand the potential $W^{M2}(\mathbf{r})$ changes sign upon this reflection. Consequently, the matrix element $\langle \psi_{Rs} | W^{M2} | \psi_{Ls} \rangle$ will be almost zero, and this explains the weak signal observed for M2 as compared to M1.

The spatial shape of the *d* states implies that coupling to the *s* channel is possible only via the transverse modes M3 and M4, see the symmetry of W^{λ} in the insets of Fig. 2. Limiting the sums in Eq. (11) to these two relevant states we see that ΔG becomes proportional to $\mathcal{R}_d - \mathcal{T}_s$. The increase in conductance found for the transverse modes in the Pt contact can thus be explained by a higher reflection probability of the low-transmitting *d* channel as compared to the transmission probability of the high-transmitting *s* channel. We stress that small changes in the transmission probabilities for the *s* or *d* channels could change the sign of ΔG. The symmetry of the displacement potential, W^{λ}, for the transverse modes prevents coupling between two states with *s* symmetry, which explains why the transverse modes do not affect the conductance of the Au junction.

We notice that the calculated increase in conductance due to the transverse modes is not in agreement with the experimental data from inelastic point-contact spectroscopy for Pt-H_2-Pt junctions which show a conductance decrease. Some of the possible explanations for this disagreement are:

(i) According to Eq. (11), the size (and the sign) of ΔG is determined by the relative magnitude of the *s*- and *d*-channel transmissions. Even small changes here could change the sign of ΔG. In this sense, the fact that we obtain an increase in conductance while experimentally a decrease is observed, should be viewed as a quantitative rather than a qualitative difference.

(ii) In principle the 1BA applies in the limit of weak electron-phonon interactions while we obtain electron-phonon matrix elements [M in Eq. (2)] on the order of electron volts. On the other hand the inelastic features in the dI/dV are a few percentage of G_0 indicating that only a few out of a hundred electrons are scattered. Moreover, previous studies applying the 1BA to gold chains agree nicely with experiments,[8] indicating that the 1BA provides an accurate description of electron-phonon interactions in strongly coupled metal-molecule-metal junctions.

(iii) The highly symmetric geometry of the metal-H_2-metal junction used in this study is an idealized but oversimplified model of the real structure. However, we have considered other less symmetric configurations none of which gave rise to a conductance decrease for the transverse modes.

(iv) Inclusion of a finite phonon temperature could affect the calculated properties. However, as can be seen from Eq. (14) of Ref. 35, to lowest order in the electron-phonon interaction strength the sign of ΔG cannot change by including heating.

Despite the differences between the experimental and theoretical findings for the phonon-induced features in the dI/dV, we hesitate to conclude that the linear bridge configuration is not the structure observed in the experiments. The reason is the strong evidence mentioned in the introduction which favors the linear bridge combined with the small size and high sensitivity of the inelastic features.

In conclusion, we have performed first-principles calculations for the nonlinear dI/dV curves of Pt-H_2-Pt and Au-H_2-Au molecular junctions in the presence of electron-phonon interactions. For both metals, the longitudinal vibrations of the H_2 leads to a decrease in the conductance at bias voltage corresponding to the frequency of the vibration, $eV = \hbar\Omega$. In the case of Pt electrodes, the transverse vibrations induce an increase in conductance. This might seem surprising since the hydrogen junction supports a single almost fully open transport channel and thus, according to the

one-channel model, inelastic scattering should always lower the conductance. On the basis of scattering theory we showed that the increase is a result of nontransmitting *d* channels which couple to the transmitting *s* channel via the transverse modes. This is consistent with the finding that transverse modes do not affect the conductance in the case of Au electrodes.

We acknowledge support from the Lundbeck Foundation's Center for Atomic-scale Materials Design and the Danish Center for Scientific Computing.

[1] L. Venkataraman, J. E. Klare, C. Nuckolls, M. S. Hybertsen, and M. L. Steigerwald, Nature (London) **442**, 904 (2006).
[2] S. Kubatkin, A. Danilov, M. Hjort, J. Cornil, J.-L. Bredas, N. Stuhr-Hansen, P. Hedegård, and T. Bjørnholm, Nature (London) **425**, 698 (2003).
[3] R. H. M. Smit, Y. Noat, C. Untiedt, N. D. Lang, M. C. van Hemert, and J. M. van Ruitenbeek, Nature (London) **419**, 906 (2002).
[4] G. Cuniberti, G. Fagas, and K. Richter, *Introducing Molecular Electronics* (Springer, New York, 2005).
[5] Z. Huang, F. Chen, R. D'Agosta, P. A. Bennett, M. Di Ventra, and N. Tao, Nat. Nanotechnol. **2**, 698 (2007).
[6] N. Lorente, M. Persson, L. J. Lauhon, and W. Ho, Phys. Rev. Lett. **86**, 2593 (2001).
[7] D. Djukic, K. S. Thygesen, C. Untiedt, R. H. M. Smit, K. W. Jacobsen, and J. M. van Ruitenbeek, Phys. Rev. B **71**, 161402(R) (2005).
[8] T. Frederiksen, M. Brandbyge, N. Lorente, and A.-P. Jauho, Phys. Rev. Lett. **93**, 256601 (2004).
[9] E. L. Wolf, *Princinples of Electron Tunneling Spectroscopy* (Oxford University Press, New York, 1985).
[10] K. W. Hipps and U. Mazur, J. Phys. Chem. **97**, 7803 (1993).
[11] B. C. Stipe, M. A. Rezaei, and W. Ho, Phys. Rev. Lett. **82**, 1724 (1999).
[12] M. Galperin, M. A. Ratner, and Abraham Nitzan, J. Phys.: Condens. Matter **19**, 103201 (2007).
[13] A. Halbritter, P. Makk, Sz. Csonka, and G. Mihaly, Phys. Rev. B **77**, 075402 (2008).
[14] D. Djukic and J. M. van Ruitenbeek, Nano Lett. **6**, 789 (2006).
[15] J. C. Cuevas, J. Heurich, F. Pauly, W. Wenzel, and G. Schön, Nanotechnology **14**, R29 (2003).
[16] K. S. Thygesen and K. W. Jacobsen, Phys. Rev. Lett. **94**, 036807 (2005).
[17] V. M. García-Suárez, A. R. Rocha, S. W. Bailey, C. J. Lambert, S. Sanvito, and J. Ferrer, Phys. Rev. B **72**, 045437 (2005).
[18] Y. García, J. J. Palacios, E. SanFabián, J. A. Vergés, A. J. Pérez-Jiménez, and E. Louis, Phys. Rev. B **69**, 041402(R) (2004).
[19] L. de la Vega, A. Martin-Rodero, N. Agrait, and A. Levy Yeyati, Phys. Rev. B **73**, 075428 (2006).
[20] J. K. Viljas, J. C. Cuevas, F. Pauly, and M. Hafner, Phys. Rev. B **72**, 245415 (2005).
[21] M. Paulsson, T. Frederiksen, and M. Brandbyge, Phys. Rev. B **72**, 201101(R) (2005).
[22] O. Tal, M. Krieger, B. Leerink, and J. M. van Ruitenbeek, Phys. Rev. Lett. **100**, 196804 (2008).
[23] H. Haug and A.-P. Jauho, *Quantum Kinetics in Transport and Optics of Semiconductors* (Springer, New York, 1998).
[24] Y. Meir and N. S. Wingreen, Phys. Rev. Lett. **68**, 2512 (1992).
[25] Note that both the Green's functions and self-energies depend on the bias voltage, however, for notational simplicity we do not show this dependence explicitly.
[26] K. S. Thygesen and K. W. Jacobsen, Chem. Phys. **319**, 111 (2005).
[27] T. Frederiksen, M. Paulsson, M. Brandbyge, and A.-P. Jauho, Phys. Rev. B **75**, 205413 (2007).
[28] A. Gagliardi, G. C. Solomon, A. Pecchia, T. Frauenheim, A. Di Carlo, N. S. Hush, and J. R. Reimers, Phys. Rev. B **75**, 174306 (2007).
[29] B. Hammer, L. B. Hansen, and J. K. Nørskov, Phys. Rev. B **59**, 7413 (1999); S. R. Bahn and K. W. Jacobsen, Comput. Sci. Eng. **4**, 56 (2002).
[30] D. Vanderbilt, Phys. Rev. B **41**, 7892 (1990).
[31] J. P. Perdew, J. A. Chevary, S. H. Vosko, K. A. Jackson, M. R. Pederson, D. J. Singh, and C. Fiolhais, Phys. Rev. B **46**, 6671 (1992).
[32] K. S. Thygesen, L. B. Hansen, and K. W. Jacobsen, Phys. Rev. Lett. **94**, 026405 (2005); Phys. Rev. B **72**, 125119 (2005).
[33] J. R. Taylor, *Scattering Theory* (Dover, New York, 2000).
[34] M. Brandbyge, M. R. Sorensen, and K. W. Jacobsen, Phys. Rev. B **56**, 14956 (1997).
[35] M. Paulsson, T. Frederiksen, and M. Brandbyge, J. Phys.: Conf. Ser. **35**, 247 (2006).